DEFENCE S&T TECHNICAL BULLETIN

BULETIN TEKNIKAL S&T PERTAHANAN

VOL. JIL. 2 | NO. BIL. 1 | YEAR TAHUN 2009 | ISSN 1985-6571

CONTENTS

STRIDE™

SCIENCE & TECHNOLOGY RESEARCH INSTITUTE FOR DEFENCE
INSTITUT PENYELIDIKAN SAINS & TEKNOLOGI PERTAHANAN

AIMS AND SCOPE

The Technical Defence S&T Bulletin (*Buletin Teknikal S&T Pertahanan*) is the official techinal bulletin of the Science & Technology Research Institute for Defence (STRIDE). It contains articles on research findings in various fields of defence science and technology. The primary purpose of this bulletin is to act as a channel for the publication of defence-based research work undertaken by researchers both within and outside the country.

WRITING FOR THE TECHNICAL DEFENCE S&T BULLETIN

Contributions to the journal should be based on original research in the areas related to defence science and technology. All contributions should be in British English or Bahasa Melayu.

PUBLICATION

The editors' decision with regard to publication of any item is final. A paper is accepted on the understanding that it is an original piece of work which has not been accepted for publication elsewhere. Contributors will receive one complimentary copy of the issue in which their work appears.

PRESENTATIONS OF MANUSCRIPTS

The format of the manuscript is as below:-

a) MS Word format (preferably in Word 2007 format)
b) Single space.
c) Justified.
d) In Times New Roman 11-point font.
e) Should not exceed 15 pages, including references.
f) Margin should be 2 1/2 cm or 1 inch an all sides.
g) Texts in charts and tables should be in 10-point font.
h) Citations and references should follow the standard format.

Please e-mail the final paper to :

1) Dr. Zalini bt Yunus (yzalini@yahoo.co.uk)
2) Pn. Norkamizah bt Mohd. Nor (norkamizah@gmail.com)
3) Dinesh Sathyamoorthy (dinsat60@hotmail.com)

Template of the paper is as below

TITLE OF PAPER

Name of Author(s)

Address
Tel:
Fax:
E-mail:

Abstract

Contents of abstract.

Keywords: *Keyword 1; Keyword 2; Keyword 3.*

1. TOPIC

Paragraph 1.

Paragraph 2.

1.1 Sub Topic 1

Paragraph 1.

Paragraph 2.

2. TOPIC 2

Paragraph 1.

Paragraph 2.

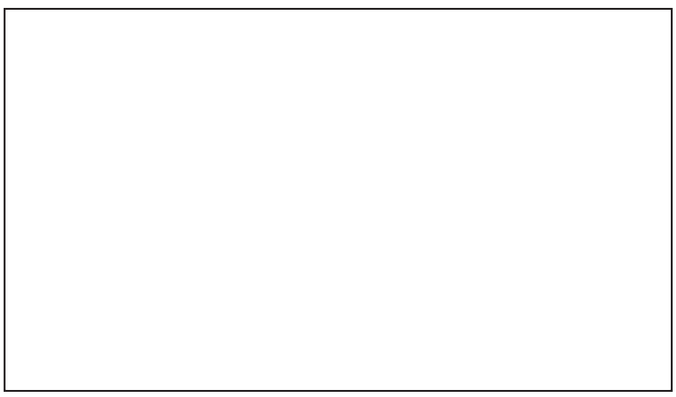

Figure 1: Title

Table 1: Title

Content	Content	Content
Content	Content	Content
Content	Content	Content
Content	Content	Content

Formula 1 (1)
Formula 2 (2)

REFERENCES

Long lists of notes of bibliographical references are generally not required. The method of citing references in the text is 'name date' sytle, e.g. 'Hanis (1993) claimed that...' or '…including the lack of interoperability (Bohara et al., 2003)'. End references should be in aplhabetical order.

1) Author(s) (Year). Title. Publisher, State Published.
2) Author(s) (Year). Title. Journal Title. Vol. , No. , pp. .
3) Website Title (Year). Website address. Accessed date and year.

TEST PROTOCOL FOR MALAYSIAN ARMED FORCES (MAF) VEHICLES: HEALTH HAZARD ASSESSMENT (HHA) AND VEHICLE PERFORMANCE

Adam Hj Gani*, Shamsul Akmar Ab Aziz & Abdul Hamid bin Hassan

Mechanical & Aerospace Technology Division
STRIDE, Taman Bukit Mewah Fasa 9, 43000 Kajang, Selangor.
Tel: 03-87324510
Fax: 03-87336219
*E-mail: ag_stride@yahoo.com

Abstract

In Malaysia, there is no standard for scientific test protocols for Malaysian Armed Forces (MAF) vehicles. Hence, this paper is aimed at proposing a suitable test protocol for MAF vehicles. This test protocol is based on test procedures employed by the Science and Technology Research Institute for Defence (STRIDE) Vehicle Branch, which is considered as the best practice at the moment. The test protocol is divided into two categories, Health Hazard Assessment (HHA) and vehicle performance. HHA will focus on vibration, noise and heat stress evaluation. Whereas, vehicle performance will be assessed by brake efficiency performance, maximum speed and turning circle capability. All tests must be performed in-field with certain test ground conditions.

Keywords: *MAF vehicles protocol test; Health hazard assessment (HHA); Vehicle performance.*

1. INTRODUCTION

As the government body responsible for the scientific tests of Malaysian Armed Forces (MAF) vehicles, the Science and Technology Institute for Defence (STRIDE) is committed in ensuring that all vehicles that are to be used by the MAF are safe and comfortable. To fulfil these requirements, several tests have to be performed.

In Malaysia, currently there is no standard for scientific test protocols for MAF vehicles. Hence, this paper is aimed at proposing a suitable test protocol for MAF vehicles. This test protocol is based on test procedures employed by the STRIDE Vehicle Branch, which is considered as the best practice at the moment. The test protocol is divided into two categories, Health Hazard Assessment (HHA) and vehicle performance. HHA will focus on vibration, noise and heat stress evaluation, while vehicle performance will be assessed by brake efficiency performance, maximum speed and turning circle capability. The primary objective of this test protocol is to provide guidelines on how to conduct HHA and vehicle performance testing in a scientific approach.

HEALTH HAZARD ASSESSMENT (HHA)

1.1 Whole Body Vibration (WBV)

WBV is defined as the mechanical vibration that, when transmitted to the whole body, entails risks to the health and safety of workers, in particular lower-back morbidity and trauma of spine (Directive 2002/44/EC, 2002). These ailments will not happen in a short period of time but will happen a few years later. Frequent exposure to excessive vibrations is the main cause of the problems. In order to minimize the risks, MAF personnel shall perform their work within a permissible exposure action limit. The daily exposure action value standardised to an eight-hour reference period shall be 0.5 m/s^2 (Directive2002/44/EC, 2002). Figure 1 shows the exposure duration and caution zone for the WBV.

The assessment of the level of exposure to vibration is based on the calculation of daily exposure A (8), expressed as the equivalent continuous acceleration calculated over an eight-hour period or the highest vibration

dose value (VDV) of the frequency-weighted accelerations, determined on three orthogonal axes (Directive2002/44/EC, 2002).

In conducting WBV measurements, vibration measurements shall be made as close as possible to, or through, the point at which the vibration is transmitted (ISO 2631/1, 1997). For a seated person, the measurement is made using a seat pad containing 3-axis accelerometers (vibration transducers). The vehicle vibration will be transmitted to the body through 3-axis transducers. The WBV data will be recorded by the transducers. The measurement will be carried out in four conditions; idle, and at velocities of 20 km/h, 40 km/h and 60 km/h (Shamsul *et al.*, 2008). The vehicle speed shall be stabilized for a few minutes at every condition. The pavement road condition shall be straight for at least 3 km. For WBV measurement, three positions will be selected, at the driver, co-driver and passenger positions. The MAF personal is seated facing sideways in the vehicle.

The data obtained will be analyzed and, comparisons will be made with Figure 1 in order to get the exposure limit. The conclusions shall be made according to Table 1.

Table 1: Comfort reactions to vibration environments.
(Source: ISO 2631/1, 1997)

Vibration Value (m/s^2)	Comfort reactions
< 0.315	not uncomfortable
0.315 - 0.63	a little uncomfortable
0.5 – 1.0	fairly uncomfortable
0.8 – 1.6	Uncomfortable
1.25 – 2.5	very uncomfortable
>2.5	extremely uncomfortable

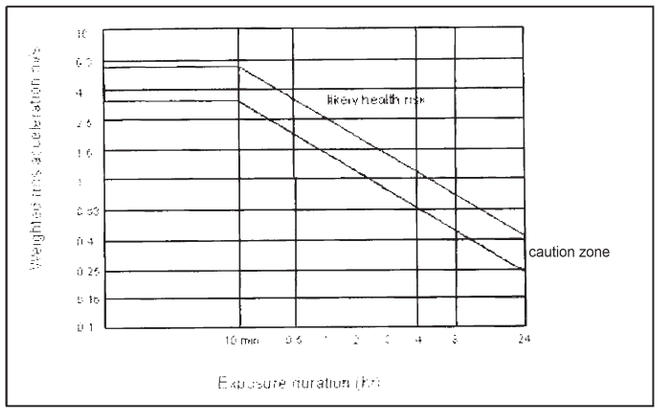

Figure 1: Health guidance zone.
(Source: ISO 2631/1, 1997)

2.2 Hand Arm Vibration (HAV)

HAV is defined as the mechanical vibration that, when transmitted to the human hand-arm system, entails risks to the health and safety of workers, in particular vascular, bone or joints neurological or muscular disorders (Directive2002/44/EC, 2002). Exposure of vibration to that particular part in long periods of time is the main cause of these ailments. To minimize the exposure action limit, MAF personnel shall work within the permissible exposure limit. The daily exposure action value standardised to an eight- hour reference period shall be 2.5 m/s^2 (Directive 2002/44/EC, 2002). The assessment of the level of exposure to HAV is based on the calculation of the daily exposure value normalised to an eight-hour reference period A (8) (Directive2002/44/EC, 2002).

In conducting HAV measurements, vibration measurements should be made at or near the surface of the hand (or hands) where the vibration enters the body (ISO 5349/2, 2001). The transducer should be located at the middle of the gripping zone; it is at this location that the most representative evaluation of the vibration entering that hand is obtained (ISO 5349/2, 2001). Figure 2 shows the transducer location for vehicle steering.

The measurements will be carried out in four conditions; idle, and speed at velocities of 20km/h, 40km/h and 60km/h. The vehicle speed shall be stabilized for a few minutes at every condition. The pavement road condition shall be straight for at least 3 km. The measurement shall be taken at least three times for each condition.

The data obtained shall be analyzed, and data comparisons with Figure 3 shall be made.

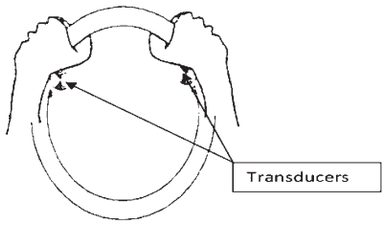

Figure 2: Measurement location for vehicle steering.
(Source: ISO 5349/2, 2001)

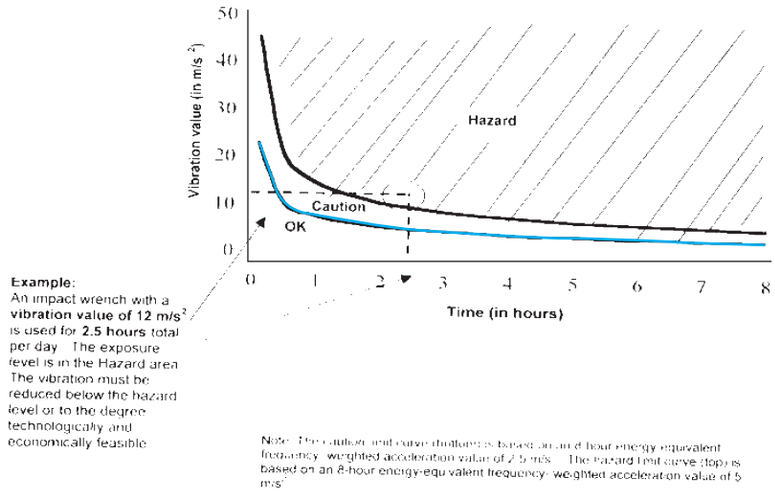

Figure 3: Hand-arm vibration exposure limit.
(Source: WISHA, 2003)

2.3 Pass-by Noise

When a vehicle is passing in front of us, or surrounding us, the sound produced by the vehicle (e.g. engine, exhaust and tyres) is known as pass-by noise. The measurement of that sound is known as the pass-by noise test. The pass-by noise test is performed to meet the requirements indicated in the Environmental Quality Act 1974-Environmental Quality (Motor Vehicle Noise) Regulation 1987 (DOE, 1987).

The basic instrument for sound measurement is the sound level meter (SLM). It is a microphone connected to a voltmeter with some additional features. The pass-by noise test shall be performed according to DOE (1987). The main parameters that should be understood before the test is carried out are the instrumentation, the test site, background noise and wind interference, and the test procedure. The detailed instructions described in DOE (1987) shall be followed. Failure to do so will cause the results to be invalid.

The maximum level of sound which may be emitted by motor vehicles having more than three wheels shall be the sound levels of Standard C as prescribed in the Second Schedule of DOE (1987) as shown in Table 2.

Table 2: Maximum sound level permitted for motor vehicles having more than three wheels. (Source: DOE, 1987)

No.	Category of Vehicle	Maximum Sound Level Permitted (dB (A))
1.	Used for the carriage of passengers and comprising not more than 9 seats (including the driver's seat).	80
2.	Used for the carriage of passengers and comprising more than 9 seats. Permitted maximum weight does not exceed 3.5 tonnes.	81
3.	Used for the carriage of goods. Permitted maximum weight does not exceed 3.5 tonnes. Engine is less than 200 h.p. DIN.	81
4.	Used for the carriage of passengers and comprising more than 9 seats. Permitted maximum weight exceeds 3.5 tonnes. Engine is less than 200 h.p. DIN.	82
5.	Used for the carriage of passengers and comprising more than 9 seats. Permitted maximum weight exceeds 3.5 tonnes. Engine is 200 h .p. DIN or more.	85
6.	Used for the carriage of goods. Permitted maximum weight exceeds 3.5 tonnes. Engine is less than 200 h.p. DIN.	86
7.	Used for the carriage of goods. Permitted maximum weight exceeds 3.5 tonnes. Engine is 200 h.p. DIN or more.	88

In performing the test, the microphone shall be placed in the positions shown in Figure 4. The vehicle shall approach line AA with the path of its centre line following line CC as closely as possible (Environmental Quality 1974, 1987). When the front of the vehicle reaches line AA, the throttle shall be fully opened as rapidly as practicable, and held fully opened until the rear of the vehicle reaches line BB, where the throttle shall then be closed as rapidly as possible (DOE, 1987).

The data obtained shall be interpreted by comparison with the Standard C shown in Table 2. In Shamsul *et al.* (2009), this test method is used to test different types of MAF vehicles in order to determine their compliance with the pass-by noise requirements indicated in DOE (1987).

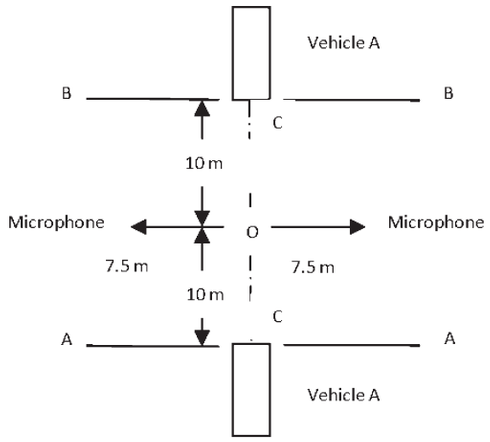

Figure 4: Microphone positions for measurements.
(Source: DOE1987)

2.4 Measurement of Engine Noise

The measurement of engine noise shall be performed at the stationary position. During the measurement, all other equipment inside the vehicle shall be switched off in order to avoid interference from the sound of air-conditioning and radio, and other unwanted sounds. The test site shall be any open space with a flat area made of concrete, asphalt or hard material having high acoustical reflectivity. The edges of the test site shall be at least 3 m from the vehicle and there shall be no objects present on the test site. The microphone positions shall be as shown in Figure 5 and according to engine location and driver position. The microphone shall be placed at a height of 0.5 m from the ground (ISO 5130, 1982).

Nowadays, most vehicles have their engines in the front. Hence, the test only will be conducted for this type of vehicles. The microphone positions shall be as shown in Figure 6. The noise emitted by the engine will be measured in two conditions; idle and full throttle. Before the measurement commences, the engine shall be stabilized at the idle position for a few second before the reading is taken. At throttle conditions, a few steps shall be followed to ensure that the maximum engine speeds are achieved. For engines with controlled ignition, engine speed shall be equal to $n/2$, where n is the engine speed at which the engine produces its maximum power as indicated by the manufacturer. For diesel engines, the governed no load speed shall be used (ISO 5130, 1982). At least three measurements shall be carried out, with only the highest level being noted.

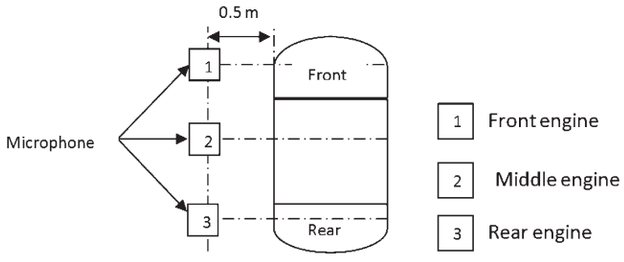

Figure 5: Microphone positions for noise measurement.
(Source: ISO 5130, 1982)

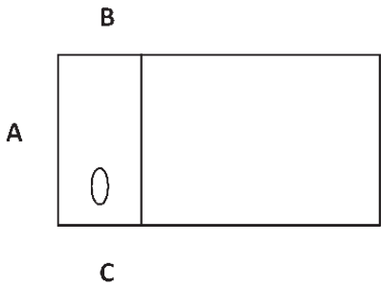

Figure 6: Microphone positions A, B and C for the front engine.

2.5 Measurement of Exhaust Noise

The measurement of exhaust noise is similar to engine noise measurement, but the difference is the microphone position. The test site, measurement methods and other conditions are similar to procedure that had been described in Section 2.4. The test method shall refer to ISO 5130 (1982) as a detailed guideline for the measurement. For this purpose, the microphone height shall be not less than 0.2 m and at the angle of 45^0±10 from the gas flow (Figure 7).

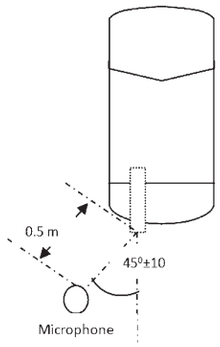

Figure 7: Microphone positions for exhaust test.
(Source: ISO 5130, 1982)

At least three measurements shall be carried out, and will be considered valid if the range of these three measurements made immediately one after another is not greater than 2 dB (ISO 5130, 1982).

2.6 Measurement of Internal Noise

The monitoring of internal noise is very important in order to check whether the noise of a vehicle is still within prescribed limits. If the noise inside the vehicle exceeds the prescribe limits, it will cause damage to human hearing. Therefore, internal noise measurement is a compulsory part of the proposed test protocol. To perform the test, the vehicle shall be in three conditions, and every condition shall be tested separately. The conditions are steady speeds, full throttle acceleration and stationary. At least five steady speeds shall be evaluated in the range of 60 to 120 km/h or 80% of maximum vehicle speed, whichever is lower. Full throttle acceleration shall be tested at 120 km/h or 90% of the engine speeds, whichever is lower and at stationary condition, two procedures, at idle and full throttle shall be tested. Other parameters that need to be considered are microphone positions, tyres and the engine itself (ISO 5128, 1980). The details of the test procedures are discussed in ISO 5128 (1980).

2.7 Noise Ranging

The requirement for the noise ranging test is based more on tactical requirements, as during the tactical operations quieter vehicle engines are really needed. Furthermore, in military applications, quieter vehicles are very important especially during war or any tactical operations. Quieter vehicles provide a significant advantage as the possibility of the vehicles' sound being heard by the enemy is less. By knowing the distance from which the engine noise can be heard, the operation can move as close as they can to an enemy base without being heard. At the same time, controlling the engine noise may reduce the contribution to noise pollution. To perform the test, the test site shall be up to 1 km in range. Microphones are positioned every 25 m from point 0 up to 1 km to determine if the sound can be measured. Two vehicle conditions shall be tested; the first condition is the front of the vehicle facing the microphones while moving away in reverse mode, and the second condition is the rear of the vehicle facing the microphones while moving away in forward mode. In both conditions, noise ranging for both idle and full throttle conditions is measured. Before the measurement, the wind speed, background noise and temperature shall be noted.

2.8 Measurement of Heat Stress

In Malaysia, the temperature can reach up to 40 $^{\circ}$C on sunny days. Hench, it is compulsory to provide each MAF vehicle with an air conditioning system. The increase in body temperature due to heat will affect safety and health, and reduce the military personnel's performance (Adam *et al.,* 2008). Heat disorders such as heat stroke, heat exhaustion, heat cramps, fainting and heat rashes may happen if the necessary precautions are neglected. Therefore, in order to monitor the temperature inside the vehicle, heat stress measurement is conducted. To perform this measurement, the value of the Wet Bulb Globe Temperature (WBGT) is recorded using heat stress equipment, which consists of a Natural Wet Bulb Thermometer, a Black Globe Bulb Thermometer and a Dry Bulb Thermometer.

To perform the measurement, the equipment shall be placed inside the vehicle half an hour before the measurement commences. Two locations shall be monitored; at passenger and driver cabins. The vehicle shall be under direct sunlight for at least 2 hours during the measurement. The details of the test method are discussed in Adam *et al*. (2008).

2. VEHICLE PERFORMANCE

2.1 Brake Efficiency

Brake efficiency is defined as the total the braking effort recorded from all the wheels of the vehicle when the brake is applied divided by the vehicle weight, and then multiplying the result by 100 (Ukmot, 2004). The test will be conducted at a steady speed of 30 km/h. For this test, speeds exceeding 30 km/h is not advisable for all types of vehicles for safety reasons. An important condition that will be taken into account in choosing the right speed is the vehicle weight. If the vehicle weight is more than 7000 kg, the speed may be revised. The parameters that shall be noted in the report are tyre pressure, type of brakes, and brake pad and disc conditions. Any other related parameters may also be considered if necessary.

Before the test commences, the tyre pressure shall be as recommended by the manufacturer and the tyres' condition shall be good. The road shall be of pavement type, straight and levelled so that the gradient influence can be reduced. A pedal force transducer shall be placed on the top of the brake pedal and shall be tightened properly. The vehicle shall be in a constant speed at 30 km/h for a few seconds before the brake pedal is pressed. The driver's foot shall be placed on the top of the transducer for immediate stopping by pressing the transducer as well as the brake pedal. The force generated by the braking effort that is transmitted to the Decelerometer is called pedal force. In theory, the applied brake force should be equal to the vehicle weight. Vehicles with 4 or more wheels shall have a service brake (foot-brake) operating on at least 4 wheels and a parking brake

(handbrake) operating on at least 2 wheels that should be not less than 50% of the brake efficiency (Ukmot, 2004).

2.2 Acceleration Performance Test

The acceleration test is carried out to confirm the vehicle's engine capabilities and power. An underpowered vehicle will slowdown its movement because the power to weight ratio is small. Vehicle pick up performance test can be done through an acceleration test on a straight, levelled and smooth road. The road should be of tarmac or concrete surface for better grip and stranglehold between the tyres and the surfaces. The vehicle shall be unladen except for the driver and the tester. Air-conditioning or any other equipment shall be turned off during the test. The vehicle's engine horse power and the vehicle's weight shall be recorded.

To perform the test, the vehicle must be moved from 0 m to 400 m. The throttle shall be fully opened when starting at the stationary position, and held fully open until the front of the vehicle reaches the 400 m marking line. The time and the highest speed are recorded once the vehicle reaches the 400 m marking line. The test shall be repeated three times.

2.3 Turning Circle

Turning circle is the measure of how easily the vehicle will be able to park or perform a U-turn in confined spaces. In military practice, a vehicle that has the capability to perform a U-turn or make a turning in a confined space is an advantage as it provides easy manoeuvrability and faster movements especially during operations. To fulfil this requirement, a small turning circle or turning radius is necessary. Therefore, the turning circle shall be checked to ensure that it conforms to what has been described in manufacturer's brochure. The usual practice is measured kerb to kerb using the front outside tyre. The reading shall be taken three times for the right turn as well as the left turn. Before the measurements are made, the vehicle shall be in stationary position and the steering shall be turned to the maximum, either to the right or to the left. After the completion of the three readings for the right turn, three readings for the left turn shall be performed. The average reading for each side shall be the final result. The results shall be compared to the manufacturer data in the brochure. In some brochure only the radius data is given, so for the diameter, or complete circle, the radius is multiplied by two. A notable exception in this description is of vehicles that are capable of spinning around their central axis, such as a tank or certain lawnmowers as they do not form a circular path as they turn. In this case, the vehicle is referred to as a "zero turning radius" vehicle, although whether or not the turning radius is actually nonexistent is unclear (Wikipedia, 2008). Figure 8 shows how to measure the turning circle.

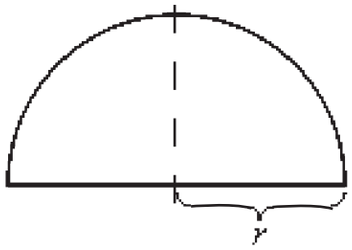

Figure 8: Turning radius.
(Source: Wikipedia, 2008)

4.0 CONCLUSION

The proposed test protocols are based on basic methods retrieved from specific standards. All the tests highlighted in this paper are based on the STRIDE Vehicle Branch's current test procedures, which have proven to be highly effective and satisfy the MAF's strict requirements. Most of the test methods and approaches are adapted from ISO standards, and some are adapted from directives and journals. For the tests which are not provided with specific references, such as brake efficiency, acceleration performance, turning circle and noise ranging, these tests are adapted from current methods that have been practiced for many years by the STRIDE Vehicle Branch. It should be noted that this test protocol describes the general test procedures required for testing MAF vehicles; the conditions and procedures can vary for different vehicle requirements. Hence, the STRIDE Vehicle Branch works closely with the MAF to ensure that the best test procedures are employed for the testing of different MAF vehicles.

REFERENCES

Adam, G., Shamsul, A. & Hamid, A. (2008). Heat Stress on Various Types of Military Vehicles in Malaysian Climate., *Defence S&T Tech. Bull.*,**1**: 16-29.

Department of Environment (DOE) (1987). Environmental Quality Act 1974 (Environmental Quality (Motor Vehicle Noise) Regulations) (1987). Department of Environment, Ministry of Natural Resources & Environment, Malaysia.

Directive 2002/44/EC. (2002). On the minimum health and safety requirements regarding the exposure of workers to the risks arising from physical agents (vibration). Brussels.

ISO 2631/1 (1997). Evaluation of human exposure to whole-body vibration. International Organization for Standardization, Geneva, Switzerland.

ISO 5349/2 (2001). Mechanical vibration-Measurement and evaluation of human exposure to hand-transmitted vibration. International Organization for Standardization, Geneva, Switzerland.

ISO 5130 (1982). Acoustics-Measurement of noise emitted by stationary road vehicle. International Organization for Standardization, Geneva, Switzerland.

ISO 5128 (1980). Acoustics - Measurement of noise inside motor vehicles. International Organization for Standardization, Geneva, Switzerland.

Ukmot (2004). Brake System. Available online at: http://www.ukmot.com/bike_3-3.asp (Last access date: 7th January 2008).

Shamsul, A., Adam, G. & Hamid, A. (2008). Whole Body Vibration (WBV) on Malaysian Armed Forces (MAF) Vehicles. *Defence S&T Tech. Bull.*, **1**: 7-15.

Shamsul, A., Adam, G. & Hamid, A. (2009). Pass-by noise of Malaysian Armed Forces (MAF) vehicles. *Defence S&T Tech. Bull,* this edition, 11-20.

WISHA (2003). Hand –Arm Vibration Analysis. Available online at: http://personal.health.usf.edu/tbernard/HollowHills/WISHA_HAV.pdf (Last access date: 23rd February 2009).

Wikipedia (2008). Turning Radius. Available online at: http://en.wikipedia.org/wiki/Turning_radius (Last access date: 17th November 2008).

PASS-BY NOISE OF MALAYSIAN ARMED FORCES (MAF) VEHICLES

Shamsul Akmar Ab Aziz*, Adam Hj Gani & Abdul Hamid Hassan

Mechanical & Aerospace Technology Division,
Science & Technology Research Institute for Defence (STRIDE),
Taman Bukit Mewah Fasa 9, 43000, Kajang, Selangor D.E.
Tel: 03-87324510
Fax: 03-87336219
*E-mail: saaa.pst@mod.gov.my

Abstract

Noise, Vibration and Harshness (NVH) is an important engineering study attribute and focus for every vehicle in research and development. Pass-by noise is one of the NVH parameters that need to be considered in order to improve noise in a vehicle as a whole. Hence, this paper will demonstrate the opportunities that pass-by noise test can provide in a new development of Malaysian Armed Forces (MAF) vehicles. This paper will consider all the requirements and advantages that pass-by noise can accomplish in a NVH study on MAF vehicles. In this study, the Vehicle Branch, Science Technology Research Institute for Defence (STRIDE will perform pass-by noise test on five commonly used MAF vehicles The main objective is to ensure that MAF vehicles meet the requirements of the Environmental Quality Act 1974 – Environmental Quality (Motor Vehicle Noise) Regulations 1987, and consequently improve overall noise quality by demonstrating procedures that will accomplish the targets of NVH. From the results obtained, three vehicles were identified as failing to fulfil the standard requirement; 3-Ton Truck Mercedes Benz 4X4 911B, Vamtac S3 and High Mobility Load Carrier (HMLC) Tatra 10 Ton 6x6. Only one vehicle passed the standard requirement; the Land Rover Defender 130 TDI 4x4. Meanwhile, the High Mobility Load Carrier (HMLC) Tatra 7 Ton 4x4 passed the standard requirement as a passenger carrier but failed as a cargo carrier.

Keywords: *Pass-by noise; Noise, Vibration and Harshness (NVH); Malaysian Armed Forces (MAF).*

1. INTRODUCTION

Sound pollution has became an important issue in present day society, with a large number of scientific papers emphasizing on the analysis of Noise, Vibration and Harshness (NVH) generated by vehicles. When a vehicle is passing in front of us or surrounding us, the sound emitted by the vehicle is called pass-by noise. Pass-by noise generated by Malaysian Armed Forces (MAF) vehicles is one of the relevant environmental issues that affect the comfort reaction of MAF personnel.

MAF vehicle is a complex vehicle in which every component is a potential source of noise. The noises emitted by MAF vehicles may be from the engine, exhaust, tyre path or from other particular components, or a combination of these sources. To monitor these noises, the method described in the Environmental Quality Act 1974-Environmental Quality (Motor Vehicle Noise) Regulation 1987 (DOE, 1987) is currently used. In most cases, the vehicle manufacturers not only want to check that the vehicle conforms to regulations, they also desire the ability to analyze the results within the framework of research and development studies. Usually, the equipment setup often requires installation and dismantling which takes most of the time needed to perform a test.

One of the problems in performing an outdoor measurement is the weather condition. Adverse weather conditions are very difficult to work in and no possible measurement can be done. Consequently, the measurement system should not only be resistant to difficult outdoor weather conditions, but also be very compact, easy to use and fast to setup (Cousin & Mauss, 2003).

In this paper, the investigation of difference types of MAF vehicles is conducted in order to determine their compliance with the pass-by noise requirements indicated in DOE (1987). If the MAF vehicle's pass-by noise complies with this standard, it means that the MAF vehicle is safe and comfortable to be used by MAF personnel. At the same time, supposed that one of the noise pollution sources can be reduced, it provides a significant tactical advantage during military operations. As one of the government bodies responsible in monitoring the human comfort of MAF vehicles, the Vehicle Branch, Science Technology Research Institute for Defence (STRIDE) is very concerned about noise pollution of MAF vehicles. Hence, pass-by noise is one of the required test methods in the standard test protocol for MAF vehicles employed by this branch (Adam *et al.*, 2009). Therefore, it is hoped that the results of this paper will provide guidelines for reducing the pass-by noise of MAF vehicles.

2. PASS BY NOISE ASSESSMENT

Noise-induced hearing loss, which is increasing slowly over the years, is caused by high levels of noise regularly exceeding a daily average of 85 dB(A) (Fernandes *et al.*, 2005). One of the main causes of hearing loss is due to occupational noise exposure. In this study, the level of daily personal noise exposure for MAF personnel is calculated using the following standard expression:

$$L_{A(EP,d)} = 10 \log 10 \left(\sum_{k=1}^{k} Tk_{10}{}^{0.1 L_{A(eq),Tk}} \right)$$

where $L_{A(EP,d)}$ is an 8-hour daily sound average and the $L_{A(eq)}$ is the A-weighted equivalent continuous sound level for an interval of time T corresponding to the type of noise k that the person is exposed to during T hours per day (Fernandes *et al.*, 2005). A-weighting is used with noise measuring equipment to give approximately the same response to different frequencies as the human ear (Powell & Forrest, 1988). Most of the measurements related to vehicle noise use A-weighting which is already set up in the equipment. The unit dB(A) is defined as decibel A-weighted, being a unit of measurement of sound level obtained when using a sound level meter corrected to the "A" weight scale using a reference pressure of 20 micropascals (DOE, 1987).

Vehicle noise can cause hearing loss, annoyance, discomfort and interfere with personal performance if it exceeds the permissible limit. Table 1 shows the maximum sound level permitted for motor vehicles having more than three wheels. It is divided into seven categories depending on usage of vehicle, vehicle permissible weight and engine capacity.

3. METHODOLOGY

3.1 Types of Vehicles

Five types of vehicles are used in this study; 3-Ton Truck Mercedes Benz 4X4 911B, Vamtac S3, Land Rover Defender 130 TDI 4x4 LRV, High Mobility Load Carrier (HMLC) Tatra 7 Ton 4x4 and Tatra 10 Ton 6x6. All these vehicles are wheeled vehicles, and shall confirm to the requirements of DOE (1987).

3.2 Methods

Pass-by noise on MAF vehicles is measured using a Sound Level Meter (SLM) Bruel & Kjaer Type 2500 or Type 2238. The equipment meet the requirements of a Type 1 instrument according to the International Electrotechnical Commission (IEC) Publication 651. The measurements shall be made by using the frequency weighting "A" and time frequency "F" (DOE, 1987).

Table 1: Maximum Sound Level Permitted For Motor Vehicles Having More Than Three Wheels. (Source: DOE, 1987)

No.	Category of Vehicle	Maximum Sound Level Permitted (dB (A))
1.	Used for the carriage of passengers and comprising not more than 9 seats (including the driver's seat)	80
2.	Used for the carriage of passengers and comprising more than 9 seats. Permitted maximum weight does not exceed 3.5 tonnes	81
3.	Used for the carriage of goods. Permitted maximum weight does not exceed 3.5 tonnes. Engine is less than 200 h.p. DIN.	81
4.	Used for the carriage of passengers and comprising more than 9 seats. Permitted maximum weight exceeds 3.5 tonnes. Engine is less than 200 h.p. DIN.	82
5.	Used for the carriage of passengers and comprising more than 9 seats. Permitted maximum weight exceeds 3.5 tonnes. Engine is 200 h .p. DIN or more	85
6.	Used for the carriage of goods. Permitted maximum weight exceeds 3.5 tonnes. Engine is less than 200 h.p. DIN	86
7.	Used for the carriage of goods. Permitted maximum weight exceeds 3.5 tonnes. Engine is 200 h.p. DIN or more	88

An SLM is positioned at each side of the vehicle (left position and right position). Each SLM is positioned 7.5 m from reference line CC (Figure 1) on the test track. The height of the SLM shall be 1.2 m above ground level. In order to comply with the standard, the measurement must be carried out under certain conditions. Background and wind noise interference will give effect to the reading. The weather shall be clear, and the wind speed shall not exceed 5 m/s. The surroundings must be clear of high vegetation or buildings. The background noise (including wind noise) shall be at least 10 dB less than levels measured during the test. Measurements shall not be made in adverse weather conditions (DOE, 1987).

The track must have certain characteristics and comply with certain rules. Standard ISO 10844 or SAE1470 describe the characteristics of the track. The test site shall be substantially levelled. The test track and the surface of the site shall be dry and free from absorbing materials such as long grass, or big trees (DOE, 1987). By considering all the parameters involved in this type of measurement, a complete system shall be able handle, control and adhere to the measurement process.

Table 2: MAF Vehicles Specifications.
(Source: STRIDE, 2004; 2005; 2007a; 2007b, 2007c)

Vehicles	3-Ton Truck Mercedes Benz	Vamtac S3, Spain	Land Rover Defender 130 TDi	Tatra 7 Ton 4x4	Tatra 10 Ton 6x6
Type	OM 352, Diesel 4 Stroke 6 Cylinder, 130hp	Turbo Intercooler, 6 line 188 hp, 3200 cc	2495 cc	4 stroke with 6 cylinder in-line	4 stroke with 6 cylinder in-line
Max Torque	363 Nm @ 2000 rpm	410 Nm @ 2000 rpm	265 Nm @ 1800 rpm	950 Nm @ 1700 rpm	1966 Nm @ 1200 rpm
Vehicle use	Goods carrier	Goods carrier	Passenger carrier	Passenger and cargo carrier	Passenger and cargo carrier
Maximum pay load (kg)	3000	2000	3500	7000	10000
Max sound level permitted (dB(A))	81	81	80	85 passenger carrier) 88 (good carrier)	85 passenger carrier) 88 (good carrier)

At least two measurements shall be made on each side (right and left). The vehicle shall approach line AA with constant speed 50 km/h. When the front of the vehicle reaches line AA, the throttle shall be fully opened as rapidly as practicably possible and held fully opened until the rear of the vehicle reaches line BB, where the throttle shall be closed as rapidly as possible. The measurement shall be made on each side of vehicle, with 2 readings for each side of vehicle. The results are valid if the differences between 2 readings do not exceed 2 dB, and the highest value given by the measurement shall be adopted as the representative value of the noise generated from running vehicles on roads (DOE, 1987).

Figure 1: Microphone positions for measurements
(Source: DOE, 1987)

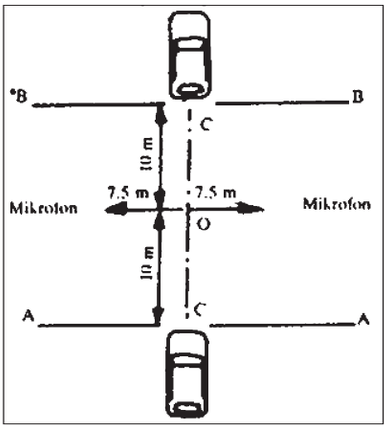

13

4. RESULTS & DISCUSSION

4.1. 3-Ton Truck Mercedes Benz 4X4 911B (Figure 2)

This trial was carried out at Kahang Air Strip, Johor (STRIDE, 2004). This location was selected because it has a long path road and is located far away from the main road. The wind speed and environmental noise levels were recorded to ensure these parameters do not exceed the given limits.

Figure 2: 3-Ton Truck Mercedes Benz.

Table 3: 3-Ton Truck Mercedes Benz pass-by noise test results.

	Sound Pressure Level dB(A)	
	Left Position	**Right Position**
Reading 1	84.0	81.0
Reading 2	84.1	81.6
Reading 3	84.3	82.6
*** Environment parameters:** Wind Speed : 1.2 – 1.5m/s Background Noise : 33.5 dB(A) Temperature: 38^{o}C		

From the vehicle specification given in Table 2, this vehicle falls into Category 3 (Table 1), for which the permitted sound level is 81 dB(A). From the results (Table 3), the highest reading obtained for this vehicle was 84.3 dB (A) at the left position. We can conclude that the overall sound produced by this vehicle exceeds the permitted limit.

4.2 Vamtac S3 (Figure 3)

URO VAMTAC (Vehículo de Alta Movilidad Táctico) is a four-wheel drive military vehicle manufactured by the Spanish Company, Urovesa. This vehicle was physically evaluated by the MAF trial team at Kahang Air Strip, Johor in February 2007 (STRIDE, 2007b).

From the vehicle specification given in Table 2, this vehicle falls into Category 3 (Table 1), for which the permitted sound level is 81 dB(A). From the results (Table 4), the highest reading obtained for this vehicle was

101.1 dB(A) at right position. We can conclude that the overall sound produced by this vehicle exceeds the permitted limit.

Figure 3: Vamtac S3.

Table 4: Vamtac S3 pass-by noise test results.

	Sound Pressure Level dB(A)	
	Left Position	Right Position
Reading 1	96.0	100.3
Reading 2	97.6	100.5
Reading 3	96.8	101.1
***Environmental parameters:** Wind Speed : 2.5 - 3.5 m/s Background Noise : 39.8 dB(A) Temperature : 35^{o}C		

4.3 Land Rover Defender 130 TDI 4x4 (Figure 4)

The Land Rover Defender is a British four-wheel drive off-road utility vehicle (STRIDE, 2004). In Malaysia, this vehicle is a common utility vehicle that is used to carry armed forces personnel and light goods.

Figure 4: Land Rover Defender 130 TDI 4x4.

Table 5: Land Rover Defender 130 TDI pass-by noise test results.

	Sound Pressure Level dB(A)	
	Left Position	**Right Position**
Reading 1	79.0	78.9
Reading 2	79.2	78.4
Reading 3	79.1	78.7
***Environmental parameters:** Wind Speed : 2.5 - 3.5 m/s Background Noise : 39.0 dB(A) Temperature : 35^{o}C		

From the vehicle specification given in Table 2, this vehicle falls into Category 1 (Table 1), for which the permitted sound level is 80 dB(A). From the results (Table 5), the highest reading obtained from this vehicle was 79.2 dB(A) at the left position. We can conclude that the overall sound produced by this vehicle does not exceed the permitted limit.

4.4 High Mobility Load Carrier (HMLC) Tatra 7 Ton 4x4 (Figure 5)

The MAF trial team conducted the physical evaluation for this truck, which was manufactured by Tatra Company, Czech Republic (STRIDE, 2007a). This truck is used for transporting personal, logistics and goods.

Figure 5: High Mobility Load Carrier (HMLC) Tatra 7 Ton 4x4.

Table 6: Tatra 7 Ton 4x4 pass-by noise test results.

	Sound Pressure Level dB(A)	
	Left Position	**Right Position**
Reading 1	87.0	88.1
Reading 2	87.4	88.5
Reading 3	87.2	88.7
***Environmental parameters:** Wind Speed : < 5 m/s Background Noise : 34.5 dB(A) Temperature : 36^{o}C		

From the vehicle specification given in Table 2, this vehicle falls into Category 5 (Table 1) if used as a passenger carrier, and Category 7 (Table 1) if used as a cargo carrier. The permitted sound level is 85 dB(A) and 88 dB(A) respectively. From the results (Table 5), the highest reading obtained for this vehicle was 88.7 dB(A) at the right position. We can conclude that the overall sound produced by this vehicle does not exceed the permitted limit if used as a passenger carrier, but exceeds the permitted limit if used as a cargo carrier.

4.5 High Mobility Load Carrier (HMLC) Tatra 10 Ton 6x6(Figure 6)

The Tatra 10 Ton vehicle has the same functions as the Tatra 7 Ton vehicle, but has a different-axle system, which was upgraded to the 6x6 type (STRIDE, 2007b).

Figure 6: High Mobility Load Carrier (HMLC) Tatra 10 Ton 6x6.

Table 7: Tatra 7 Ton 6x6 pass-by noise test results.

	Sound Pressure Level dB(A)	
	Left Position	**Right Position**
Reading 1	83.5	84.6
Reading 2	83.8	84.9
Reading 3	83.5	84.0
***Environmental parameters:** Wind Speed : < 5 m/s Background Noise : 34.5 dB(A) Temperature : 36^{o}C		

From the vehicle specification data given in Table 2, this vehicle falls into Category 5 (Table 1) if used as a passenger carrier, and Category 7 (Table 1) if used as a cargo carrier. The permitted sound level is 85 dB(A) and 88 dB(A) respectively. From the results (Table 7), the highest reading obtained from this vehicle was 84.9 dB(A) at right position. We can conclude that the overall sound produced by this vehicle exceeds the permitted limit for the both its functions, as a passenger carrier and as a cargo carrier.

5. CONCLUSION

Pass-by noise measurement was conducted to determine the maximum overall sound pressure level emitted by an MAF vehicle while accelerating between a set of two SLMs. As high sound pressure levels can cause damage to the human hearing, necessary reduction of exposure in sound levels is required for acoustic comfort. From the results above, three vehicles were identified as failing to fulfil the standard requirement as stated in DOE (1987). They were 3-Ton Truck Mercedes Benz 4X4 911B, Vamtac S3 and High Mobility Load Carrier (HMLC) Tatra 10 Ton 6x6. Only one vehicle passed the standard requirements; the Land Rover Defender 130 TDI 4x4. Meanwhile, the High Mobility Load Carrier (HMLC) Tatra 7 Ton 4x4 passed the standard requirement as a passenger carrier but failed as a cargo carrier.

To conclude, a reduction in the sound level of noise sources can be obtained by regular maintenance, early repairs, and replacement of defective items of the vehicles. Currently the exterior noise level of the accelerated pass-by noise measurement is the only legal limit for vehicle acoustics. Within the scope of further noise emission reduction efforts, a tightening of limits and the procedure can be expected. Pass-by noise measurements can support the development activities of car manufactures in producing environmental friendly MAF vehicles. We hope that the enforcement of the rules and regulations will be more stringent to ensure the noise level emitted by MAF vehicle is below the permitted level limit.

ACKNOWLEDGEMENTS

The authors would like to acknowledge the support of the STRIDE Vehicle Branch members, Mr Amin Nor Rahamat, Mr. Sanib Saidon, Mr. Borhanuddin Mohd Youssof and Mr. Mohamad Fairuz Ahmad, for their support for this project.

REFERENCES

Adam, G., Shamsul, A. & Hamid, A. (2009). Test protocol for Malaysian Armed Forces (MAF) vehicles: Health Hazard Assessment (HHA) and vehicle performance. *Defence S&T Tech. Bull.*, this edition, 1-10.

Cousin, G. & Mauss, P. (2003). An overview of vehicle pass-by noise. OROS, Virginia, USA.

Department of Environment (DOE) (1987). Environmental Quality Act 1974 (Environmental Quality (Motor Vehicle Noise) Regulations) (1987). Department of Environment, Ministry of Natural Resources & Environment, Malaysia.

Fernandes, S.J.C., Carvalho, A.P.O., Gallas, M., Vaz, P. & Matos, A. (2005). Noise Levels in Dental Schools. University of Porto, Portugal.

Fry.J. & Jennings.P. (2003). Using multi-layer perceptions to predict vehicle pass-by noise. University of Warwick, United Kingdom.

Powell, R.F. & Forrest, M.R. (1988). Noise in the Military Environment. Shrivenham, United Kingdom.

STRIDE (2004). Laporan STRIDE Ujinilai Land Rover Defender 130 TDI 4x4 LRV. Science & Technology Institute for Defence (STRIDE), Ministry of Defence, Malaysia.

STRIDE (2005). Laporan STRIDE Ujinilai 'Technology Demonstrator' Trak 3 Ton Mercedes Benz 4X4 911B/911C Yang Telah Di Baikpulih. Science & Technology Institute for Defence (STRIDE), Ministry of Defence, Malaysia.

STRIDE (2007a). Laporan STRIDE Ujinilai High Mobility Load Carrier (HMLC) Tatra 7 Ton 4x4. Science & Technology Institute for Defence (STRIDE), Ministry of Defence, Malaysia.

STRIDE (2007b). Laporan STRIDE Ujinilai High Mobility Load Carrier (HMLC) Tatra 10 Ton 6x6. Science & Technology Institute for Defence (STRIDE), Ministry of Defence, Malaysia.

STRIDE (2007c). Laporan STRIDE Ujinilai Vamtac S3 dari Spain. Science & Technology Institute for Defence (STRIDE), Ministry of Defence, Malaysia.

CALCULATION OF STRESS CONCENTRATION FACTORS OF VARIOUS GEOMETRIC DISCONTINUITIES USING ANSYS

Yogeswaran A/L Sinnasamy*, Mohd Zaidi bin Ismail & Md Ashly bin Ibrahim

Maritime Technology Division,
Science & Technology Research Institute for Defence (STRIDE),
D/A KD MALAYA, Pangkalan TLDM, 32100 Lumut, Perak Darul Ridzuan.
Tel: 05 – 681 7360 Fax: 05 – 681 7350
*Email: yoges_aero@yahoo.com

Abstract

A stress concentration is a location in an object or member of a structure where stress is concentrated. Stress concentration is an important factor in machineries design as it gives rise to localized and centralized stress when any changes in the design of surface or cross section occurred. A material can fail or break, via a propagating crack, when a concentrated stress exceeds the material's theoretical cohesive strength. There are two methods used to calculate stress concentration factor; finite element method (FEM) and theoretical method. One of the most popular FEM softwares is ANSYs which is widely used in many applications and industries. In this paper, different kinds of geometric discontinuities are analyzed using ANSYS in terms of their physical changes and responses to varying geometric discontinuities ratios by applying horizontal load at constant rate. In this calculation, rectangular steel plates are used as geometric models due to the easiness of creating models and the existence of such geometric shapes in many applications such as body frames of ships, and aircraft and military tanks, especially the portions where rivetings are done. Three types of geometric discontinuities, U-shape notches, centre hole and fillets, are modelled and analysed in 2-D using plate models. It is found that the plate model with a centre hole has the highest value of stress concentration factor, while the plate model with U-shaped notches has the lowest value.

Keywords: *Stress concentration factors; finite element method (FEM); ANSYS.*

1. INTRODUCTION

Stress in an axially loaded structural member of a gradually changing or near constant cross section (as shown in Figure 1) can be computed by the simple relationship shown in Equation 1, where P is the applied load and A is the cross sectional area of the member. The limitation of this equation is that it cannot satisfactorily compute axial stress if the cross sectional area is not near constant or changes abruptly. Furthermore, it cannot be used to predict the values of stress that occur around geometric discontinuities (such as in Figure 2) because it assumes that stress is uniform throughout the member.

$$\sigma = P / A \tag{1}$$

Figure 1: Plate with constant cross section and under load *P*.

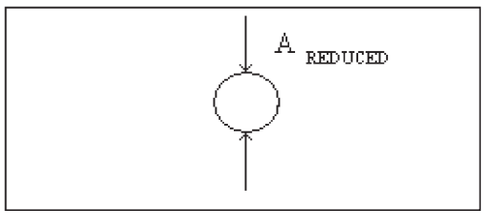

Figure 2: Example of a plate with hole as a geometric discontinuity.

There are many types of geometric discontinuities such as U-shapes, holes, fillet, and cracks. Almost all machine components and structural members contain some form of geometric or micro-structural discontinuities. The maximum local stress normally occurs at these discontinuities. For example, as shown in Figure 3, for a member with a hole, high stresses occur in a section passing through the centre of the hole Thus, the discontinuities cause areas of stress concentration within the component, and are often called "stress raisers". In marine, aviation and land vehicle applications, the existence of geometric discontinuities is very important to be considered, especially for parts of the vehicle which always experience continuous and high levels of stress that would fracture the member when the stress produced exceeds the maximum value.

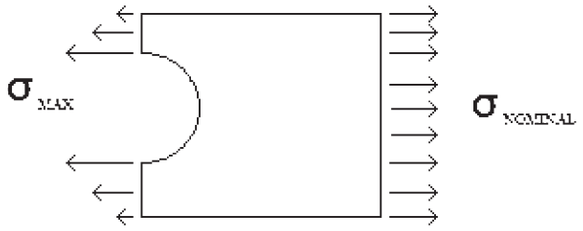

Figure 3: Maximum stress distributions at the tip of the notch.

The ratio of the average or nominal stress $\sigma_{NOMINAL}$ to the maximum stress σ_{MAX} is called the Stress Concentration Factor and is denoted by K as per Equation 2, where $\sigma_{NOMINAL}$ is defined as the stress over the net area of the reduced section $A_{REDUCED}$ as per Equation 3. Knowledge of the values of K can help designers and engineers find the required maximum stress for their designs.

$$K = \sigma_{MAX} / \sigma_{NOMINAL} \tag{2}$$

$$\sigma_{NOMINAL} = P / A_{REDUCED} \tag{3}$$

There are two methods used to calculate stress concentration factor; finite element method (FEM) and theoretical method. FEM, sometimes referred to as finite element analysis (FEA), transforms differential equations into a set of algebraic equations. If the original differential equations are linear in form, FEM gives rise to a set of linear algebraic equations which can be solved using the application of the appropriate boundary conditions to obtain an approximate solution to the boundary value problem. FEM originated from the requirement for solving complex elasticity and structural analysis problems in civil and aerospace engineering. Its development can be traced back to the work by Hrennikoff (1941) and Courant (1942). FEM has been used for analyzing structural parts since the 1950s. The method was first developed for use in the aerospace and nuclear power industries. Here, the safety of the structures is critical; they involve large expenditure and the economic consequences of a failure are very severe, so the cost of the analysis is justified. Today, the method is also extensively used in areas such as the automotive industry, where components are relatively cheap but are manufactured in large volumes. Furthermore, any small reduction in the safe weight of a component such as a connecting rod can lead to additional benefits in areas such as vibration reduction and fuel economy. The growth

in the usage of FEM is directly attributable to the rapid advances in computing technology in recent years (Oden, 1987; Thomas, 2000; Solin et al., 2003; Zienkiewicz *et al.* 2005; Cook *et al.*, 2007; Waterman, 2008).

One of the most popular FEM softwares is ANSYS. This software uses a pre-processor software engine to create geometry. It then uses a solution routine to apply loads to meshed geometry. Finally it outputs the desired results in post-processing (DeSalvo & Gorman, 1987; ANSYS, 2005). ANSYS was first introduced in the aerospace industry for making the wings of aircrafts, and then, became very important in other fields of science and industry such as heat transfer analysis, air conditioning flow analysis, automotive industry, ship repair, building sector, civil construction and collapse investigation (DeSalvo & Gorman, 1987; Rudnyi & Korvink, 2006; Moaveni, 2007). ANSYS was also used in the investigation of the World Trade Centre collapse in 2001 (Moaveni, 2007). The software contains many routines that are interrelated to achieve a solution to practical problems using FEM. Analysis of models using ANSYS is divided into five stages; Pre-processing, Simulation or Solution, Post-processing, Refine Model and Advanced Refine Model (DeSalvo & Gorman, 1987; ANSYS, 2005).

In this paper, different kinds of geometric discontinuities are analyzed using ANSYS in terms of their physical changes and response to varying geometric discontinuities ratios by applying horizontal load at constant rate. In this calculation, rectangular steel plates are used as geometric models due to the easiness of creating models and the existence of such geometric shapes in many applications such as body frames of ships, aircrafts and military tanks, especially the portions where rivetings are done.

2. METHODS AND MATERIALS

2.1 Dimensions of Plate Models

In this paper, three types of geometric discontinuities are analyzed; U-shaped notches ((Figure 4a), centre hole (Figure 4b), and fillets (Figure 4c). Each geometric discontinuity has different ratios which will be modelled separately in 2-D using a plate model with width D 0.12 in and thickness t 0.04 in. The material used for this application is stainless steel with material properties; elastic modulus $E = 2.07 \times 10^{11}$ N/m^2 and Poisson's ratio $\upsilon = 0.29$.

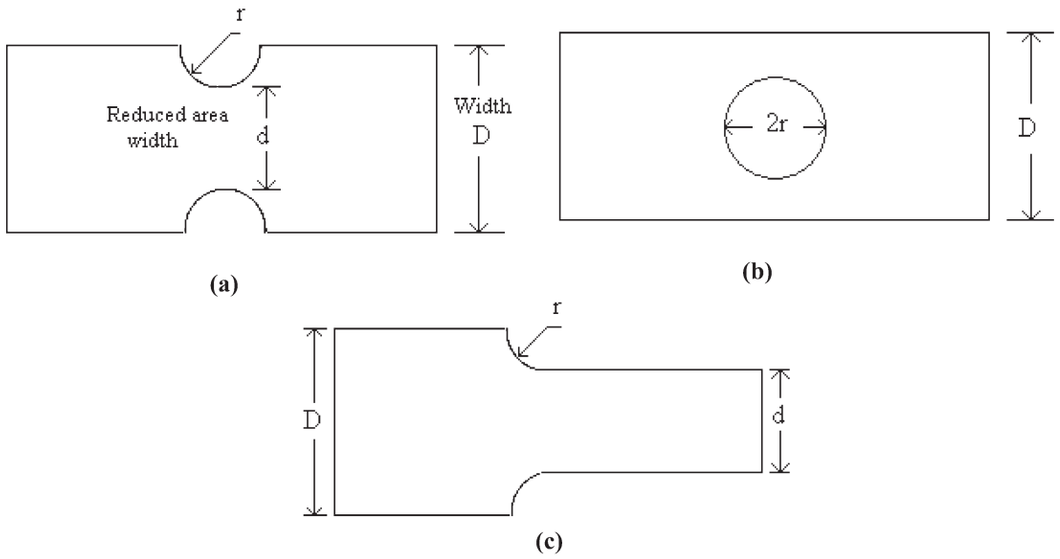

Figure 4: Plate models with discontinuities; (a) U-shaped notches, (b) centre hole and (c) fillets. *D* is the width of the plate, *d* is the reduced width of the plate caused by the discontinuities and *r* is the radius of the discontinuities.

2.2 Element Selection

The accuracy of the solution depends on the number of elements (subdivisions); the more elements used, the greater is the accuracy. However, although the analysis of each individual element is straightforward the analysis of a large number of elements becomes extremely tedious. In ANSYS, 2-D problems can be modelled with six-node triangles, four-node quadrilaterals or eight-node quadrilaterals. The greater the number of nodes, the higher the order of the polynomial and the greater the accuracy in describing displacements, stresses and strains within the element. If the stress is constant throughout a region, a very simple model, with perhaps only one or two elements, is sufficient to describe the stress state.

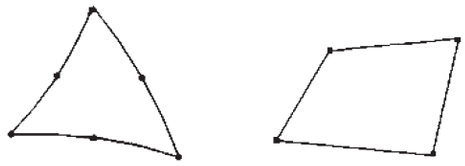

Figure 5: 2-D problems can be modelled using (a) six-node triangles and (b) four-node quadrilaterals.

2.3 Calculation

For each model, the calculation will have three steps. The first step is to calculate the value of $\sigma_{NOMINAL}$ using Equation 3. Then the second step is to extract the value of σ_{MAX} from the finite element output. The last step is to calculate the value of K using Equation 2.

3. RESULTS

3.1 Plate Model with U-shaped Notches

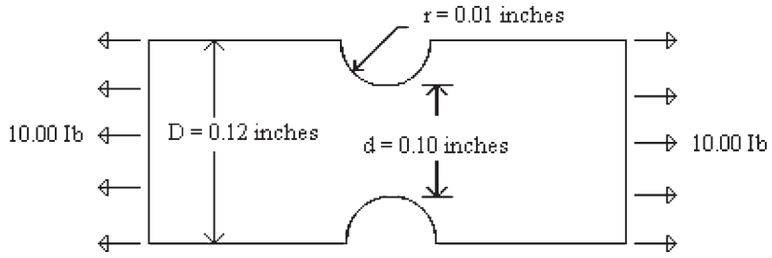

Figure 6: Plate model with U-shaped notches.

Calculation of $\sigma_{NOMINAL}$ for the plate model with U-shaped notches (Figure 6):

$$\begin{aligned} \sigma_{NOMINAL} &= P / A_{REDUCED} \\ &= P / (D - r - r) * t \\ &= 10.00 / (0.12 - 0.01 - 0.01) * 0.04 \\ &= 2500.00 \text{ psi.} \end{aligned}$$

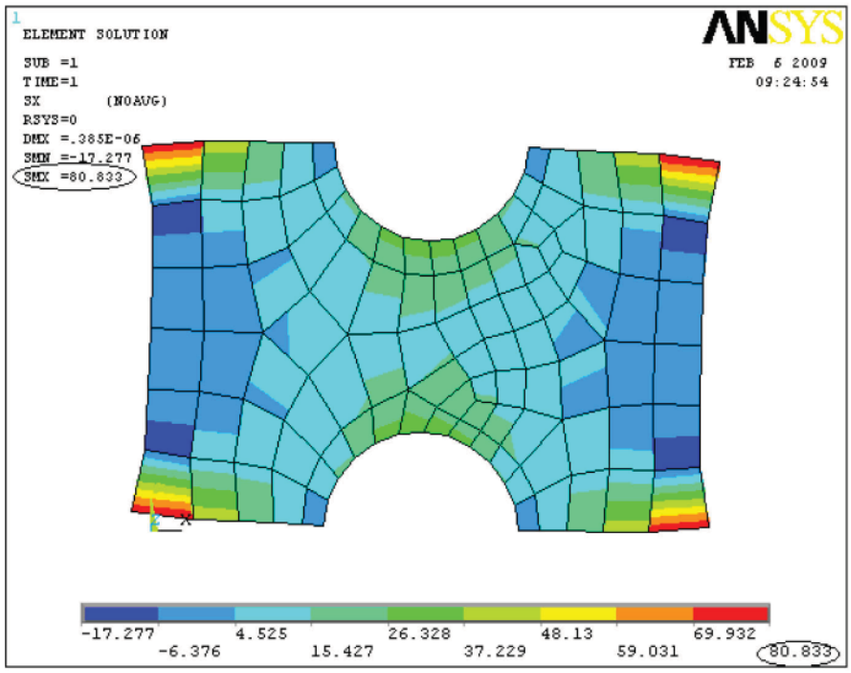

Figure 7: Finite element image for the plate model with U-shaped notches.

Figure 7 shows the finite element image for the plate model with U-shaped notches. The circled item on the image is the value of σ_{MAX}; 80.83 psi.

Hence, $K = \sigma_{MAX} / \sigma_{NOMINAL} = 80.83 / 2500.00 = 0.03$.

3.2 Plate Model with a Centre Hole.

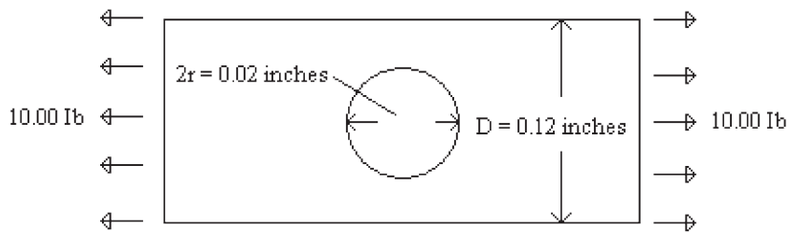

Figure 8: Plate model with a centre hole.

Calculation of $\sigma_{NOMINAL}$ for the plate model with a centre hole (Figure 8):

$$\begin{aligned} \sigma_{NOMINAL} &= P / A_{REDUCED} \\ &= P / (D - 2r) * t \\ &= 10.00 / (0.12 - 0.02) * 0.04 \\ &= 2500.00 \text{ psi.} \end{aligned}$$

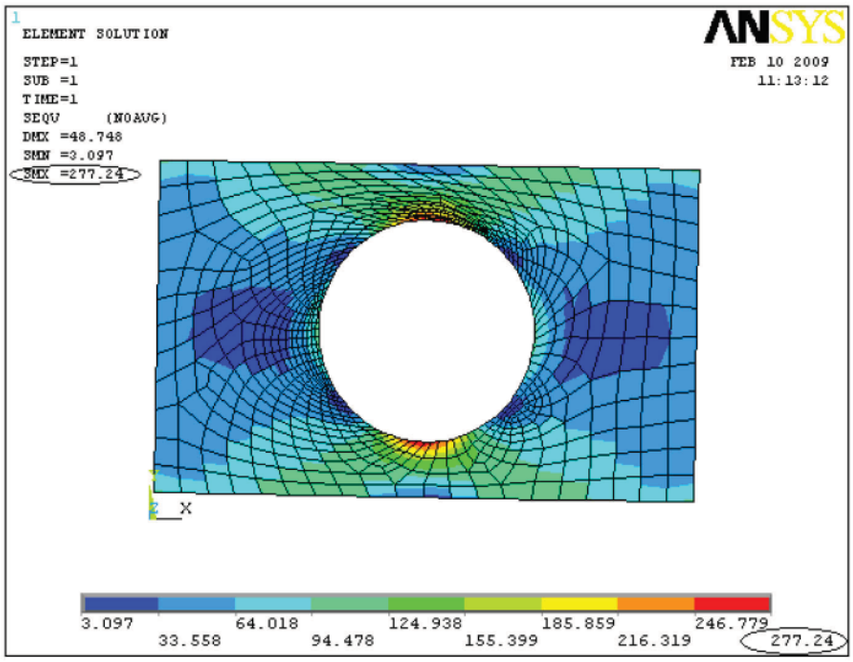

Figure 9: Finite element image for the plate model with a centre hole.

Figure 9 shows the finite element image for the plate model with a centre hole. The circled item on the image is the value of σ_{MAX}; 277.24 psi.

Hence, $K = \sigma_{MAX} / \sigma_{NOMINAL} = 277.24 / 2500.00 = 0.11$.

3.3 Plate Model with Fillets

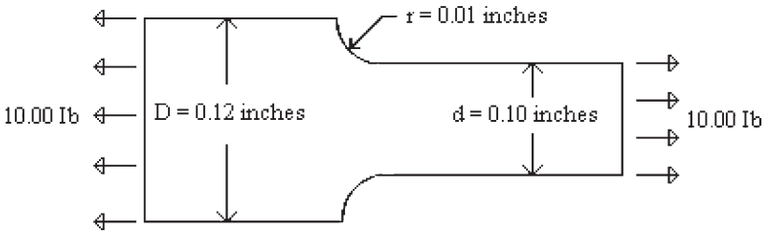

Figure 10: Plate model with fillets.

Calculation of $\sigma_{NOMINAL}$ for the plate model with fillets (Figure 10):

$$\begin{aligned} \sigma_{NOMINAL} &= P / A_{REDUCED} \\ &= P / (D - 2r) * t \\ &= 10.00 / (0.12 - 0.04) * 0.04 \\ &= 3125.00 \text{ psi.} \end{aligned}$$

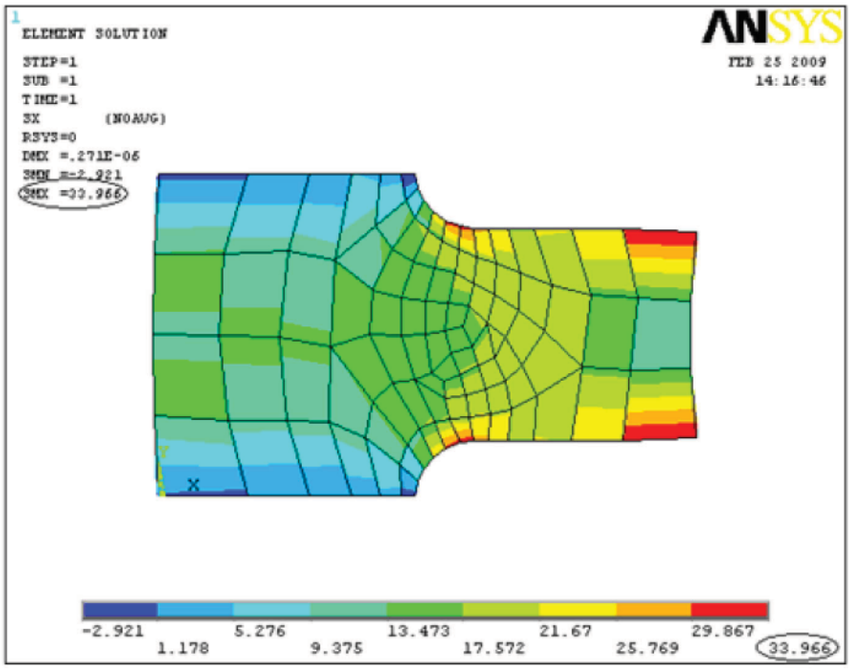

Figure 11: Finite element image for plate model with fillets.

Figure 11 shows the finite element image for plate model with fillets The circled item on the image is the value of σ_{MAX}; 277.24 psi.

Hence, $K = \sigma_{MAX} / \sigma_{NOMINAL}$
$= 277.24 / 3125.00$
$= 0.09.$

4. DISCUSSION AND SCOPE FOR FUTURE WORK

Based on the results for each model, it was found that the plate model with a centre hole has the highest value of *K*, while the plate model with U-shaped notches has the lowest value of *K*. In comparison, these two plate models are only different in their orientation of the geometric discontinuities, while other factors, such as width, length and radius of the geometric discontinuities, are same. The highest value shows that the plate model with centre hole is stronger than plate model with U-shaped notches. This is because, based on the finite element image, the plate model with centre hole needs more stress to reach deformed state compared with plate model with U-shaped notches with each of the plate model having the same value of nominal stress. For the plate model with fillets, the comparison is not possible because the value of the nominal stress is different among these three plate models.

In this paper, each type of geometric discontinuities was modelled using a single value of radius. For future research, it is recommended to use different values of radius for each type of geometric discontinuities. By using different set of dimensions and radius values, researchers will be able to create a trend of stress concentration values versus ratio of plate models and make comparison with standard graphs stress concentration factors.

REFERENCES

ANSYS (2005). ANYSYS 10.0 Documentation. ANSYS Inc., Canonsburg, Pennsylvania.

Cook, R.D., Malkus, D.S., Plesha, M.E. and Witt, R.J. (2007). The Finite Element Method in Engineering Science. John Wiley & Sons, West Sussex, England.

Courant, R. L. (1943). Variational methods for the solution of problems of equilibrium and vibration. *Bull. Am. Math. Soc*., **49**: 1-23.

DeSalvo, G.J. & Gorman, R.W. (1987). ANSYS Engineering Analysis System User's Manual. Swanson Analysis Systems, Canonsburg, Pennsylvania.

Hrennikoff, H. (1941). Solutions of problems in elasticity by the framework method. *J. Appl. Mech.*, **8**: 169-175.

Moaveni, S. (2007). Finite Element Analysis Theory and Application with ANSYS.Prentice-Hall, New Jersey.

Oden, T. (1987). Some historic comments on finite elements. *Proceedings of the ACM Conference on History of Scientific and Numeric Computation*, Princeton, New Jersey, pp. 125 - 130.

Rudnyi, E.B. & Korvink, J.G. (2006). Model order reduction for large scale engineering models developed in ANSYS. *Lec. Notes Comp. Sci.*, **3732**: 349-356.

Solin, P, Segeth, K. & Dolezel, I. (2003). Higher-Order Finite Element Methods. Chapman & Hall/CRC Press, Boca Raton.

Thomas, H. (2000). The Finite Element Method: Linear Static and Dynamic Finite Element Analysis. Dover Publications, New York.

Waterman, P.J. (2008). Meshing: The critical bridge. Available online at:

http://www.deskeng.com/articles/aaakfj.htm (Last access date: 27th February 20009)

Zienkiewicz, O.C., Taylor, R.L. & Zhu, R.J. (2005). The Finite Element Method: Its Basis and Fundamentals. Elsevier, Amsterdam.

COMPUTATION OF SCALE INDEPENDENT SURFACE ROUGHNESS

Dinesh Sathyamoorthy

Instrumentation and Electronic Technology Division
STRIDE, Ministry of Defence, Malaysia
Tel: 603-87324431
Fax: 603-87348695
E-mail: dinsat60@hotmail.com

Abstract

Surface roughness is a useful tool for terrain analysis as it reflects numerous geophysical parameters, such as landform characteristics, distribution of crenulations and degree of erosivity. Hence, in the past few decades, the quantitative computation of surface roughness of terrains for the purposes of numerical surface study has received increasing attention, with a number of algorithms being proposed to compute surface roughness. These algorithms, which operate at singular scales of measurement, provide scale-dependant roughness parameters. In an earlier research effort, a procedure to compute a scale-independent surface roughness parameter from digital elevation models (DEMs) was proposed. In this paper, this procedure is extended to perform the computation of the surface roughness of individual pixels of DEMs. Mathematical morphology is employed to segment the terrain of a DEM into the three predominant physiographic features; mountains, basins and piedmont slopes. The lifting scheme is used to generate multiscale DEMs. The mask of pixels modified in each distinct individual landform at each scale is computed by performing the intersection operation between the landform and the mask of pixels modified at each scale. The normalized probability functions for each landform are computed as the ratio of the area of pixels modified in the landform at each scale to the area of the landform. The computed normalized probability functions are used to compute the average size of convex and concave regions in the landform, the scale-independent average roughness of the landform due to the distribution of convex and concave regions averaged over the landform, and the landform's roughness coefficient. The surface roughness of each individual pixel in the landform is computed by multiplying the roughness coefficient with the pixel's area of convex and concave regions. The proposed procedure provides a surface roughness parameter that is realistic with respect to the amplitudes and frequencies of the terrain, invariant with respect to rotation and translation, and has intuitive meaning. The procedure allows for a more accurate quantification of a region's convexity/concavity over varying scales, distinguishing between shallow and deep incisions, and hence provides a more accurate surface roughness parameter.

Keywords: *Scale independent surface roughness; multiscale digital elevation models (DEMs); convex and concave regions; physiographic features.*

1. INTRODUCTION

Roughness is a measure of the texture of a surface. It is quantified by the vertical deviations of a real surface from its ideal form. If these deviations are large, the surface is rough; if they are small, the surface is smooth. Surface roughness is a useful tool for terrain analysis as it reflects numerous geophysical parameters, such as landform characteristics, distribution of crenulations and degree of erosivity. Hence, in the past few decades, the quantitative computation of surface roughness of terrains for the purposes of numerical surface study has received increasing attention. Hoffman and Krotkov (1989) reported that surface roughness measurements must have the following properties:

i. Must discriminate between surfaces of different amplitudes, frequencies, and correlation
ii. Be an intrinsic property of the surface, invariant with respect to rotation or translation
iii. Be a local, not a global measure of the surface
iv. Have intuitive or physical meaning.

A number of algorithms have been employed to compute surface roughness of terrains; a summary can be found in Shepard *et al.* (2001) and Li *et al.* (2005). The most commonly used roughness parameter, and the easiest to obtain, is the root-mean-square (RMS) height, or the standard deviation of heights above the mean (Brock, 1983; Bennett, 1992; Yokota *et al.,* 2008). The profile is first detrended by subtracting a best fit linear function from the data, leaving a series of heights with a mean value of zero. This approach is insensitive to amplitude differences and is not a good frequency discriminator, and hence, is unable to provide an accurate surface roughness parameter. An alternative approach is to fit a plane to a surface, and use the error as an estimate of the surface roughness (Wilcox and Gennery, 1987). In the case of two sinusoidal surfaces of differing frequencies, plane fitting suffers from a fundamental shortcoming by producing the same roughness estimation. Stone and Dugundji (1965) proposed a method of computing surface roughness using Fourier analysis. This method measures roughness along specific directions of a surface, and includes amplitude, frequency and autocorrelation terms. This approach provides surface roughness parameters that have consistent representation in the frequency domain. However, as it depends on the direction of measurement, it is influenced by the rotation and translation of the surface. The slope and intercept of the logarithmic plot of the power spectrum of the terrain profile is reported as a roughness parameter by van Zyl *et al.* (1991). However, there is no simple correspondence between the intercept or the slope of the logarithmic plot of the power spectrum and commonly used roughness measures. Other reported roughness measures, developed to overcome these shortfalls, include effective slope (Miller and Parsons, 1990; Campbell and Garvin, 1993), autocorrelation length (Turcotte, 1997), radiosity models (Li et al., 1998), median and absolute slope (Kreslavsky and Head, 1999), granulometry (Tay *et al.*, 2005), high-order statistics (Nikora, 2005), and extended Kalman filtering (Dabrowski and Banaszkiewicz, 2008). These algorithms, which operate at singular scales of measurement, provide scale-dependant roughness parameters.

Dinesh *et al.* (2008a) proposed a procedure to compute a scale-independent surface roughness parameter from digital elevation models (DEMs). First, multiscale DEMs are generated using the lifting scheme. The area of pixels modified at each scale is computed. The computed areas are divided with the area of the DEM to obtain the normalized probability functions, which are used to compute the average size of convex and concave regions in the DEM, and the scale-independent average roughness of the terrain of the DEM due to the distribution of convex and concave regions in the terrain. Dinesh *et al.* (2008b) extended this methodology to perform the computation of surface roughness of individual mountain objects extracted from DEMs.

In this paper, the methodologies proposed by Dinesh *et al.* (2008a,b) is extended to perform the computation of scale-independent surface roughness of individual pixels of DEMs. The quantitative computation of surface roughness employed in this paper will have important applications in modelling landform character and processes, and in determining terrain trafficability.

2. THE GLOBAL DIGITAL ELEVATION MODEL (GTOPO30) OF GREAT BASIN

The DEM in Figure 1 shows the area of Great Basin, Nevada, USA. The area is bounded by latitude 38° 15’ to 42° N and longitude 118° 30’ to 115° 30’W. The DEM was rectified and resampled to 925m in both x and y directions. The DEM is a Global Digital Elevation Model (GTOPO30) and was downloaded from the USGS GTOPO30 website (GTOPO30, 1996). GTOPO30 DEMs are available at a global scale, providing a digital representation of the Earth’s surface at a 30 arc-seconds sampling interval. The land data used to derive GTOPO30 DEMs are obtained from digital terrain elevation data (DTED), the 1-degree DEM for USA and the digital chart of the world (DCW). The accuracy of GTOPO30 DEMs varies by location according to the source data. The DTED and the 1-degree dataset have a vertical accuracy of ± 30m while the absolute accuracy of the DCW vector dataset is ±2000m horizontal error and ±650m vertical error (Miliaresis and Argialas, 2002). Tensional forces on the terrain’s crust and thins by normal faulting cause the formation an array of tipped mountain blocks that are separated from broad plain basins, producing a basin-and-range physiography (Howell, 1995; Summerfield, 1996, 2000; and Argialas, 1999; Miliaresis, 2008).

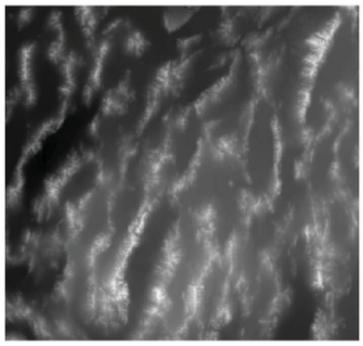

Figure 1: The GTOPO30 DEM of Great Basin. The elevation values of the terrain (minimum 1005 meters and maximum 3651 meters) are rescaled to the interval of 0 to 255 (the brightest pixel has the highest elevation). The scale is approximately 1:3,900,000.

3. GENERATION OF MULTISCALE DEMS USING THE LIFTING SCHEME

Scale variations can constrain the detail with which information can be observed, represented and analyzed. Changing the scale without first understanding the effects of such an action can result in the representation of patterns or processes that are different from those intended (Robinson *et al.*, 1984; Lam and Quattrochi, 1992; Goodchild and Quattrochi, 1997; Lam *et al.*, 2004; Summerfield, 2005). Hence, feature detection and characterization often need to be performed at different of scales measurement. Wood (1996a, b) demonstrated that analysis of a location at multiple scales allows for a greater amount of information to be extracted from a DEM about the spatial characteristics of a feature. The term scale refers to combination of both spatial extent, and spatial detail or resolution (Goodchild and Quattrochi, 1997; Tate and Wood, 2001; Li *et al.*, 2005).

In this paper, multiscaling is performed using the lifting scheme (Sweldens, 1996, 1997). The lifting scheme is a flexible technique that has been used in several different settings, for easy construction and implementation of traditional wavelets and of second generation wavelets, such as spherical wavelets. Although several the lifting scheme has proven to be a powerful multiscale analysis tool in image and signal processing (Claypoole and Baraniuk, 2000; Starck, 2002; Guo *et al.*, 2008), it is rarely used for multiscale analysis in GIS applications. Lifting consists of the following three basic operations:

Step 1: Split

The original data set $x[n]$ is divided into two disjoint subsets, even indexed points $x_e[n]=x[2n]$, and odd indexed points $x_0[n]=x[2n+1]$.

Step 2: Predict

The odd and even subsets are often highly correlated. This correlation structure typically local and hence, it is possible to accurately predict the wavelet coefficients $d[n]$ as the error in predicting $x_0[n]$ from $x_e[n]$ using the prediction operator P:

$$d[n] = x_o[n] - P(x_e[n] \tag{1}$$

where

$$P(x_e[n] = \frac{1}{2}(x_e[n] + x_e[n+1] \tag{2}$$

Step 3: Update

Scaling coefficients $c[n]$ that represent a coarse approximation to the signal $x[n]$ are obtained by combining $x_e[n]$ and $d[n]$. This is accomplished by applying an update operator U to the wavelet coefficients and adding to $x_e[n]$:

$$c[n] = x_e[n] + U(d[n]) \tag{3}$$

where

$$U(d[n]) = \frac{1}{4}(d[n-1] + d[n+1]) \tag{4}$$

These three steps form a lifting stage. The lifting scheme scans 2D images row-by-row. Using a DEM as the input, an iteration of the lifting stage generates the complete set of multiscale DEMs $c_r[n]$ and the elevation loss caused by the change of scale $d_r[n]$.

Multiscale DEMs of the Great Basin region are generated by implementing the lifting scheme on the DEM of Great Basin using scales r of 1 to 20. As shown in Figure 2, as the scale increases, the merge of small regions into the surrounding grey level regions increases, causing removal of fine detail in the DEM. As a result, the generated multiscale DEMs possess lower resolutions at higher degrees of scaling.

The fine detail in DEMs represents crenulations, which are used to extract hydrological features from DEMs. Convex crenulations are used to extract ridge networks while concave crenulations are used to extract drainage networks (Gilbert, 1909; Howard, 1994; Rodríguez-Iturbe and Rinaldo, 1997; Sagar *et al.*, 2003). The distribution of convex and concave regions in a terrain indicates the surface roughness of the terrain. The removal of convex and concave regions from the terrain during the multiscaling process results in the terrain becoming smoother. It is observed in Figure 3 that as the scale increases, the area of individual convex and concave regions increase, while the number of individual convex and concave regions decrease. This observation indicates that the development of an accurate surface roughness parameter requires an accurate quantification of a region's convexity/concavity over varying scales, distinguishing between shallow and deep incisions of the terrain.

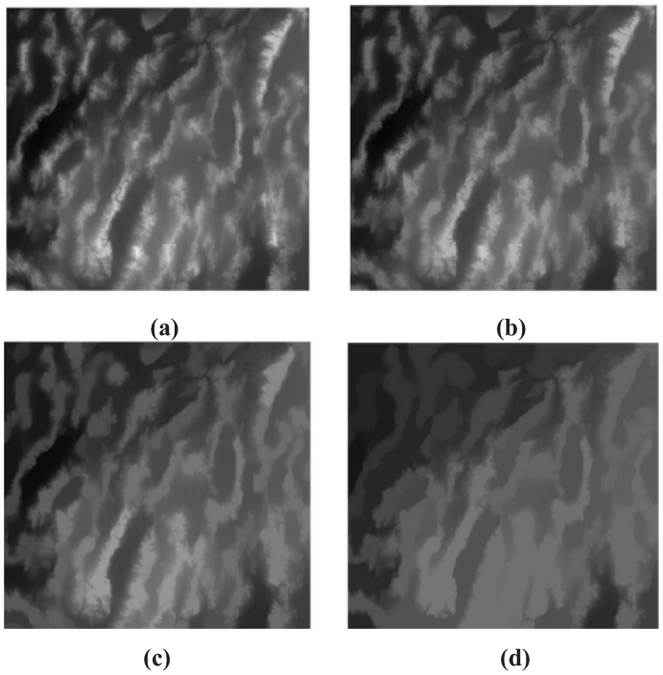

Figure 2: Multiscale DEMs generated using scales of (a) 3 (b) 5 (c) 10 (d) 20.

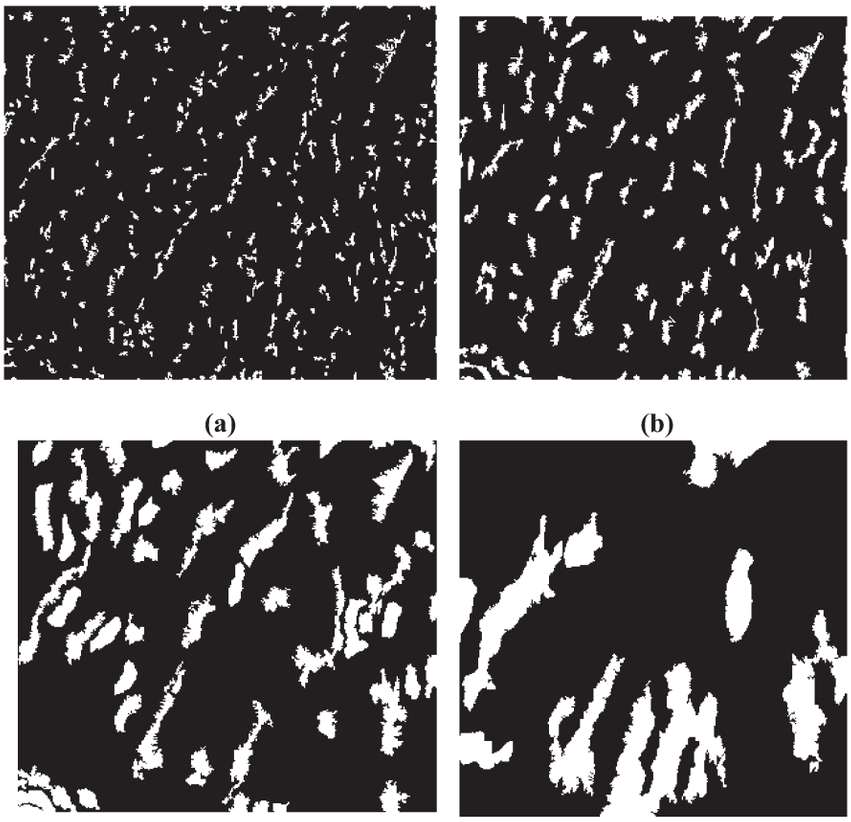

Figure 3: Mask of pixels modified during the multiscaling process for the corresponding multiscale DEMs in Figure 2. This indicates the convex and convex regions removed from the DEM during the multiscaling process.

4. COMPUTATION OF SCALE-INDEPENDENT SURFACE ROUGHNESS

For each scale r, the area of pixels modified $S(r)$ is computed. The normalized probability functions $s(r)$ are computed as the ratio of the areas of pixels modified to the area of the original DEM S_0.

$$s(r) = S(r) / S_0 \tag{5}$$

A larger value of *s(r)* indicates a larger area of convex and concave regions removed at scale r. The computed values of $s(r)$ are used to compute two important grayscale granulometric complexity measures:

1) **Average size *n***: Indicates the average size of convex and concave regions in the DEM.
2) **Average roughness *H***: Indicates surface roughness of the terrain of the DEM due to the distribution of convex and concave regions in the DEM.

The measures n and H are computed using the following equations, which are due to Maragos (1989):

$$n = \sum_{r=`}^{20} rs(r) \tag{6}$$

$$H = \sum_{r=`}^{20} s(r) \log s(r) \tag{7}$$

For the given DEM, the computed values for n and H are 42.038 and 2.341, respectively. The proposed procedure takes into account the amplitudes and frequencies of the terrain, ensuring a realistic measure of the roughness of the terrain. As the proposed procedure does not depend on direction of measurement, it is invariant with respect to rotation and translation. The parameters n and H are intuitive; surfaces with large amplitudes have larger values of n and H as compared to surfaces with smaller amplitudes. The proposed procedure takes into account the removal of convex and concave regions across multiple scales, and is as able to provide a scale-independent roughness parameter.

In order to demonstrate the importance of scale-independent surface roughness computation, the surface roughness of the terrain over varying scales of measurement is computed using a commonly used scale-dependent surface roughness parameter; RMS height (Brock, 1983; Hoffman and Krotkov, 1989; Bennett, 1992; Shepard et al., 2001; Li *et al.*, 2005; Yokota et al., 2008). It is observed in Figure 4 that as the scale is increased, the surface roughness of the terrain reduces due to the reduction of fine detail in the generated multiscale DEMs. Scale-dependant roughness parameters only consider convex and concave regions at singular scales, at fixed levels of incisions, and hence, vary significantly according to scale. The proposed methodology allows for a more accurate quantification of a region's convexity/concavity over varying scales, distinguishing between shallow and deep incisions, and hence provides a more accurate surface roughness parameter.

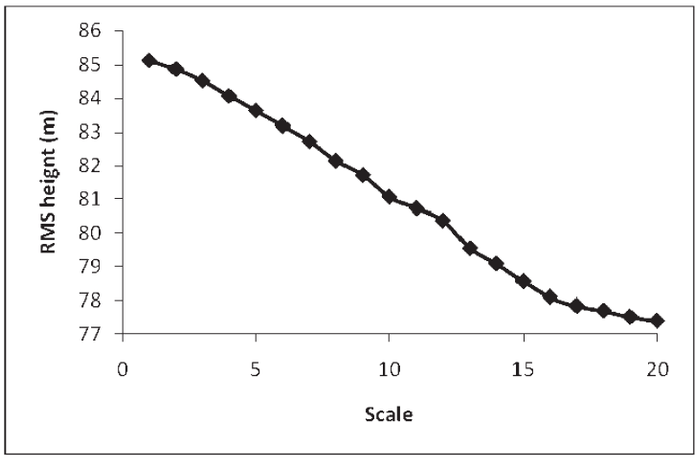

Figure 4: Surface roughness of the terrain the varying scales of measurement via RMS height.

5. DIRECT COMPUTATION OF SURFACE ROUGHNESS OF INDIVIDUAL PIXELS

Based on grayscale granulometry, the roughness of the individual pixels H_{ij} is computed as:

$$H_{ij} = \sum_{r=`}^{20} s_{ij}(r) \log s_{ij}(r) \tag{8}$$

where $s_{ij}(r)$ is the normalized probability function of the pixel; $s_{ij}(r)=1$ when the pixel is modified at scale r, and $s_{ij}(r)=0$ when the pixel is not modified at scale r.

However, as log 1=0, this equation is not practical. Alternatively, H_{ij} is computed as follows:

$$H_{ij} = cn_{ij} \tag{9}$$

where c is the terrain's roughness coefficient, and n_{ij} is the size of convex and concave regions for each individual pixel.

$$c = n / H \tag{10}$$

$$n_{ij} = \sum_{r=`}^{20} rs_{ij}(r) \tag{11}$$

The computed surface roughness of the individual pixels of the DEM is shown in Figure 5. The disadvantage of the methodology to compute individual pixel surface roughness is that it assumes that convex and concave regions are equally distributed throughout the terrain. However, convex and concave regions are more highly distributed in mountain regions compared to non-mountain regions. In order to demonstrate the drawback of the present methodology, three models are used (Figure 6). All three models use singular mountains with size 100 x 100 pixels, but have different backgrounds sizes; 200 x 200 pixels, 300 x 300 pixels, and 400 x 400 pixels.

For the non-mountain region of each model, being completely flat, the pixels would have roughness values of 0. As the mountain in each is DEM is exactly the same, each mountain pixel should have the same roughness value as the corresponding pixel in the other DEMs. However, it is observed in Figure 8 that using the current methodology, the mountains in all 3 models have different roughness values. As the background size is increased, the distribution of the convex and concave regions is more concentrated in the mountain region, resulting in an increase of the roughness coefficient, and an increase in surface roughness values.

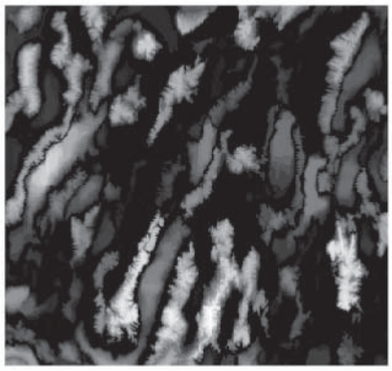

Figure 5: The computed surface roughness of the individual pixels of the DEM. The surface roughness values (ranging from 0 to 11.646) are rescaled to the interval of 0 to 255 (the brightest pixel has the highest membership value).

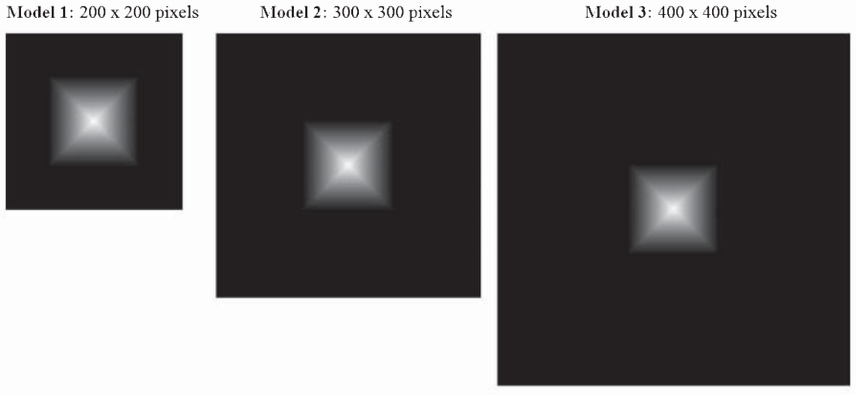

Figure 6: Three model DEMs using the same singular mountain with size 100 x 100 pixels, but having different backgrounds sizes; 200 x 200 pixels, 300 x 300 pixels, and 400 x 400 pixels.

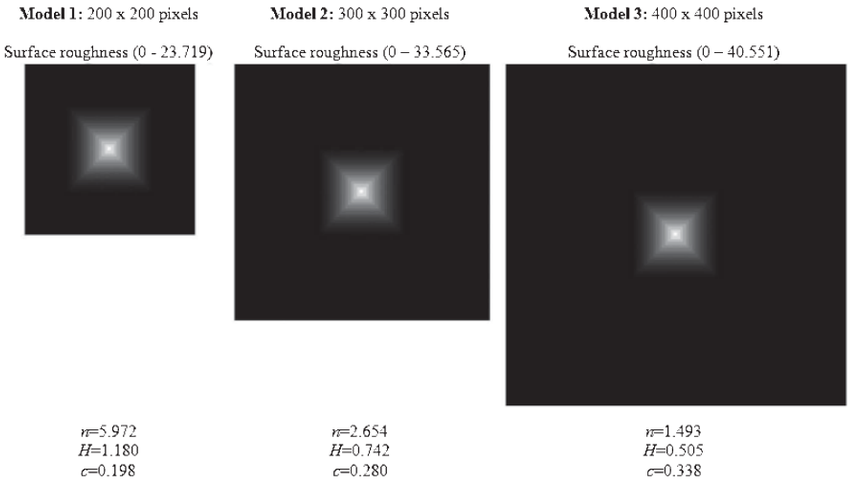

Figure 7: The computed surface roughness of the individual pixels of the corresponding models in Figure 6.

6. COMPUTATION OF SURFACE ROUGHNESS OF INDIVIDUAL PIXELS OF SPECIFIC REGIONS

In order to rectify this problem, the algorithm has to be modified to compute the surface roughness at specific regions, to ensure the roughness values reflect the convex and concave region distribution in each region. For the case of the DEM of Great Basin DEM, the 3 predominant physiographic features, mountains, basins and piedmont slopes, have distinct roughness characteristics. Physiography (also known as land surface characteristics) refers to the study of physical features and attributes of the earth's land surface. The detection of the physiographic features of a terrain is the first phase involved in the classification of the various landforms of the terrain.

The mountains (Figure 8(a)), basins (Figure 8(b)) and piedmont slopes (Figure 8(c)) of the DEM are extracted using the mathematical morphological based physiographic segmentation algorithm proposed in Dinesh *et. al* (2007). Ultimate erosion is used to extract the peaks and pits of the DEM. Conditional dilation is performed on the peaks and pits of the DEM to obtain the mountain and basin pixels respectively. The pixels that are not classified as mountain pixels or basin pixels are assigned as piedmont slope pixels. Surface roughness values need to be computed for the distinct individual mountains (14), basins (13) and piedmont slopes (666).

The procedure proposed to perform the computation of surface roughness of the individual mountain objects is demonstrated using the first mountain object (Figure 9). The mask of pixels modified in the each mountain object at each scale (Figure 10) is computed by performing the intersection operation between the mountain object and the mask of pixels modified at each scale. The normalized probability functions of the mountain object $s_m(r)$ are computed as the ratio of the area of pixels modified in the mountain object at each scale $S_m(r)$ to the area of the mountain object S_{m0}.

$$s_m(r) = S_m(r) / S_{m_0} \tag{12}$$

The computed values of $s_m(r)$ are used to average size of convex and concave regions of the mountain n_m, and the average roughness of the mountain H_m:

$$n_m = \sum_{r=`}^{20} r s_m(r) \tag{13}$$

$$H_m = \sum_{r=`}^{20} s_m(r) \log s_m(r) \tag{14}$$

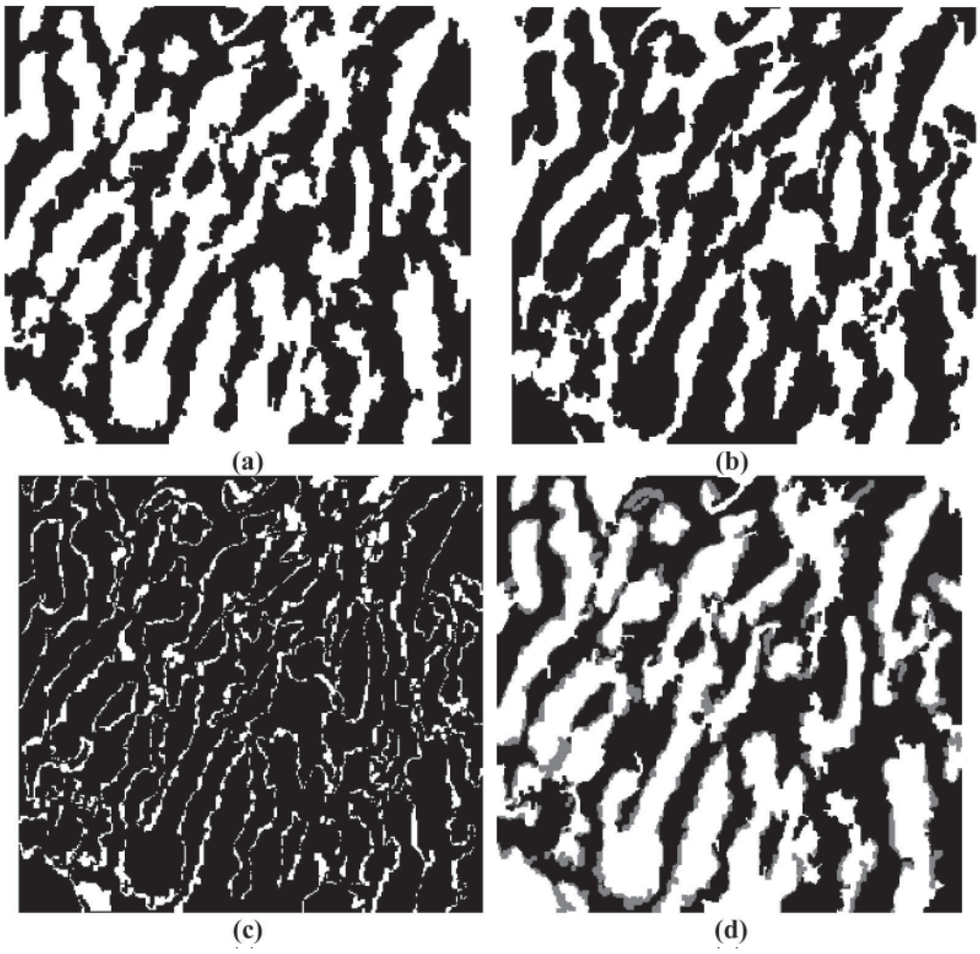

Figure 8: Physiographic segmentation of the terrain of the DEM. (a) Mountains (b) Basins (c) Piedmont slopes (d) The physiographically segmented DEM; the mountains pixels are the in white, the piedmont pixels are the pixels in grey and the basin pixels are the pixels in black.

Figure 9: The first mountain object.

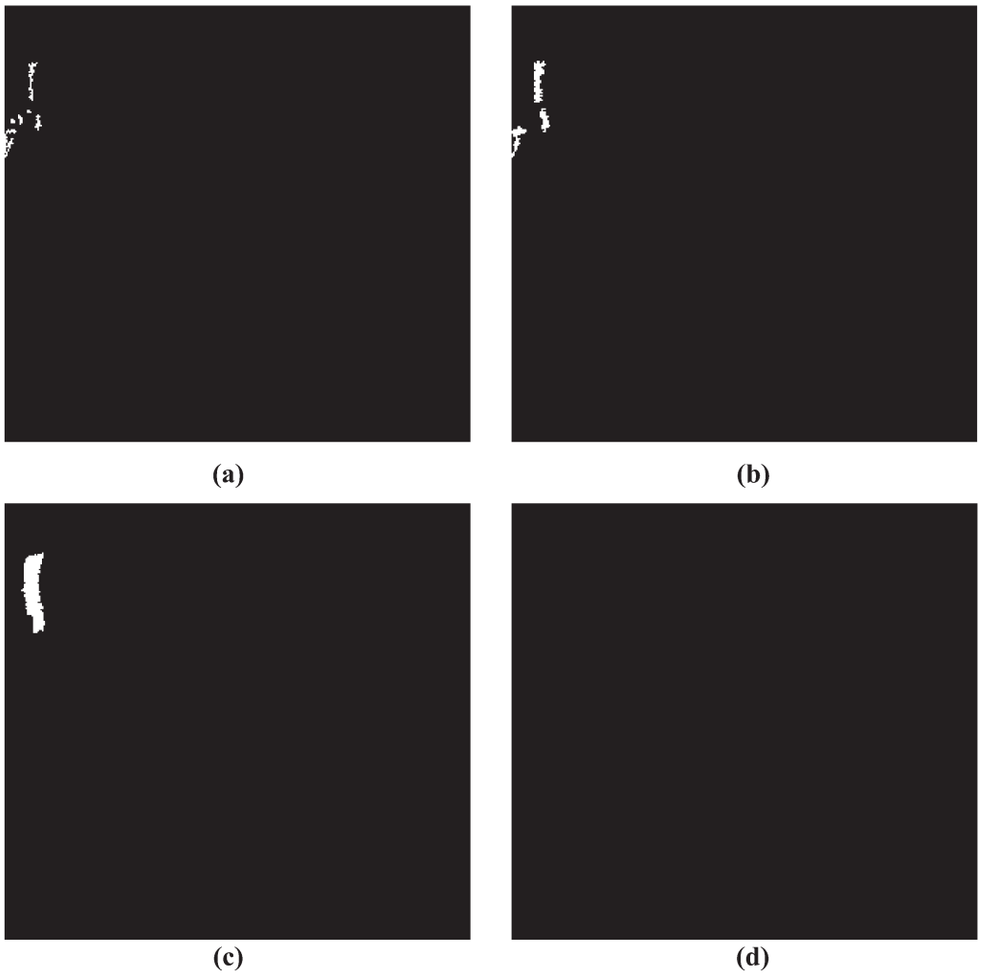

Figure 10: The mask of pixels modified in the first mountain object during the multiscaling process for the corresponding multiscale DEMs in Figure 2. This indicates the convex and convex regions removed from the mountain object during the multiscaling process.

The values of n_m and H_m for the first mountain object are computed to be 108.412 and 1.795, respectively. The mountain's roughness coefficient c_m is computed to be 0.017.

$$c_m = n_m / H_m \tag{15}$$

The surface roughness of the individual pixels of the mountain H_{mij} is computed. The methodology is applied to compute the surface roughness of the individual pixels of the remaining individual mountains, basins and piedmont slopes. The computed surface roughness values are shown in Figure 11.

$$H_{m_{ij}} = c_m n_{m_{ij}} \tag{16}$$

The validity of the revised methodology is verified using the models in Figure 6. As observed in Figure 12, the surface roughness values of the mountain pixels for the three models are the same, indicating that the revised methodology is able distinguish between regions of varying degrees of distributions of convex and concave regions.

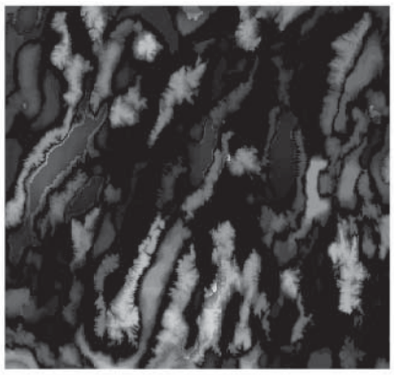

Figure 11: Surface roughness of the individual pixels of the DEM computed using the revised methodology. The surface roughness values (ranging from 0 to 11.500) are rescaled to the interval of 0 to 255 (the brightest pixel has the highest membership value).

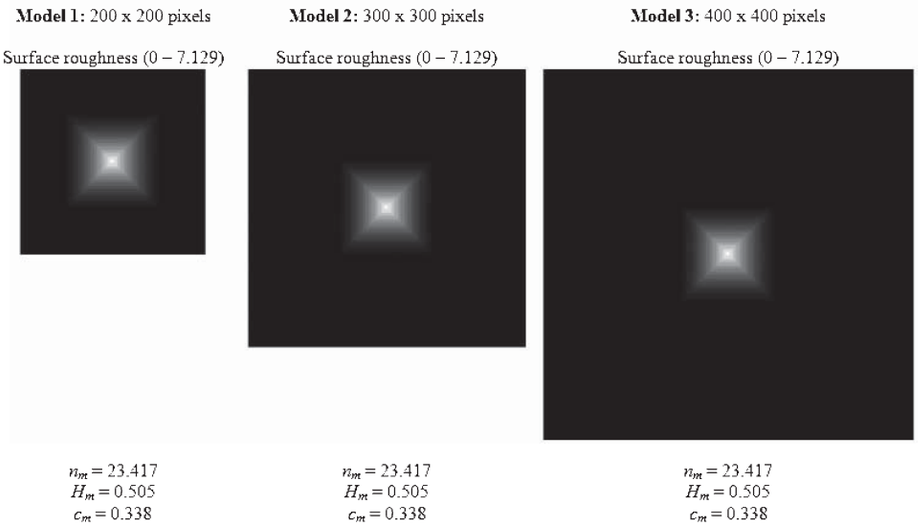

Figure 12: Surface roughness of the individual pixels of the corresponding models in Figure 7 computed using the revised methodology.

7. CONCLUSION

In this paper, a procedure to perform the computation of the scale-independent surface roughness of individual pixels of DEMs was proposed. Mathematical morphology is employed to segment the terrain of a DEM into the three predominant physiographic features; mountains, basins and piedmont slopes. The lifting scheme is used to generate multiscale DEMs. The mask of pixels modified in each distinct individual landform at each scale is computed by performing the intersection operation between the landform and the mask of pixels modified at each scale. The normalized probability functions for each landform are computed as the ratio of the area of pixels modified in the landform at each scale to the area of the landform. The computed normalized probability functions are used to compute the average size of convex and concave regions in the landform, the scale-independent average roughness of the landform due to the distribution of convex and concave regions averaged over the landform, and the landform's roughness coefficient. The surface roughness of each individual pixel in the landform is computed by multiplying the roughness coefficient with the pixel's area of convex and concave regions. The proposed procedure provides a surface roughness parameter that is realistic with respect to the amplitudes and frequencies of the terrain, invariant with respect to rotation and translation, and has intuitive meaning. The procedure allows for a more accurate quantification of a region's convexity/concavity over varying scales, distinguishing between shallow and deep incisions, and hence provides a more accurate surface roughness parameter.

ACKNOWLEDGEMENTS

The author is grateful to Prof. Ir. Dr. Ahmad Fadzil Hani and Dr. Vijanth Sagayan a/l Asirvadam, both from the Department of Electrical and Electronics Engineering, Universiti Teknologi Petronas, Malaysia, and Dr. George Miliaresis, University of Patras , Greece for their suggestions that have helped improve the technical content of this article.

REFERENCES

Bates, R.L. & Jackson, J.A. (Eds.) 1987. Glossary of Geology. American Geological Institute, Virginia.

Bennett, J.M. (1992). Recent developments in surface roughness characterization. *Meas. Sci. Technol.*, **3**: 1119-1127.

Brock, M. (1983). Surface Roughness Analysis. Brüel & Kjær Instruments Inc., Nærum, Denmark.

Campbell, B.A & Garvin, J.B. (1993). Lava flow topographic measurements for radar data interpretation, Geophys. Res. Lett., **20**: 831-834.

Claypoole, R.L. & Baraniuk, R.G., 2000. A multiresolution wedgelet transform for image processing. *In* Unser, M.A., Aldroubi, A. and Laine, A.F. (Eds.). Wavelet Applications in Signal and Image Processing VIII, Volume 4119 of SPIE Proceedings, 253-262.

Dabrowski, B. & Banaszkiewicz, M. (2008). Multi-rover navigation on the lunar surface. *Adv. Space Res.*, **42**: 369-378.

Dinesh, S., Fadzil, M.H.A. & Vijanth Sagayan, A. (2008). Computation of scale-independent surface roughness via the generation of multiscale digital elevation models. *International Conference on Computer & Communication Engineering 2008 (ICCCE08)*, 13th-15th May 2008, Istana Hotel, Kuala Lumpur.

Dinesh, S., Fadzil, M.H.A. & Vijanth Sagayan, A. (2008). Computation of scale-independent surface roughness of individual mountains. *Map Asia 2008*, 18th-20th Aug. 2008, Kuala Lumpur Convention Centre (KLCC), Kuala Lumpur.

Dinesh, S., Radhakrishnan, P. & Sagar, B.S.D. (2007). Morphological segmentation of physiographic features from DEM. *Int. J. Remote Sens.*, **28:** 3379 - 3394.

Gilbert, G.K. (1909). The convexity of geology. *J. Geol.*, **17**: 344-350.

Goodchild, M.F. & Quattrochi, D.A., 1997. Scale, multiscaling, remote sensing and GIS. *In* Quattrochi, D.A. and Goodchild, M.F. (Eds.). Scale in Remote Sensing and GIS. Lewis Publishers, Boca Raton, Florida, 1-11.

Guo, S.M., Chang, .H., Tsai, J.S.H., Zhuang, B.L. & Chen, L.C. (2008). JPEG 2000 wavelet next term filter design framework with chaos evolutionary programming. *Sign. Proces.*, **88**: 2542-2553.

Graff, L.H. & Usery, E.L. (1993). Automated classification of generic terrain features in digital elevation models. *Photogrammetric Eng. Remote Sens.*, **59**: 1409-1417.

Hoffman, R. & Krotkov, E., 1989. Terrain roughness measurement from elevation maps. *SPIE Vol. 1195 Mobile Robots IV*, 104-114.

Howard, A.D. (1994). A detachment-limited model of drainage basin evolution. *Water Resour. Res.*, **30**: 2261-2285.

Howell, D. (1995). Principles of Terrain Analysis: New Applications for Global Tectonics. Chapman and Hall, London.

Kreslavsky, M.A & Head, J.W. (1999). Kilometer-scale slopes on Mars and their correlation with geologic units: Initial results from Mars Orbiter Laser Altimeter (MOLA) data. *J. Geophys. Res.*, **104**: 21,911-21,924.

Lam, N. & Quattrochi, D. (1992). On the issues of scale, resolution, and fractal analysis in the mapping science. Prof Geog., **44**: 88-98.

Lam, N., Catts, D., Quattrochi, D, Brown, D. & McMaster, R. (2004). Scale. *In* Rechcígl, M., McMaster, R.B., and Usery, E.L (Eds.). A Research Agenda for Geographic Information Science. CRC Press, New York.

Li, W.-H., Weeks, R. & Gillispie (1998). Multiple scattering in the remote sensing of natural surfaces. *Int. J. Remote Sens.*, **19**: 1725 – 1740.

Li, Z., Zhu, Q. & Gold, C. (2005). Digital Terrain Modelling: Principles and Methodology. CRC Press, New York.

Maragos, P. (1989). Pattern spectrum and multiscale shape representation. *IEEE Trans. Pattern Anal. Mach. Intel.*, **11**: 701-716.

Miliaresis, G. C. (2000). The DEM to mountain transformation of Zagros Ranges. *5th International Conference on GeoComputation*, 23-25 of August 2000, University of Greenwich.

Miliaresis G. (2008). Quantification of terrain processes. *Lecture Notes in Geoinformation & Chartography*, **Vol. XIV**: 13-28.

Miliaresis, G.C. & Argialas, D.P. (1999). Segmentation of physiographic features from Global Digital Elevation Model/GTOPO30. *Comput. Geosci.*, **25**: 715-728.

Miliaresis, G.C., & Argialas, D.P. (2002). Quantitative representation of mountain objects extracted from the Global Digital Elevation Model (GTOPO30). *Int. J. Remote Sens.*, **23**: 949-964.

Miller, L.S. and Parsons, C.L. (1990). Rough surface scattering results based on bandpass autocorrelation forms. *IEEE Trans. Geosci. Remote Sens.*, **28**: 1017-1021.

Nikora, V. (2005). High-order structure functions for planet surfaces: A turbulence metaphor. *IEEE Trans. Geosci. Remote Sens.*, **2**: 362-365.

Robinson, A.H., Sale, R.D., Morrison, J.L. & Muehrcke, P.C. (1984). Elements of Cartography. John Wiley & Sons, New York.

Rodríguez-Iturbe, I. & Rinaldo, A. (1997). Fractal River Basins: Chance and Self-Organization. Cambridge University Press, New York.

Shepard, M.K., Campbell, B.A., Bulmer, M.H., Farr, T.G., Gaddis, L.R. & Plaut, J.J. (2001). The roughness of natural terrain: A planetary and remote sensing perspective. *J. Geophys. Res.*, **106**: 32,777-32,795.

Stone, R. and Dugundji, J. (1965). A study of microrelief: Its mapping, classification and quantification by means of a Fourier analysis. *Eng. Geol.*, **1**: 89-187.

Summerfield, M. (1996). Global Geomorphology. Longman, Essex.

Summerfield, M. (Ed.) (2000). Geomorphology and Global Tectonics. John Wiley & Sons, New York.

Summerfield, M.A. (2005). A tale of two scales, or two geomorphologies. Trans. Inst. Bri. Geog., **30**: 402-415.

Sweldens, W. (1996). The lifting scheme: A custom-design construction of biothorgonal wavelets. *App. Comput. Harmonics Anal.*, **3**: 186-200.

Sweldens, W., 1997. The lifting scheme: A construction of second generation wavelets. *J. Math. Anal.*, **29**: 511-546.

Tate, N. & Wood, J. (2001). Fractals and scale dependencies in topography. *In* Tate, N. and P. Atkinson (Eds.). Modelling scale in geographical information science. Wiley, Chicester, 35-51.

Tay, L.T., Sagar, B.S.D. & Chuah, H.T. (2005). Derivation of terrain roughness indicators via granulometries. *Int. J. Remote Sens.*, **24**: 573-581.

Turcotte, D.L., 1997. Fractals and Chaos in Geology and Geophysics. Cambridge University Press, New York.

van Zyl, J.J., Burnette, C.F. and Farr, T.G. (1991). Inference of surface power spectra from inversion of multifrequency polarimetric radar data. Geophys. Res. Lett., **18**: 1787-1790.

Wilcox, B. & Gennery, D. (1987). A Mars rover for the 1990's. *J. Bri. Planet. Soc.*, **40**: 484-488.

Wood, J. (1996a). Scale-based characterization of digital elevation models. *In* Parker, D. (Eds.) Innovation in GIS 3. Taylor & Francis, London, 163-175.

Wood, J. (1996b). The geomorphological characterization of digital elevation models. PhD Thesis, Department of Geography, University of Leicester, Leicester.

Yokota, Y., Haruyama, J., Honda, C., Morota T., Ohtake, M., Kawasaki, H., Hara, S., Hioki, K & the LISM Working Group (2008). Lunar topography: Statistical analysis of roughness next term on a kilometer scale. *Adv. Space Res.*, **42**: 259-266.

AN OVERVIEW ON CONDITION BASED MONITORING BY VIBRATION ANALYSIS

Abdul Hamid Hassan*, Adam Hj Gani & Shamsul Akmar Ab Aziz

Mechanical & Aerospace Technology Division,
Science & Technology Research Institute for Defence (STRIDE),
Taman Bukit Mewah Fasa 9, 43000, Kajang, Selangor D.E.
Tel: 03-87324511
Fax: 03-87336219
*E-mail: ahh3884@yahoo.com

Abstract

One of the methods to achieve mission availability is through the proper maintenance of aerial platforms. An alternative concept in the maintenance of these aerial platforms, particularly rotating parts, is by using vibration analysis. Vibration monitoring is commonly understood to be a form of condition monitoring used extensively in the aerospace industry to monitor engines, transmissions and gearboxes to detect faults before they develop into catastrophic failures. Some applications simply wear out of excessive vibration levels, while others are able to match the vibration signatures of known failure modes. Given the safety and cost implications of catastrophic failures in these helicopter components, investment payback can be achieved if such failures are avoided. This project is focused on the AGUSTA helicopter used by Pasukan Udara Tentera Darat (PUTD), where regular vibration measurements are taken at the main gearbox while monitoring the vibration trending. By the analysing the vibration spectra, the engineer can predict when a component is going to fail, and hence the necessary remedies and actions can be taken.

Keywords: *Condition Based Monitoring; Vibration Analysis; Pasukan Udara Tentera Darat (PUTD); AGUSTA helicopter.*

1. INTRODUCTION

Changes in the concept of operations of the Malaysian Armed Forces (MAF) have led to the need for better information and management concerning aerial platforms to deliver enhanced fighting power. Key objectives within the new concepts are to achieve better mission availability in the theatre, reduce the in-theatre logistic burden, and make more effective use of aerial platforms. These objectives must be achieved within an environment that continues to emphasise the need to minimise whole life costs.

One method to achieve mission availability is the proper maintenance of these aerial platforms. An alternative concept in maintenance of these aerial platforms, particularly rotating parts, is by using vibration analysis (Bramwell *et al*., 2001).

Research in the nature of the vibration data collected from the AGUSTA helicopter's transmission during test flight experiments has led to several crucial observations believed to be responsible for the high rates of false alarms and missed detections in aircraft vibration monitoring systems. This work focuses on one such finding, namely, the need to consider additional sources of information about system vibrations. AGUSTA helicopter transmission vibration data are measured and collected using triaxial accelerometers in three different directions. The vibration level content and frequency of the three different directions is compared and analyzed using time synchronously.

2. VIBRATION ANALYSIS ASSESSMENT

Vibration monitoring is commonly understood to be a form of condition monitoring used extensively in the aerospace industry. The aims are to monitor engines, transmissions and gearboxes to detect faults before they develop into catastrophic failures. Some applications simply wear out of excessive vibration levels, while others are able to match the vibration signatures of known failure modes. Given the safety and cost implications of catastrophic failures in these aerospace components, investment payback can be achieved even if such failures are avoided (Shikari & Sadiwala, 2004).

This method considers each machine or component individually by replacing fixed-interval maintenance based on fixed-interval vibration measurements of the machines or components. The development in the running condition of each individual machine or component can be monitored closely as the mechanical vibration is a good indicator of a machine's running condition.

Faulty conditions can be detected by means of regular vibration measurements. Measurements can be extrapolated in order to predict when unacceptable vibration levels will be reached and when the machine needs to be serviced. This approach allows the engineer to plan repairs well in advance (Shikari & Sadiwala, 2004).

The predictive failure allows preventive maintenance to be conducted before actual failure occurred thus mission availability is maintained. Given sufficient warning, maintenance can take place at the optimum time for overall mission performance, and also when the required engineering and logistic resources are immediately available. Furthermore, by avoiding in-service failures, and possible secondary damage, repair costs can be greatly reduced.

3. PROJECT OBJECTIVES

The project objective is to introduce vibration analysis as one of the maintenance tools to *Pasukan Udara Tentera Darat* (PUTD). Using this method, the PUTD maintenance team will be able to detect the helicopters problematic parts based on vibration data spectra. Hence, the percentage of component failures, resources, maintenance time and costs can be reduced, while extending the serviceability and life time of the helicopters.

4. PROBLEM STATEMENT

Traditional machinery maintenance practice can be broadly categorized into two methods;-Run-to-Breakdown Maintenance and Time-Based Preventive Maintenance. In Run-to-Breakdown Maintenance, the machineries or mechanical components are usually operated until breakdown, and the loss of time is not important as spare machines can usually take over.

On the other hand, for Time-Based Preventive Maintenance, where unscheduled service stops can result in large losses, hence, maintenance operations are often performed at fixed intervals. Experience has shown that in the vast majority of cases, Time-Based Preventive Maintenance is uneconomical. A significant fact is that the failure rate of many machines is not improved by replacing wearing parts regularly in advance (Shikari & Sadiwala, 2004). As the actual failure pattern for each individual machine cannot be predicted, thus Time-Based Preventive Maintenance cannot be efficiently and effectively applied. More often than not, some of these mechanical components are still serviceable even though the service maintenance schedule shows that it is mandatory to change these mechanical components.

The Vehicle Branch, Science & Technology Research Institute for Defence (STRIDE) has been given the task to introduce Condition Based Monitoring using vibration analysis on AGUSTA helicopters as one of the maintenance tools to overcome the above mentioned problem. This concept of maintenance has not been

conducted on AGUSTA helicopters owned by PUTD. Studies have proven that this method has been successful in determining when a particular component is going to fail.

5. MEASUREMENT METHODS (METHODOLOGY)

For the purpose of this project, the vibration data will be taken every 100 flying hours on AGUSTA helicopters. The measurement will be carried out while the AGUSTA helicopter is on the ground with the engine running. The measurement technique is very important to ensure that the gear box vibration level is within safe range and does not interfere with the whole structure of the aircraft. To perform this measurement, one unit of vibration tri-axial accelerometer (Type 4504-A) will be mounted on the particular part on the gear box (Brüel & Kjær, 2007b). The surface shall be clean and free from dusts and corrosions. The existence of dusts and corrosions may reduce the efficiency of the transducer which will contribute to improper reading. The measurement will be started after 5 minutes of engine running to ensure the stability of the gear box vibration. The results will be stored, and vibration level trending will be made and analysed.

6. EQUIPMENT

To ensure the maintenance of the AGUSTA helicopter's gear box and to optimise the up-time of the aircraft, the STRIDE Vehicle Branch uses the Brüel & Kjær Aircraft Vibration Analysis System Type 3649-A. It consists of the PULSE software, portable PC, tachometer probe (Type MM0024), an accelerometer with a high-temperature cable with integrated charge converter/filter and TEDS (Type 8324-G), and a water and shockproof case (Brüel & Kjær, 2007a).

Vibration measurements are made according to the procedures specified by Turbomeca, the AGUSTA helicopter manufacturer.

Figure 1: Brüel & Kjær PULSE vibration analysis software.
(Source: Brüel & Kjær, 2007a)

Figure 2: Brüel & Kjær Type 3650-B.
(Source: Brüel & Kjær, 2007a)

7. DISCUSSION

From the results obtained, the generated vibration trending graph will be monitored closely. In order to get the data, a few measurements should be taken for analytical purposes. The graphs in Figures 3-5 show the example of polarization of trending measurement being collected. Figure 3 shows the results of a 70 second run-up on the AGUSTA helicopter's engine. The vibration trend was below the warning limit, indicating that the normal trending was observed. The data will be collected as many times as possible to determine and monitor the trending. Early detection of failure can be made by looking at the graph. If the trending shows increase in the

value of vibration levels, precautionary steps shall be taken. Any level exceeding 17.5 mm/s^2 will be notified by an alarm or indicator as shown by the red line in Figure 3. Interpretation of the data can also be made by using the graph of Vibration vs. Frequency (Figure 4). All analysed and accepted data can be generated automatically in Microsoft Word format (Figure 5).

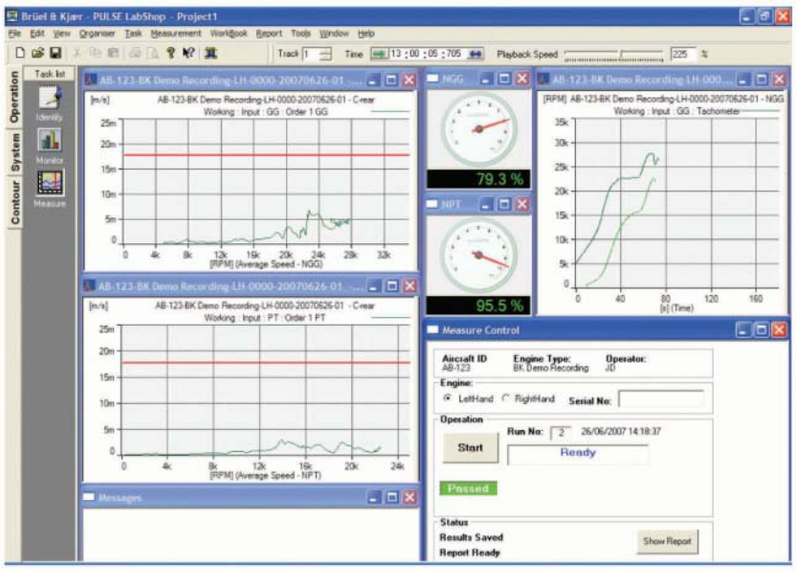

Figure 3: PULSE vibration analysis graph.
(Source: Brüel & Kjær, 2007a)

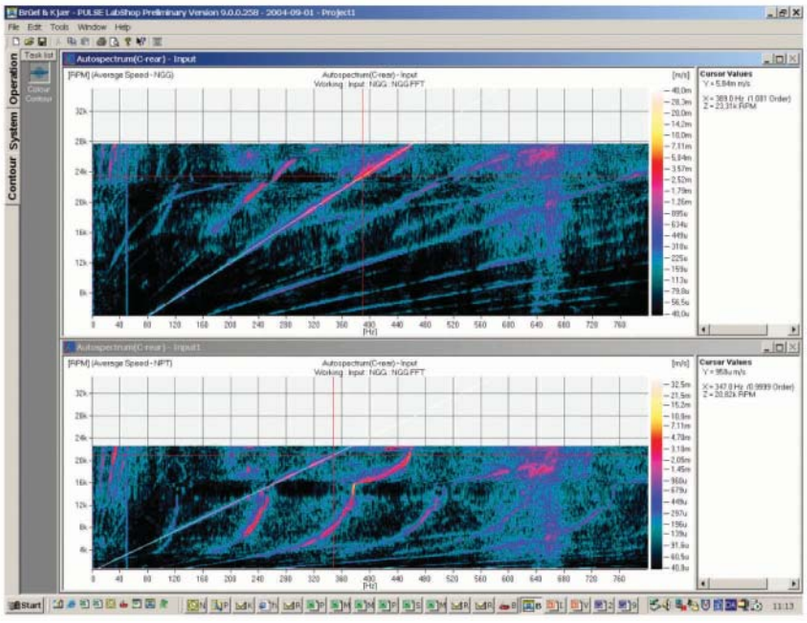

Figure 4: Vibration (mm/s^2) vs Frequency (Hz) graph.
(Source: Brüel & Kjær , 2007a)

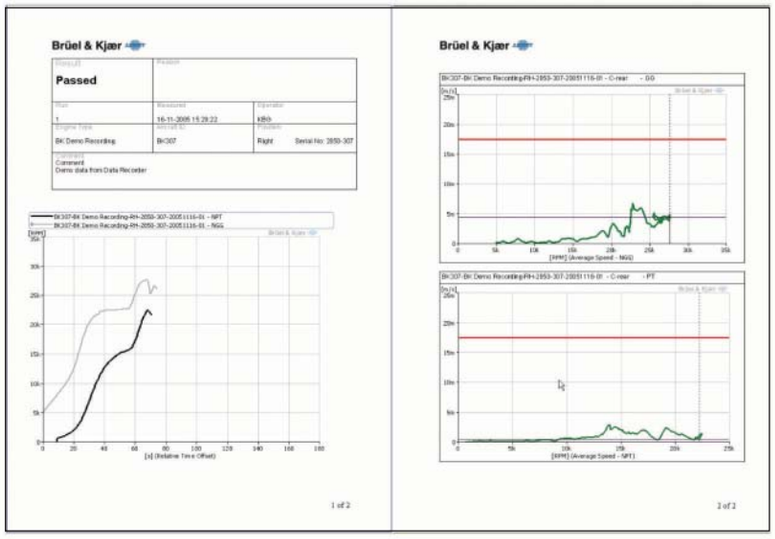

Figure 5: Generated report in Microsoft Word.
(Source: Brüel & Kjær, 2007a)

8. CONCLUSION

By performing Condition Based Monitoring using vibration analysis, the ability to detect and diagnose faulty AGUSTA helicopter conditions will be increased, thus the serviceability and life time of the helicopter will be extended. At the same time, the long term total maintenance costs can be reduced. In this project, the AGUSTA helicopter's gear box vibration data was collected using tri-axial accelerometers (Type 4504-A), was explored in three different directions, analysed for content, and then, Envelope and Order Analysis was used to analyse changes directionality. The frequency content of the three different directions was analysed using the PULSE software. The benefits of using tri-axial data for vibration monitoring and diagnostics were explored by analysing the changes in the direction of the principle axis of vibration formed using all three axes of vibration.

REFERENCES

Bramwell, A.R.S, Done, G. & Balmford, D. (2001) Helicopter Dynamics. American Institute of Aeronautics, Virginia.

Irem, Y.T. & Edward, M.H. (2004). Analyis of Triaxial Vibration Data for Health Monitoring of Helicopter Gearboxes. NASA Ames Research Center, California.

Shikari, B. & Sadiwala, C.M. (2004). Automation in Condition Based Maintenance Using Vibration Analysis. Maulana Azad National Institute of Technology, Bhopal, India.

Brüel & Kjær (2007a). Product Data. PULSE Vibration Check System for Aircraft Engine, Denmark.

Brüel & Kjær (2007b). Product Data. Accelerometer Catalogue, Denmark.

PRELIMINARY WORK ON THE DEVELOPMENT OF TETHERED AEROSTAT SYSTEM

Zainol Abidin Awang Sa*, Masliza Mustafar, Siti Rozanna Yusuff, Mohd Sal Salsidu, Noor Salwanis Saad, Ahmad Faridz Abdul Ghaffar & Nor Azman Dolah

Mechanical & Aerospace Technology Division,
Science & Technology Research Institute for Defence (STRIDE),
Taman Bukit Mewah Fasa 9, 43000, Kajang, Selangor D.E.
Tel: 03-87324506
Fax: 03-87336219
*E-mail: zaas.pst@mod.gov.my

Abstract

Tethered aerostats are currently deployed worldwide for various types of civilian, military and commercial applications. These applications include police patrol in cities, border patrol using radar, battlefield tasks, scientific research, recreation, communications, broadcasting and advertising. The applications of these lighter-than-air (LTA) vehicles and the design aspect of tethered aerostat systems are reviewed and presented in this paper. This paper also presents the results of an initial sizing study conducted as part of a preliminary work related to the development of a tethered aerostat system conducted by the Science & Technology Research Institute for Defence (STRIDE).

Keywords: *Aerostat; Surveillance; Lighter-Than-Air (LTA).*

Nomenclature

LTA = Lighter Than Air
PROPESA = Procedure for aerostat design and sizing
$Lift_{net}$ = Net lift [kg]
V_e = Envelope Volume [m^3]
ρ_{air} = Air density at off standard design pressure altitude [kg/m^3]
ρ_{LTA} = Contained gas density at off standard design pressure altitude [kg/m^3]
Pu_{LTA} = Percentage purity of the contained gas [%]
C_{DV} = Volumetric drag coefficient
l = Length of the envelope [m]
d = Diameter of the envelope [m]
Re = Reynolds number
D = Drag on the envelope [N]
v = wind speed [m/s]

1. INTRODUCTION

An aerostat is defined as a lighter-than-air aircraft that uses the buoyancy concept to produce lift to stay aloft rather than aerodynamic lifting surfaces used by heavier than air vehicles. An aerostat has three main sections; envelope, payload compartment and tethered cable. The envelope contains lifting gas (which is Helium or Hydrogen in most cases) that is required for buoyancy. It is generally categorized into three structural classes; rigid, non-rigid or semi-rigid. This envelope will be gimballed at the tether confluence point, so that it can freely align with the direction of the ambient wind. The payload compartment carries the entire aerostat payload used for operations such as radars, surveillance cameras or communication equipment. A small aerostat uses high strength rope to tether the aerostat to the ground, and in some aerostat systems, the tethered cable also provides power to the equipment on-board.

Aerostats have been used for many years in military surveillance and anti-submarine warfare. The latest development shows that there are certain applications in which aerostats have more advantages compared to other air platforms. Aerostats provide a stable and reliable platform for airborne electronics, such as surveillance radars, to give early detection and warning of unidentified flying aircrafts and missiles at its operational surroundings. It also acts as a communication relay to broadcast microwave, UHF, VHF, TV, and FM radio signals to wide areas (Amool, 2005).

In the United States, high-flying tethered aerostats are used to guard the southern border of the country under the supervision of the US Air Force. Known as “Tethered Aerostat Radar System (TARS)”, this system is used for several purposes such as surveillance on Cuba, detecting smugglers from Mexico, and maritime surveillance purposes along the Gulf of Mexico. The TARS system initially used 71 m long TCOM 71M aerostats that carried the AN/TPS-63 surveillance radar system. In the late 1990s, a 63.5 m long aerostat replaced the old system that consumed 50% more volume which carries the Lockheed Martin L-88A surveillance radar. The system could float at an altitude up to 15,000 feet. It also has the capability to spot low-flying aircrafts as well as water surface traffic monitoring (Krausman, 1994).

Under the "Joint Land Attack Cruise Missile Defense Elevated Netted Sensor (JLENS)" program, the US military in 2005 acquired a dozen set of radar aerostats to defend the forces against cruise ballistic missile, and also for tracking ground targets and tactical ballistic missiles in their boost phase. The JLENS aerostats used TCOM 71M aerostats, with 71 m long aerostats carrying a Raytheon payload with surveillance and targeting radars. The US Army also deployed a few "Rapid Deployment Initial Development (RAID)" systems to Afghanistan. The system uses 15 m long aerostats, with a sensor payload of 90 kg. Another system is the "Rapidly Elevated Aerostat Platform (REAP)" system which was used by the US Army in 2003 in Iraq with aerostats of only 9.5 m long and with a sensor payload weighing 16 kg. The entire system is capable of being deployed by a Hummer light truck. The US Army later on in 2006 deployed a "Persistent Threat Detection System (PTDS)" to Iraq. It uses mid-sized Lockheed Martin 56K aerostats, with a length of 33.4 m and a sensor payload of 225 kg (Krausman, 1994).

Tethered aerostats are not only limited to US army applications, but also to the US marines. They have deployed their own aerostat system, the "Marine Airborne Re-Transmission System (MARTS)" to Iraq, intended for radio relay. It uses TCOM 32M aerostats, with a length of 32 m and a relay payload weighing 225 kg.

In China, the People’s Liberation Army of China has a few tethered aerostat systems used for surveillance purposes. It was reported that China uses Au-21 Puma aerostats with NIIS/Leninets Novella/Sea Dragon radars from the Russia RosAeroSystems. This aerostat carries 2250 kg of payload and it is used to monitor the Straits of Taiwan where it could remain in the air for 25 days for up to 16,400 feet from ground (Krausman, 1994).

It is reported that the Israeli Defence Forces uses a few tethered aerostat systems. One of the systems was Homeland Security Aerostat for Border Protection, which used the EL/I-3330 radar with movement-detection facility and a day/night electro-optical sensor, and was manufactured by an Israeli company, Elta System (Krausman, 1994).

There are many other countries besides the above mentioned that have been well known to apply aerostat technology. Table 1 provides the types of aerostats which have been successfully deployed worldwide.

In this paper, the applications of these lighter-than-air (LTA) vehicles and the design aspect of tethered aerostat systems are reviewed and presented. This paper also presents the results of an initial sizing process conducted as part of a preliminary work related to the development of a tethered aerostat system conducted by the Science & Technology Research Institute for Defence (STRIDE).

Table 1: Current type of aerostat system used around the world (Source: Muthson, 2008)

Aerostat	L (m)	D (m)	Finess Ratio	Volume (m^3)	Payload (kg)	Payload Type	Alt (ft)	E (days)	Operation Wind Speed (kt)
15M(RAID)	15	6.2	2.42	290	90	Mini Radar	1000	7	40
32M(MARTS)	32	10	3.20	1800	225	Comm. Relay	3000	15	50
71M(TARS,JLENS)	71	22	3.23	16700	2300	Radar	15000	30	70
REAP	9.3	-	-	74	16	EO-IR	300	10	21
56K(PTDS)	33.4	11.1	3.01	1600	225	EO-IR	2500	-	-
275K(TARS)	57	19	3.00	7800	450	Radar	12000	10	-
420K(TARS)	63.5	21.2	3.00	12000	900	Radar	15000	30	-
Puma(Au-21)	60.7	21	2.89	8600	2250	Radar	15000	25	-
Aeros 21M	20.7	6.7	3.09	850	250	-	2500	-	-
Aeros 1170	25	10.5	2.38	-	91	EO-FLIR	4000	8	-
Aeros Sea Dragon	28	8	3.50	850	250	Comm. Relay	2500	-	-

2. AEROSTAT SURVEY

2.1 Finess Ratio

From the aerostat technical data in Table 1, comparisons are made between the finess ratio (i.e. length to diameter ratio) of the aerostat's envelope currently being deployed, as shown in Figure 1.

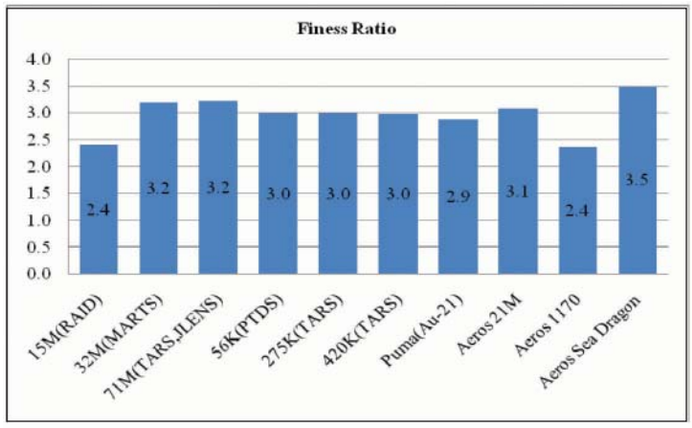

Figure 1: Finess ratio of aerostat envelope.

The data from Figure 1 shows that the finess ratio of the aerostat is between 2.4 and 3.5, and this information provides a guideline for designing the aerostat envelope.

2.2 Envelope Design

2.1.1 Envelop Structure

The structure of the envelope could be based on several main designs; rigid, non-rigid and semi-rigid. Rigid construction can be found on the Zeppelin craft of the 1920s and 1930s, which has an internal framework that maintains the shape of the envelope. Several ballonets containing lifting gas are located within the main envelope. Separate ballonets containing air are also housed in the envelope. The weight of the envelope, and hence the lifting force, can be controlled by pumping air in or out of the ballonets.

Non-rigid construction contains no internal framework to maintain the shape of the envelope. The shape is maintained by the pressure of the lifting gas within the envelope. For larger non-rigid types, they are normally included with a protective outer surface, made from robust material such as rubber. Smaller non-rigid types generally use a single skin of a durable material which has a low permeability to helium. The disadvantage of non-rigid type of designs is that components, such as radio equipment, cannot not be stored inside the envelope. However, this design proves to be simpler and less expensive compared to rigid envelopes.

Rigid structure significantly decreases the effective lift and increases the complexity and cost of manufacturing. Hence, for a smaller type of aerostat, the non-rigid design is more suitable to be used. It is inexpensive and has a high lift to weight efficiency.

Apart from the non-rigid and rigid design, the semi-rigid type suits the desired features of both characteristics. It has a non-rigid envelope with an internal pressure higher than that of the atmosphere to maintain its shape. It also has a framework, but this framework in not as extensive as the one found in the rigid design, and, hence the overall weight of the envelope is reduced.

2.2.2 Envelope Shape

Envelope shape for other projects was based principally on mathematical shape modelling and drag estimations. The National Physic Laboratory (NPL) of England made an approximate envelope using two ellipsoids, as shown in Figure 2.

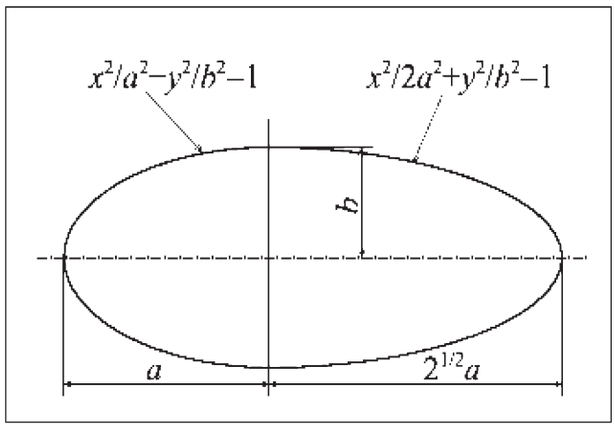

Figure 2: NPL low drag aerostat envelope (Source: Amool, 2005)

Another project initiated by Indian Institute of Technology Bombay, India, used the generalized shape as shown in Figure 3. The GNVR aerostat envelope shape is a combination of ellipse, circle and parabola.

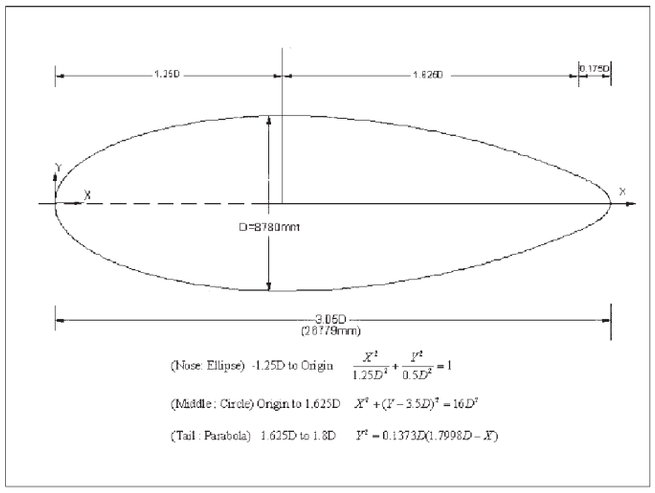

Figure 3: GNVR aerostat envelope (Source: Amool, 2005).

A family of aerostats manufactured by TCOM, USA as shown in Figure 4 uses a streamlined, elongated teardrop shape which has a larger frontal area compared to the GNVR shape and the NPL shape (Jones, 1985). This feature can be seen on many aerostat systems such as Lockheed 420K and RosAeroSystem Au-21.

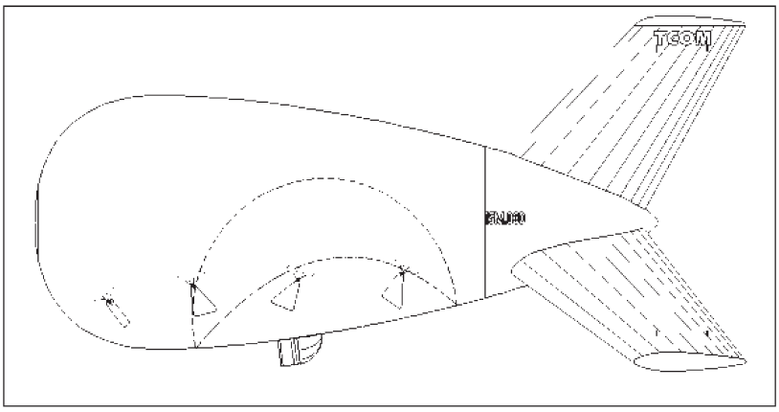

Figure 4: TCOM aerostat envelope
(Source: Jones, 1985).

2.2.3 **Envelope Material**

A number of material options are available for envelope manufacture to select. Factors such as cost, durability and permeation of helium have to be taken into account in deciding the material for aerostat envelope. There are several materials which can be used to manufacture a non-rigid envelope, including

polyurethane, “ripstop nylon” and polyvinylchloride. Polyvinylchloride or PVC is often used in the manufacturing of low budget tethered aerostats. The material is quite heavy and has high helium permeability compared to polyurethane or nylon. Hence, a larger envelope would be required to achieve the same amount of useable lift. A PVC envelope is manufactured using a gluing process to join sections of the hull. The joints also allow significant helium leakage from the envelope.

A “ripstop nylon” envelope consists of an internal bladder and an outer protective skin, which protects the bladder. Although the dual skins make the envelope heavier, but it has the advantage of robust application. “Ripstop nylon” is also commonly used in larger aerostats.

Polyurethane is a durable material, with good resistance to corrosion and low permeability. Polyurethane hulls are joined using plastic welding, making the seams have a comparatively low leakage. Although polyurethane is a more expensive envelope material, but it is commonly used for larger scale tethered aerostat.

2.2.4 Aerostat Fin

Fins are required for the stability of the aerostat. However, they also constitute a major portion of the weight, and also add to the drag. Based on the survey on the currently fielded tethered aerostat systems, most of the systems use inverted-Y shaped fins. An inverted-Y configuration is used to ensure rain and snow falling on the fins will not accumulate on the fins, thus avoiding disturbances to the balance of the aerostat (Schmidt, 1997).

2.3 Envelope Fabrication

The conventional method in fabricating aerostat envelopes is to make them from identical longitudinal petals, stretching from nose to tail. The number of petals depends on the availability of the material width. The petals will be joined together using either butt or lap joints. The lap joint is a simpler design, but has restriction in which the material must be structurally bondable on both sides. Once the type of seam is identified, there are several joining techniques to be considered in constructing the envelope. Joining techniques such as ultrasonic welding, RF welding, thermal welding, mechanical bonding and adhesive bonding can be used to join these petals together.

3. ENVELOPE DESIGN AND SIZING

A methodology for initial sizing and conceptual design of an aerostat system has been developed to obtain the required geometrical parameters and detailed mass breakup of an aerostat system, by considering some operation, configuration, and performance related parameters.

This methodology make uses of the MS-EXCEL™ spreadsheet and the module named as PROPESA. PROPESA accepts all the input parameters, constant parameters, and some geometrical and operation related options such as envelope profile selection and type of LTA gas used.

PROPESA provides the selection of optional parameters which makes the initial sizing more flexible and adaptive for any future modifications in the aerostat system, and makes sensitivity analyses much more comprehensive. In an aerostat, the geometry of the envelope has a profound effect on its aerodynamic characteristics, and hence on the stability and payload carrying ability. Some standard shapes of the aerostat envelopes exist and their profiles were incorporated into the input part of the PROPESA module.

3.1 PROPESA Modules

PROPESA is designed in a modular fashion and contains several spreadsheets that cover the calculations related to LTA gas properties in the atmosphere, and sizing of envelope, petal, tether and fins. The design procedure is based on the flow chart shown in Figure 5.

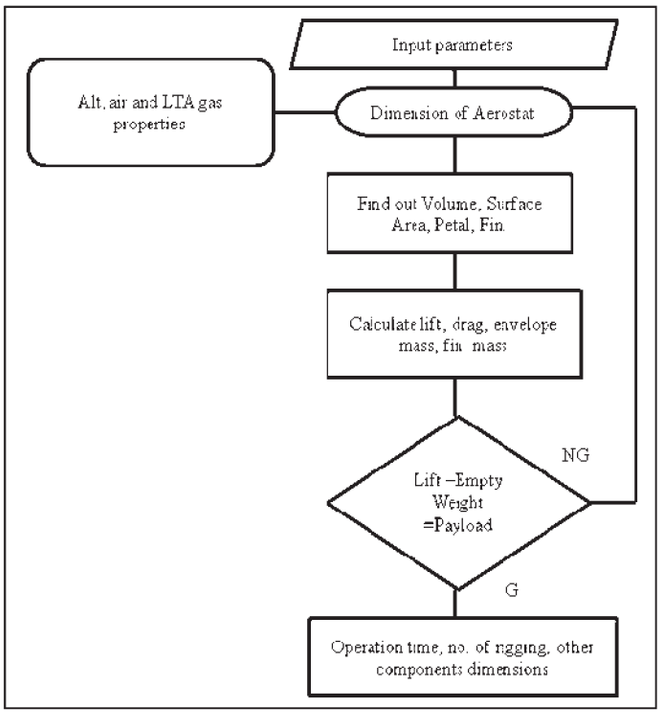

Figure 5: Design and sizing flow chart.

PROPESA starts by inputting all the required input data as shown in Table 2. A starting value for the envelope dimension is specified which invokes the envelope sizing module to calculate the volume and surface area of selected profile with the inputted dimension of the envelope. A detailed layout of the envelope profile, reference fin geometry and single gore petal is collectively shown in Figure 6.

Table 2: Sample input of the PROPESA module.

Input Parameters	SI Unit	Typical Value
Payload	[kg]	20
Floating Altitude (From Sea Level)	[m]	304.8
Spot Altitude (From Sea Level)	[m]	50
Design Wind Speed	[m/s]	15
Permissible Reduction in Altitude	±DH	5
Constant Parameters		
Contained Gas Initial Purity	[%]	99.5
Rate of Gas Permeability through Envelope fabric	[l/m^2/day]	2.5
Tether Cable Specific Length	[kg/m]	0.12
Available Envelope Fabric Density	[kg/m^2]	0.12
Permissible Blow by and Excess Length for all the cables Design altitude AGL	%	20
Options		
Profile Configuration (NPL-1, GNVR-2, TCOM-3)	NPL	1
Rear Gore Petals	[-]	16
Front Gore Petals	[-]	16
Contained Gas (He-1, H_2-2)	Helium	1

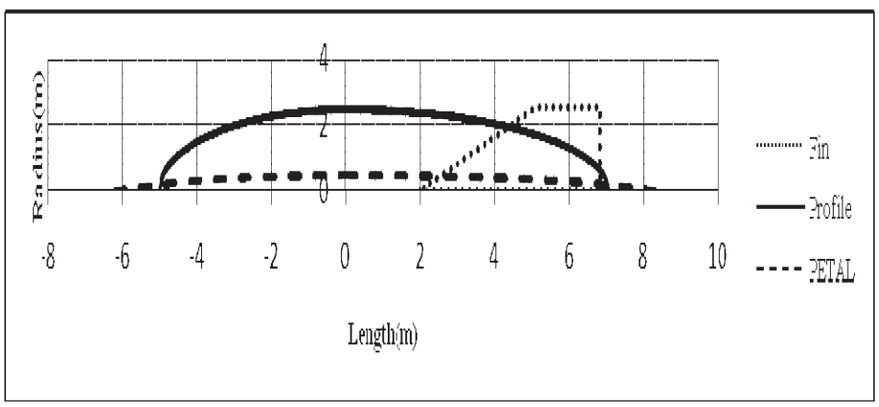

Figure 6: PROPESA output for envelope profile, petal and fin geometry.

The PROPESA receives the required properties of air and LTA gas and calculates the net disposable lift with volume of envelope, purity of LTA gas, volumetric drag and drag on the envelope by using the following equations (Amool, 2005).

$$Lift_{net} = V_e \bullet \left[\rho_{air} - \left(\rho_{LTA} - \left(\frac{Pu_{LTA}}{100} \right) \right) + \left(1 - \left(\frac{Pu_{LTA}}{100} \right) \right) - \rho_{air} \right] \quad (1)$$

$$C_{DV} = \left[0.712 \bullet {}^{l}\!/\!_{d}^{\,1/3} + 0.252 \bullet {}^{d}\!/\!_{l}^{\,1/2} + 1.032 \bullet {}^{d}\!/\!_{l}^{\,2.7} \right] \bullet \mathrm{Re}^{-1/6} \quad (2)$$

$$D = \rho_{air}^{a} \bullet v^2 \bullet V^{2/3} \bullet C_{DV} \quad (3)$$

3.2 Weight Estimation

From the calculation in PROPESA, mass of various group of aerostat as the Table 3.

Table 3: Weight estimation as obtained from PROPESA.

Group	Criteria	W(kg)
LTA Gas	-	26.71
Envelope sub-group	-	
Envelope	$W_e = \rho_{fabric} * S_e$	19.51
Riggings, Hook + Patches	$0.06 * W_e$	1.17
Nose battens	$0.1 * W_e$	1.95
Gas filling hose/opening/port	$0.02 * W_e$	0.39
Fin subgroup	-	
Mass of PU cover	Fin Module*	4.11
Mass of fin structure	Fin Module*	1.20
Total fin mass	Fin Module*	5.31
Total empennage	$3 * W_{Fin}$	15.92
Tether sub-group	-	
Tether cable	$l_t * \rho_t$	43.89
Pivot + payload frame	Fixed	4.50
Confluence line support distribution wire	$0.01 * We$	0.20
Payload	DR&O	20.00
Total Weight(kg)		144.84
Nett Lift(kg)		168.00
Lift Margin(kg)		23.16
% Lift Margin		13.79

The above weight estimation is based on an NPL shaped aerostat which is 12 m in length and 5 m in diameter.

4. FUTURE WORKS

4.1 Envelope Fabrication

The fabrication of the aerostat should be simple and easy to maintain. Therefore, this project will adopt the conventional method in developing the aerostat envelope. The design shall be from 16 identical longitudinal petals, stretching from nose to tail as shown in Figure 7. The layout of each petals of the envelope will be printed on a vinyl banner that will be the main master petal template. This template will comprise of markings for all external attachments–i.e. hooks for nose rings, nose batten, guy ropes, riggings and finger patches for confluence lines. The envelope material will be cut into 16 petals based on the master petals. These petals shall then be joined together using lap joints by means of an RF welding machine.

Figure 7: Identical petal layout for envelope shape.

4.2 Flight Test

Flight testing of the tethered aerostat will be conducted in order to obtain the aerodynamic and stability characteristics (Lambert, 2003). The data that will be collected during the flight testing are from measurements and will be stored during normal flight operations. These data items include the tether length, wind speed, tension of the tether at the aerostat, its pitch and roll angles, and altitude. The onboard sensor will be used to measure pitch and roll during flights. The load cell will be used to measure tether tension at the confluence point of the aerostat's flying lines.

5. SUMMARY

Tethered aerostats are used for a variety of military and civil applications around the world. Its capability to perform long duration surveillance at fixed locations with minimal costs has been the major reason of choosing this type of air platform. Hence, a research project was initiated in STRIDE to develop a non-rigid type of aerostat system for military surveillance purposes. The fabrication process will be done in-house in STRIDE and flight testing will be held to evaluate its performance.

ACKNOWLEDGEMENTS

The authors would like to thank the following STRIDE personnel for their involvement in the project; Ahmad Subardi Mohd Wazir and Jeffrey Hassan.

REFERENCES

Amool A.R (2005). Design, fabrication and field testing of an aerostat system. *J. Aircr.*, **42**: 1-23.

Lambert, C. (2003). Stability analysis of a tethered aerostat. *J. Aircr.*, **40**: 1-11.

Schmidt, G.S. (1997). Results of the 420K tethered aerostat flight tests. *Proceedings of AIAA 12th Lighter-Than-Air Systems Technology Conference*, June 1997, USA.

Krausman, J.A. (1994). Airship and tethered aerostat operations and optimization. *Proceedings of AIAA 9th Lighter-Than-Air Systems Technology Conference*, June 1994, USA.

Muthson, K. (2008). Jane's All the World Aircraft. Jane's Information Services, pp 50-60.

RECOGNITION OF GUNSHOTS USING ARTIFICIAL NEURAL NETWORK

Mohd Faudzi bin Muhammad[1] & Marzuki bin Mustafa[2]

[1]Instrumentation and Electronic Technology Division
STRIDE, Ministry of Defence, Malaysia
Tel: 603-87324438
Fax: 603-87348695

[2]Department of Electrical, Electronic and Systems Engineering
Faculty of Engineering
Universiti Kebangsaan Malaysia
43600 UKM Bangi, Selangor

[*]Email: mpuji70@yahoo.com

ABSTRACT

In this paper, a system for automatically identifying guns by their sounds is implemented. The gunshots data are recorded from 3 different types of guns; 155 mm, 105 mm and 90 mm. Power Spectral Densities (PSD) are used to extract the gunshot sound's spectral information. These feature parameters then serve as the input to the artificial neural network (ANN). A three layer feed forward neural network is used with back propagation as the training algorithm. The network size was selected to be 33-8-8-3 (33 input, 8 1st hidden layer, 8 2nd hidden layer and 3 output unit). Sample populations of 75 data are used as training data and 75 data serve as testing data. The results show that the trained network can correctly identify gunshot sounds with up to 90% accuracy.
Keywords: *Gunshots, Power Spectrum Densities, Artificial Neural Network (ANN).*

1. INTRODUCTION

A gunshot sound, like all sounds, has definite characteristics that can be used to verify its uniqueness when compared to other sounds (Dufaux et al., 2000). Gunshot recognition systems can be used for surveillance and security applications. It is crucial for the Malaysian Armed Forces (MAF) to identify the types of guns that are employed by the enemy, especially for short and long range guns. This information will facilitate the field commander to launch counter attacks against the enemy position. Hence, this paper is aimed at developing a system for automatically identifying guns by their sounds.

2. COLLECTING GUNSHOT SAMPLES

In order to build a system that can be used for classification, a number of samples have to be collected first. All of the signals were recorded using a tape recorder and then digitised (MathWorks, 2006). The data used in the experiments contained 150 sounds of three different types of guns; 50 for 155 mm, 50 for 105 mm and 50 for 90 mm. All the samples were split into two groups; the training set (about 50% of cases) and the test set (about 50%). The sampling rate was 10 kHz (each data contains 4096 samples), which is sufficiently high if we take into account that the frequencies of typical gunshots are below 1000 kHz.

3. PSD FEATURE EXTRACTION

Like human speech that has been thoroughly studied, gunshots characteristics consist of temporal and spectral qualities. Power Spectral Density (PSD) analysis has been used successfully in the past for human speech

recognition and it is also useful for analysis of gunshots. Spectral variables combined with temporal ones can form input vectors for recognition methods such as artificial neural network (ANN). In our approach, we tried various features that could be extracted from general characteristics of samples; Fast Fourier Transform (FFT), wavelet, Linear Predictive Coding (LPC) and PSD, and it was discovered that the application of PSD characteristics was sufficient for obtaining high quality classifications (Hiyane & Lio, 2001).

Figure 1 shows a typical gunshot sound spectrum for 155 mm. Its estimated PSD is shown in Figure 2. The 155 mm gunshot signal is filtered using a bandpass filter that allows the desired frequencies from 100 Hz to 350 Hz to pass. The results after the filtering are shown in Figures 3 and 4.

As shown in Figure 4, small sets of coefficients were selected from 100 Hz to 350 Hz. This means each data has about 100 coefficients for each matrix to serve as feature vectors. However, in gunshot classifications, the dimension of sample will be reduced using the framing method so that smaller number of the inputs will be applied to neural nets. Each frame contains a sum of three samples and the total number of the frame is 33.

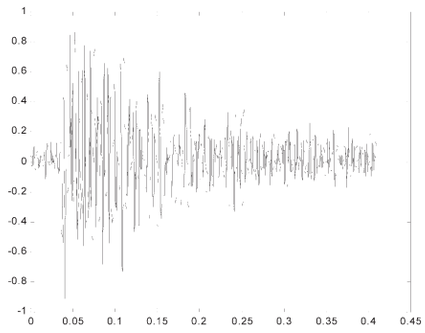

Figure 1: A typical 155 mm gunshot.

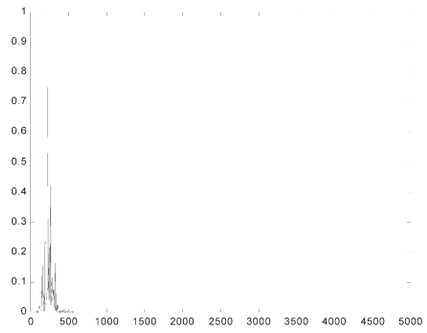

Figure 2: PSD for 155 mm gunshot.

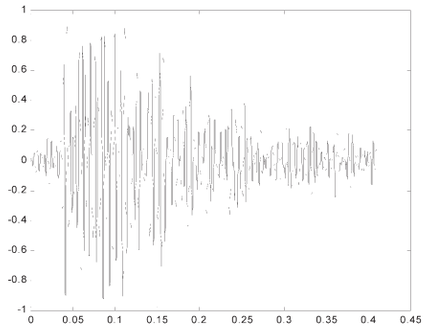

Figure 3: Waveform for 155 mm after filtering.

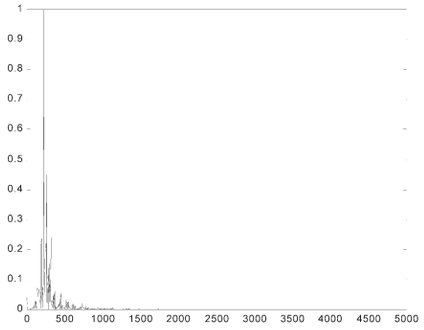

Figure 4: PSD after filtering.

4. ARCHITECTURE OF PROPOSED SYSTEM

The overall system architecture is shown in Figure 5. The digitized input signal is converted to its PSD profile (Smith, 1997). Then this profile is compared by ANN procedure to all reference profiles stored in the database. The type of the reference profile that is similar to the input profile determines the output.

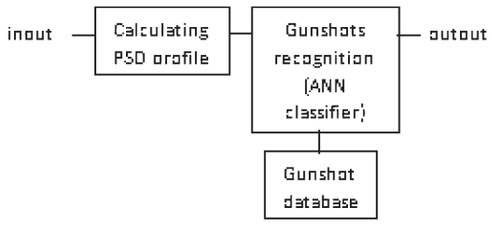

Figure 5: The overall architecture of the gunshot classifying system.

5. GUNSHOT IDENTIFICATION

For gunshot identification, the ANN algorithm was selected (Cawling, 2002). The ANN algorithm was implemented in MATLAB as a network with a set of inputs and an output of the correct class (MathWorks, 2008). The network contains a 3-layer feed forward; 33 input layers, 8 hidden layer 1, 8 hidden layer 2, and 3 outputs.

The output was a three digit binary number. For example, for the 155 mm gun, the output would be 100, 010 for the 105 mm gun, and 001 for the 90 mm gun. A back propagation neural network (BPN), as shown in Figure 6, was used in the training and recognition phases of the gunshot recognition system. A gradient descent with momentum and adaptive learning rate algorithm was used for the network training.

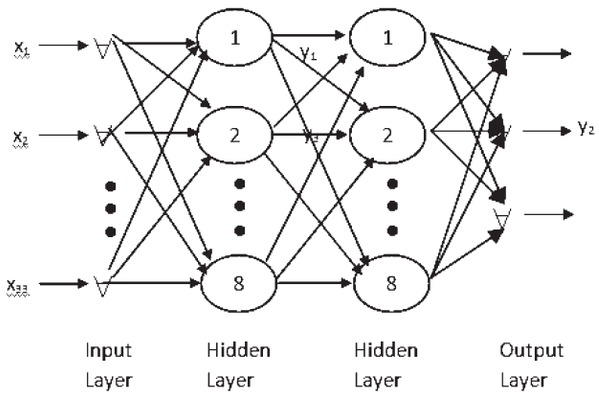

Figure 6: 3-layered BPN architecture.

6. RESULTS AND CONCLUSION

The neural network was tested with 33 input nodes, 8 hidden nodes for layer 1, 8 hidden nodes for layer 2 and 3 output nodes to transform the input PSD vector into the appropriate output pattern. The examples of neural network training results are shown in the Table 1 and the results of test data are listed in Table 2.

Table 1: Neural network training result.

Gun	System Output	Binary Equivalent
155 mm	0.9360 0.0461 0.1041	100
105 mm	0.1051 0.9008 0.1107	010
90 mm	0.0913 0.1076 0.8945	001

Table 2: Neural network test result.

Gun	System Output	Binary Equivalent
155 mm	0.8432 0.1033 0.0987	100
105 mm	0.0952 0.9241 0.0848	010
90 mm	0.0948 0.0879 0.9067	001

For 155 m, 105 m and 90 mm guns, it is observed that:

- For the 155 mm gun, 2 of 25 tested data wrongly classified
- For gun 105 mm, 1 of 25 tested data wrongly classified
- For gun 90 mm, 1 of 25 tested data wrongly classified.

From the results, it is observed that identification accuracy can reach up to 90%, and thus, we can conclude that the network is able to correctly recognize gunshot signals. This paper demonstrates the advantages of ANN in classifying gunshot sounds via their general PSD characteristics.

REFERENCES

Dufaux, A., Besacier, L., Ansorge,M. & Pellandini, F. (2000). Automatic sound detection and recognition for noisy environment. *Proceedings of EUSIPCO 2000, European Signal Processing Conference*, pp.1033-1036.

Hiyane, K, & Lio, J. 2001. Non-Speech Sound Recognition with Microphone Array. *International Workshop on Hands-Free Speech Communication*, pp. 107-110

Cawling, M. (2002). Analysis of speech recognition techniques for use in a non-speech sound recognition system. *6th International Symposium on DSP for Communication Systems*, Sydney-Manly, Australia

MathWorks (2006). MATLAB Signal Processing Toolbox. The Math Works Inc., Natick, Massachusetts.

MathWorks (2008). MATLAB Neural Network Toolbox. The Math Works Inc., Natick, Massachusetts.

Smith, S.W. (1997).The Scientist and Engineer's Guide to Digital Signal Processing. California Technical Publishing, California.

PRE-DEVELOPMENT OF READY TO EAT MEAT BARS FOR MALAYSIAN SUBMARINERS

Noorhasifah Ab. Aziz*[1], Mohd Shahrulnizam Mah Hassan, Salmah Muda, Razalee Sedek, Alina Abd. Rahim[2], Abang Omar Abang Ali[3]

[1]Protection & Biophysical Technology Division,
Science & Technology Research Institute for Defence (STRIDE),
Taman Bukit Mewah Fasa 9, 43000 Kajang, Selangor D.E.
Tel: 03-87324531
Fax: 03-87336219

[2]Faculty of Science & Technology, Islamic Universiti College of Malaysia (USIM), Nilai, Negeri Sembilan.
[3]Omcorp Sdn. Bhd, Kajang, Selangor.

*Email: cfah2001@yahoo.co.uk

Abstract

The proposal to develop a type of food product for submarine rations, known as meat bar, is based on meal ready to eat (MRE). There are two different types of meat bars that are being developed as part of this research which are made from beef and chicken products. There are three different flavours being developed to give taste to the chicken and beef meat bars, which are sate spice, honey and black pepper. The formulation of the meat bars is being modified and improved to become a tasty final product with optimum quality. To reach a goal of standard formulation, this research depends on the requirements, feedback and sensory evaluation of consumers. Based on preliminary results, two types of formulations are being developed to have a final product which is known as the prototype for meat bars. Besides developing standard formulations, this research is also aimed at choosing the best raw materials of meat between minced meat and fillet meat to be the main raw material to develop the final products. The method for cooking meat bars is also being improved by oven-grilling at 120 °C for 25 minutes (beef) or 20 minutes (chicken) using combination oven and pre-heated oven at 150 °C for 20 minutes (beef) or 15 minutes (chicken). The food chemical analysis (proximate analysis) was conducted to study the nutrient contents of the meat bars which include determining moisture (water), ash, fibre, fat and protein contents. At the moment, this test is currently only able to determine the moisture and ash content. However, other laboratory tests will be done later after the standard formulation to produce the prototype is finalized. From the results, it is shown that the moisture content is in the range of 57 to 69% and ash content is 2.9 to 5.4% in meat bar products. The results of the sensory evaluation shows that the first formulation's mean score for all attributes are in the low range of 2 to 6, which can be concluded as "dislike". For second formulation of meat bars, the mean score of sensory evaluation is higher than the first formulation (mean score ranged from 5 to 7).Hence, it can be concluded that the second formulation is acceptable and in average of "like" score.

Keywords: *Meat bar; meal ready to eat (MRE); submarine ration; oven-grilling; sensory evaluation.*

1. INTRODUCTION

Under the Ninth Malaysia Plan (RMK9), a research project to produce new submarine rations is being conducted to perpetuate the maintenance of good morale for troops who are working and living in often austere and underwater environment conditions. The concept of new submarine rations, known as meat bars, is based on ready to eat meals made from meat and chicken products that are produced using the retort pouch method. Since 1992, the Malaysian Armed Forces (MAF) personnel have taken their meals, which include dishes such as Chicken Masak Merah Pouch Halal, Beef Rendang Pouch, Chicken Curry Pouch and Beef Kurma, in plastic-foil

pouches during military operations (MAF, 1993). In 2009, the MAF will make use of the submarines KD Tunku Abdul Rahman and KD Tun Razak to conduct military surveillance operations. In order to maintain the good morale of troops who are working and living in often austere and underwater environment conditions, this new submarine ration was developed. The main objective of this research is to develop a ready to eat meal made from meat and chicken, and to introduce this new product in military ration scale, specifically for submariners and also for other military operations in flight and battle fields.

1.1 Meat Products and Meal Ready to Eat (MRE)

The meal ready to eat (MRE) is a totally self-contained, flexibly-packaged meal used by MAF personnel in the field. The MRE must be able to be maintained at high quality for three years at 27 °C and six months at 38 °C, be highly acceptable, and meet the nutritional requirements. In addition, MRE packaging must meet stringent durability requirements (including airdrops, rough handling and temperature extremes). MRE was developed for soldiers in combat conditions. These meals are already cooked and moist. Whenever disaster strikes, there is no time to look for, or cook, meals, and hence, long shelf life is always in high demand (Wikipedia, 2009).

Based on the meat and chicken products, the finished product was formed as kebab and sate. Kebab (also transliterated as kabab, kabob, kibob, kebhav and kephav) refers to a variety of meat dishes in Middle Eastern, Mediterranean, African, Central Asian and South Asian cuisines, consisting of grilled or broiled meats on a skewer or stick. The most common kebabs include lamb and beef, although others use goat, chicken, fish or shellfish. Observant Muslims and Jews do not use pork for kebabs because of religious and cultural prohibition, but pork kebabs can be found in India, especially in the state of Goa. Like other ethnic foods brought by immigrants and travellers, the kebab has become part of everyday cuisine in multicultural countries such as the UK, Australia, New Zealand and the United States.

In this study, whole meat is cut into steak form while minced meat is reformed and moulded into 80 gram bars. A steak (from Old Norse *steik*, "roast") is a slice of meat, typically beef. Most steaks are cut perpendicular to the muscle fibres, improving the perceived tenderness of the meat. In North America, steaks are typically served grilled, though they are also often pan-fried. Because steaks are cooked quickly, using dry heat, and served whole, the tenderest cuts of the animal are usually used for steak. This also means that steaks have a premium price and perception; the idea of eating steak is a signifier of relative wealth. For Malaysians, steak is regarded as one of the quintessential dishes of Western cuisine.

There are many types of beef cuts such as chuck, rib, short loin, brisket, plate, flank, round, sirloin and shank. In this research, the sirloin part, which is a steak cut from the hip, which tends to be less tough, was used. For the chicken product, boneless chicken breast and legs were used to produce the bar.

The tenderness, juiciness, flavour and colour of meat products are the main eating quality characteristics that influence the consumers' overall judgement of quality (Barbanti & Pasquini, 2005). Hence, in this research, minced beef meat and minced chicken are also used as raw materials for comparison in order to choose the most suitable raw material that should be used to produce tasteful meat bars.

1.2 Ingredients, Marination and Grill Cooking Method

In this research, marination is a process to produce meat bars. Marination is a traditional culinary technique that is used to tenderize and improve the flavour and juiciness of poultry meats (Lemos *et al.*,1999). According to Barbanti & Pasquini (2005), the process of marination, followed by air-steam cooking, is the best combination to obtain the tenderest chicken breast. In order to marinate the meat, sugar, salt, phosphate and other natural ingredients are used. Sodium chloride, polyphosphates and sugars are considered important ingredients of marinades as they improve meat tenderness and flavour. Marination also increases the water binding capacity of meats, thus reducing cooking losses and improving meat juiciness (Froning & Sackett, 1985). The cooking method that is used in this research is the oven-grilled method. Grilling, also known as direct grilling, is cooking with direct heat at a high temperature. The heat source can be below or above the food being cooked. Direct

grilling can be done over high, medium or low heat. In this research, two types of ovens are used for the grilling method. The first type of cooking is using a pre-heated oven and the second type of cooking is using a combination oven with selected meat grilling in air steamed condition with 100% humidity. From the previous study of Sheard *et al.* (1998), two cooking methods were used for each product type, based on those recommended by the manufacturer. Burgers and sausages were grilled and fried, restructured steaks were grilled and oven cooked, while minced beef was cooked by boiling or a combination of frying followed by boiling. According to Murphy & Marks (2000), the key eating quality characteristics of meats (for example cooking loss, tenderness and crust formation) are mainly affected by both cooking technique and time-temperature profiles.

1.3 Retort Pouch Technology for Meat Products

The finished product will be packed in a pouch plastic by using the retorting method. The retorting step is important as a sterilization process to prolong the shelf life of the product and to avoid bacterial contamination. Retort systems use steam or superheated water to cook food in its own package, extending shelf life and ensuring food safety. Retort flexible packaging is not new. In fact, it has been around since the late 1960s when the US Army began looking to replace its unpopular canned C-rations. That project led directly to Meal Ready to Eat (MRE) packaging, which the Army uses to this day. Since then, retort packaging has evolved from a mostly aluminium foil structure to a sophisticated multilayer, high barrier laminated package. This is done because food packed in the retort pouch tastes much better than canned rations.

Under U.S Unitized Group Ration (UGR), the concept of integrating heat and serve is applied for their menus such as hamburgers, beef and green peppers, bacon and cheese and others (DOD, 2006). In addition, one of the MREs for the Australian Defence Force is chicken sate. They used retort pouch packaging for chicken sate meal. In the Singapore food industry, they also have chicken sate in the ready meal at their food market. In conclusion, the idea to develop meat bar products for the MAF is relevant for the time being.

2. RESEARCH METHODOLOGY

2.1 Research Frameworks

The research framework for the development of the meat bar is shown in the Figure 1:

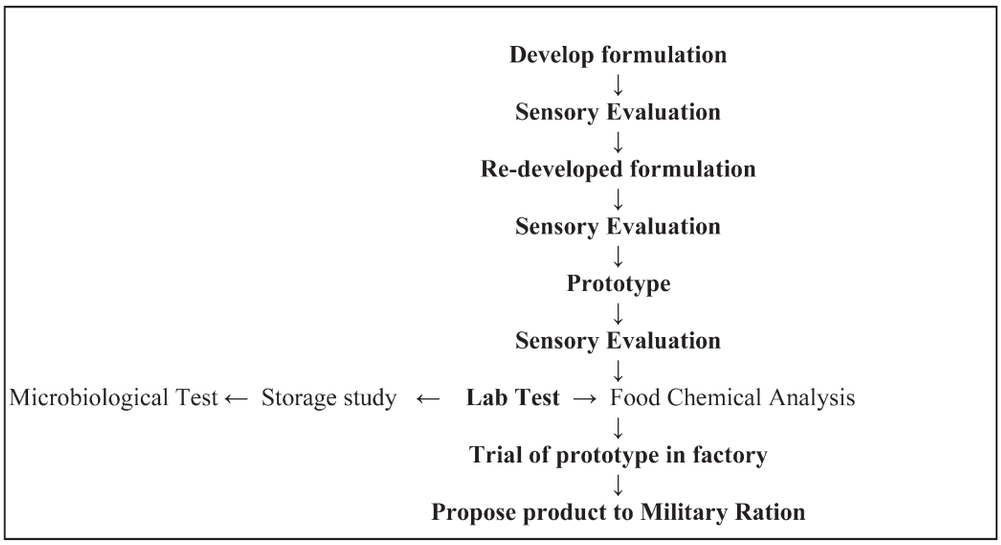

Figure 1: Research framework for the development of the meat bar.

2.2 The Ingredients and Flavours of Meat Bar

The concept for new submarine rations, known as meat bar, is based on ready to eat meals. There are two different types of meat bars that were developed during this research which are made from beef and chicken products. In this research, two different types of meats were used to produce beef and chicken bars, which are fillet and minced meat. The objective of using different types of meat is to determine and study which type of meat is most acceptable, convenient, tasty and preferred by consumers, especially for the Malaysian submariners. Tenderloin (beef from India) and breast part (local chicken) are used as fillet meat. In addition, minced beef from Australia and local fillet chicken (manual mincing) are used as minced meat. Raw materials are bought from the Omcorp Sdn. Bhd meat factory, the nearest hypermarket (Carrefour Alamanda, Putrajaya) and Pasar Borong Selangor.

There are three different flavours being developed to give taste to the chicken and beef meat bars, which are sate spice, honey and black pepper. Lean beef meat and boneless chicken are used in the production of the meat bars. Other ingredients used are black pepper, white pepper, sugar, salt, honey, turmeric powder, garlic, ginger, lemon grass, fried onion, phosphate and tenderizer, depending on the type of product's flavour.

2.3 Process of Developing Meat Bar

After mixing the raw products with the ingredients (Figure 2 (a) & 2 (b)), it will then be marinated for 24 hours at 0 – 4°C (Figure 3 (a) & 3 (b)). After 24 hours marination, the marinade is reformed to 80 gram bars (for minced meat) (Figure 4). The grilling method is used to cook the marinated raw meat. The marinades are grilled at 120°C for 25 minutes (beef) or 20 minutes (chicken) using combination oven and pre-heated oven at 150°C for 20 minutes (beef) or 15 minutes (chicken) (Figure 5). The ready to eat meat bars are shown in Figure 6. Finally, the finished product will be sterile packed using retort pouch sterilization. The formulation of meat bars is in progress of modification and upgrading to become a tasty final product with optimum quality. To get a goal for standard of formulation, this research depends on the requirements, feedback and sensory evaluation of consumers. This final product is known as the prototype.

(a) **(b)**

Figure 2: Raw products: (a) beef meat and chicken, (b) beet meat and other ingredients.

(a)

(b)

Figure 3: (a) Marinated chicken fillet; (b) Storage of marinade, 24 hours at 0 – 4°C.

Figure 4: Process of reform into meat bars.

Figure 5: Cooking process (oven grilled).

2.4 Sensory Evaluation Test

The Hedonic Scale method was used to determine the level of acceptance for different products of meat bars and to provide a benchmark on which to compare results (Stone and Sidel, 1993). In this research, 15-20 trained panels from STRIDE volunteered to evaluate the meat bar products (Figure 7). To date, two sessions of sensory evaluation have been done on two different formulations. Nine scales, ranging from totally dislike to totally like, are used to evaluate four attributes including, colour, odour/aroma, taste, texture and total acceptability. Suggestions and comments from the panels are also evaluated.

Figure 6: Ready to eat meat bars prepared for sensory analysis.

Figure 7: STRIDE trained sensory panels during the sensory evaluation sessions.

2.5 Laboratory Analysis

Samples are weighed before and after cooking. Cooked products are allowed to cool for 30 minutes before weighing, when their internal temperatures are in the range 20°C to 35°C. Cooking losses are calculated from measurements of initial and final weight. All samples for analysis are comminuted and grounded using blender & mixer to homogenize it for proximate analysis. Proximate analysis is performed in triplicate following AOAC procedures (AOAC, 1995). The total water content is determined by oven drying method at 110°C for 24 hours. The total protein content is determined by using the Kjeldhal method (AOAC, 1995). The total fat is analysed using the Soxhlet method (AOAC, 1995) and total ash content is determined by weight after heating samples in a muffle furnace at 550°C for 4 hours (AOAC, 1995). The energy value of cooked product is analysed using a bomb calorimeter for comparison with the energy value from calculation method.

3. RESULTS AND DISCUSSION

3.1 Weight Loss of Cooked Meat Bar

To calculate the percentage of weight loss, weight gain before cooking is recorded. After cooking and cooling for 30 minutes, the weight loss is recorded. From the data, percentage of cooking loss due to water evaporation of the cooked meat bar is calculated. Losses of fat and moisture due to cooking are shown in Table 1.

Table 1: Percentage of weight loss after cooking meat bar.

Samples		Weight (g)			% of Weight Loss
		Before Cooking	After Cooking	Weight Loss	
Beef	Minced Blackpepper	519.6	369.1	150.5	29.0
	Minced Honey	532.6	378.0	154.6	29.0
	Minced Sate Spice	549.6	369.1	180.5	32.8
	Fillet Blackpepper	521.7	304.7	217.0	41.6
	Fillet Honey	529.8	289.8	240.0	45.3
	Fillet Sate Spice	547.0	315.7	213.3	42.3
Chicken	Minced Blackpepper	532.5	429.9	102.6	19.3
	Minced Honey	531.6	428.3	103.3	19.4
	Minced Sate Spice	558.4	411.7	146.7	26.3
	Fillet Blackpepper	522.2	417.1	105.1	20.1
	Fillet Honey	521.0	401.8	119.2	22.9
	Fillet Sate Spice	546.1	407.5	138.6	25.4

According to Froning & Sackett (1985), the synergistic effect of salt and phosphates on meat decreases cooking losses, improves texture and enhances water-holding capacity. From the results in Table 1, the weight loss is quite high (19 to 25%) for cooked chicken meat and 29 to 45% for cooked beef meat. This is may be due to the effect of the marinating process and cooking temperature, and most likely due to the minimal amount of polyphosphates in our formulation ingredients. Based from the of Barbanti & Pasquini (2005), the differences due to the cooking method using air steam method increased the cooking loss at 130, 150 and 170ºC, for 8 and 12 minutes for marinated chicken fillet samples, ranging from 29 to 45% of cooking loss.

3.2 Proximate Composition of Meat Bar

The research is continued by conducting food analyses, such as microbiology test, storage studies and chemical analysis. The preliminary results are only at the stage of improving the formulation, sensory analysis and proximate analysis. The proximate analyses are conducted to determine the nutritional values of product in terms of fat, protein, ash and moisture content. It shall contain not less 1.7% of nitrogen in organic combination and shall not contain more than 30% of fat content in this product (maximum amount stipulated in the Food Regulation 1985). From Siong et al. (1997), the nutrient composition was referred in the beef burger patty category which contains 187 Kcal of energy, 40 g (53.8%) of water, 16.7 g (22.5%) of protein, 11.7 g (15.8%) of fat, 3.6 g (4.9%) of carbohydrate, 2.2 g (3%) of ash and no fibre content in a 74 g sample. For chicken burger patty category, it contains 157 Kcal of energy, 45.9 g (60.4%) of water, 13.7 g (18%) of protein, 8.8 g (11.6%) of fat, 5.8 g (7.6%) of carbohydrate, 2.0 g (2.6%) of ash and no fibre content in a 76 g sample.

The results of moisture and ash content for 12 types of meat bars is shown in Table 2.The results shows that the percentage of moisture is quite high; 57 to 61% for cooked beef meat and 62 to 69% for cooked chicken meat. From the Siong et al. (1997), the moisture content of meat products, especially for beef burger patty, should be 53.8%, and 60.4% for chicken burger patty, of its total weight. It indicates that the cooked meat bar has higher moisture content compared to the beef burger patty. For ash content, this study shows that the range of ash content in the meat bar is 2.9 to 5.4%. It indicates that some of products contain ash higher than beef burger patty (3%) according to the literature. At the moment, this test currently is only able to determine the moisture and ash content. However, other tests will be conducted later after the standard formulation to produce the prototype is finalized.

Table 2: Moisture and ash content of the meat bars.

Samples	Ash (%)	Moisture (%)
Beef Fillet Honey	4.07	60.01
Beef Fillet Black Pepper	4.19	60.78
Beef Fillet Sate Spice	2.89	62.60
Beef Minced Honey	3.11	57.79
Beef Minced Black Pepper	2.90	57.80
Beef Minced Sate Spice	3.22	57.06
Chicken Fillet Honey	3.83	62.23
Chicken Fillet Black Pepper	5.36	64.40
Chicken Fillet Sate Spice	3.45	64.75
Chicken Minced Honey	3.34	66.77
Chicken Minced Black Pepper	3.27	68.86
Chicken Minced Sate Spice	2.68	68.33

3.3 Product of Ready to Eat Meat Bars

Based on the two formulations that have been developed, Figures 8-11 show the uncooked and cooked meat and chicken bars respectively. To date, this research is in the process of procuring a standard mould in bar shapes to fulfil the meat bar standards. However, for ongoing research progress, standard burger 80 grams mould is used to mould the minced meat. For the fillet of meat and chicken, the shapes and size of marinade is controlled by weigh not exceeding 100 grams per fillet.

Figure 8:
Minced beef meat bar before cooking.

Figure 9:
Minced chicken meat bar after cooking.

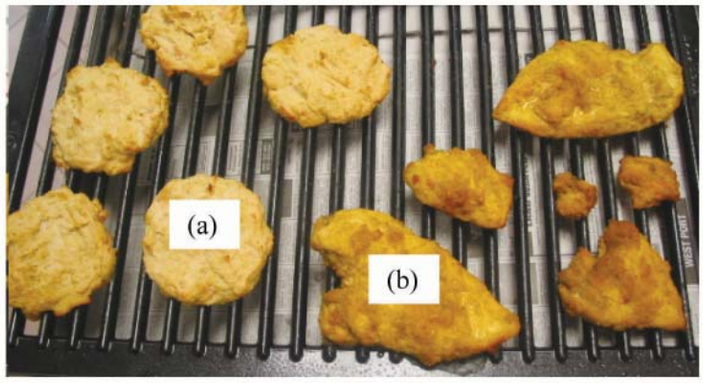

Figure 10: Cooked (a) minced chicken (b) chicken fillet

(a) **(b)**

Figure 11: Minced beef meat bar (a) before cooking; (b) after cooking

3.3 Results of Sensory Evaluations

There are 12 finished products that were produced according to the types of meat and its flavours such as honey, black pepper and sate spice. A sensory evaluation was conducted to determine the taste, colour, aroma, texture and overall acceptance of all the products of meat bar by the consumers. This test was also aimed at determining which product is most acceptable, tasty and fulfils the consumers' need. Besides that, some of products should be improved in terms of their taste, texture, aroma and colour according to the perceptions from panellists. There are 12 panellists from STRIDE involved in this test.

In this sensory evaluation, the Hedonic Scale method was used to determine the level of acceptance for different products of meat bars and to provide a benchmark on which to compare results (Stone and Sidel, 1993). The results in Table 3 show the comparisons of two sessions of sensory evaluations for the two formulations of meat bars. For the first formulation, it shows that the mean score for all attributes are in the low range of 2 to 6 which can be concluded as "dislike". After we formulated second formulation of meat bars, the mean score of sensory evaluation is higher than the first formulation (mean score ranged from 5 to 7). We can conclude that the second formulation is acceptable and in average of the "like" score. From the results, it is shown that chicken minced sate spice received the lowest overall liking scores compared to the other products. The highest liking score is 7.0 ± 1.2 for overall acceptance for chicken fillet sate spice may be the result of the consumers' greater experience with chicken fillet sate spice.

4. CONCLUSIONS

In this research, we used chicken and beef as raw materials. From the materials, we tried to evaluate the best raw materials (minced or fillet) to produce a tasty meat bar. To date, only two formulations have been developed using the technique of marinating before the grilling process. The first type of cooking is using a pre-heated oven and the second type of cooking uses a combination oven with the selection of meat grilling in air steamed condition with 100% humidity. The results of the sensory evaluations show that, the mean score for all attributes of first formulation are very low ranged from 2 to 6 which can be concluded as "dislike". After we formulated second formulation of meat bars, the mean score of sensory evaluation is higher than the first formulation (mean score ranged from 5 to 7). We can conclude that the second formulation is acceptable and in average of the "like" score. From the results, it is shown that chicken minced sate spice received the lowest overall liking scores compared to the other products. The highest liking product for chicken fillet sate spice may be the result of the consumer's greater experience with chicken fillet sate spice. For the next research progress, the third formulation for meat bars will be developed and will be continue to be evaluated with sensory evaluation sessions and other laboratory analyses. As a conclusion, the formulation of meat bars will be improved to produce a high quality product which meets the requirements of consumers and will give a better taste. Hopefully this research will develop a prototype for meat bars and will be introduced in the submarine ration menu for use during surveillance operations.

ACKNOWLEDGEMENT

We gratefully acknowledge the STRIDE Nutrition and Ration Branch personnel, En. Mohd Badrolnizam Jamhari, En. Abdul Jalani Hj Aini, Pn. Seti Salmah Khalid and Pn. Nadira Mahadi, for their supportive effort during laboratory analysis and product development. Lots of gratitude also to Islamic University College of Malaysia (USIM) for their technical consultations. We are also grateful to Omcorp Sdn. Bhd. for their kindness in allowing use to their factory facilities, and in procuring product materials.

Table 3: Mean scores of sensory evaluation on two formulations of meat bar.

Samples/ Score (Min ± s.d)	Colour		Aroma		Taste		Texture		Overall Acceptance	
	F 1	F 2	F 1	F 2	F 1	F 2	F 1	F 2	F 1	F 2
Beef Fillet Honey	5.8±1.4	6.3 ± 1.1	5.3±1.4	6.3 ±1.1	6±1.71	6.3 ± 1.3	5.2±1.9	6.3 ± 1.1	5.3±2.1	6.3 ± 1.3
Beef Fillet Black Pepper	5.9±1.8	7.0 ± 1.0	5.4±1.7	7.0 ±1.0	5.8±1.7	6.8 ± 1.5	5.3±2.0	6.7 ± 1.4	5.4±2.1	6.7 ± 1.3
Beef Fillet Sate Spice	5.6±1.8	6.5±1.2	5.8±1.8	7.0±1.0	4.3±2.6	6.8±0.9	5.0±2.0	6.8±1.0	4.9±2.3	6.8±1.0
Beef Minced Honey	5.1±2.2	6.3±1.2	4.7±1.9	6.6±1.3	5.4±1.9	6.2±1.3	4.8±2.2	6.0±1.4	4.9±2.3	6.3±1.3
Beef Minced Black Pepper	5.8±1.7	6.1±1.1	5.8±1.7	6.0±1.6	5.8±1.7	5.8±2.0	5.5±1.7	6.5±1.6	5.5±2.0	5.8±1.9
Beef Minced Sate Spice	4.5±1.7	5.8±0.6	5.0±1.9	6.3±1.2	3.3±2.1	5.9±1.3	3.3±2.1	6.1±1.6	3.6±2.0	6.1±1.2
Chicken Fillet Honey	6.3±1.2	5.5±1.7	5.6±1.5	5.7±2.1	5.5±2.1	6.7±1.2	5.9±2.0	7.0±1.0	5.8±1.7	6.3±1.5
Chicken Fillet Black Pepper	6.9±1.1	6.6±1.0	6.3±1.3	6.8±1.2	5.8±1.4	6.8±1.0	6.6±0.9	6.9±0.9	5.9±1.5	6.7±1.0
Chicken Fillet Sate Spice	5.8±1.9	6.8±1.2	5.8±1.9	7.2±1.0	4.8±1.8	7.3±1.1	5.1±2.0	7.1±0.9	5.3±1.7	7.0±1.2
Chicken Minced Honey	5.0±2.0	4.9±1.4	5.4±1.5	5.2±1.7	4.4±2.1	5.8±1.6	5.1±1.8	6.1±1.2	4.9±1.6	5.8±1.6
Chicken Minced Black Pepper	5.4±1.5	5.5±1.0	6.2±1.6	5.5±1.7	4.1±1.8	6.3±1.1	4.8±2.0	6.0±1.0	5.1±1.6	5.8±1.0
Chicken Minced Sate Spice	4.1±1.8	4.9±1.7	4.9±2.0	5.8±1.8	2.8±1.6	5.3±1.9	2.4±1.1	5.3±1.8	2.9±1.5	5.0±1.8

* F 1 = Formulation 1, F 2 = Formulation 2

REFERENCES

AOAC (1995). Official Methods of Analysis of AOAC International (16th Edition). AOAC International Publication, Aarlington, VA, USA.

Barbanti, D., & Pasquini, M. (2005). Influence of cooking conditions on cooking loss and tenderness of raw and marinated chicken breast meat. *LWT*, **38**: 895–901.

Department of Defense (DOD) (2006). Operational Rations of the Department of Defense 7th Edition. U.S Army Natick Soldier RD&E Center, Department of Defense, United States of America.

Froning, G.W. & Sackett, B. (1985). Effect of salt and phosphate during tumbling of turkey breast muscle on meat characteristics. *Poult. Sci.*, **64**: 1328-1333.

Lemos, A. L. S. C., Nunes, D. R. M., & Viana A. G. (1999). Optimization of the still-marinating process of chicken parts. *Meat Sci.*, **52**: 227-234.

Malaysian Armed Forces (MAF) (1993). Malaysian Defence Specification; MDS 461:1989, Amended 1993-Beef '*Rendang*' Pouched Halal. Malaysian Armed Forces, Malaysia.

Murphy, R. Y. & Marks, B. P. (2000). Effect of meat temperature on proteins, texture and cook loss for ground chicken breast patties. *Poult. Sci.*, **79**: 99–104.

Sheard, P.R., Nute, G.R. & Chappell, A.G. (1998). The effect of cooking on the chemical composition of meat products with special reference to fat loss. *Meat Sci.*, **49**: 191-217.

Stone, H., and Sidel, J.L., (1993). Sensory Evaluation Practices (2nd Edition). Academic Press San Diego, CA.

Siong, T.E., Noor, M.I., Azudin, M.R. & Idris, K. (1997). Nutrient Composition of Malaysian Food (4th Edition). Institute for Medical Research, Kuala Lumpur.

Wikipedia (2009). Meals Ready to Eat. Available online at: http://en.wikipedia.org/wiki/MRE (Last access date: 11th February 2009).

THE EFFECT OF LOADING SEQUENCE ON THE FATIGUE LIFE OF THE RMAF PC-7 MKII AIRCRAFT

Mohd Yazid Ahmad[1], Siti Rozana Yusuf[2], Shamsiah Kalil[1], Syed Roslee Sayd Bakar[1], Ahmad Khairy Amat Zaini[1], Azhar Idris[2], N. Kamarudin[3], Mohd Yusuf Ahmad Tarmizi[4] & Ang Eu Jin[4]

[1]Science & Technology Research Institute for Defence (STRIDE),
43000 Kajang, Selangor

[2]Markas Tentera Udara, Wisma Pertahanan, Jalan Padang Tembak,
50634 Kuala Lumpur

[3]PUSPEKA, Pangkalan Udara Subang, 40000 Shah Alam, Selangor

[4]CAIDMARK Sdn Bhd, Damansara Utama, 47400 Petaling Jaya, Selangor

*Email: mya.pst@mod.gov.my

Abstract

This paper presents some of the early results of a fatigue coupon test program carried out by the Science & Technology Research Institute for Defence (STRIDE). The primary purpose was to obtain results from coupons with a material typical of some regions of the critical structure of the RMAF PC-7 mk II aircraft. A spectrum representative of RMAF PC-7 fleet fatigue usage was used. The coupons were representative of the material and geometry of a structural detail that has been found to be fatigue-critical in the 7075 T6 high strength aluminium alloy wing main spar component. Following the tests, quantitative fractography was used to produce crack growth curves for each of the fatigue specimens. This paper describes the test spectra, test methods, some of the early test results and examines the effect of loading sequences on fatigue crack growth rate and to establish a measure of the severity of the sequences from which the fatigue cracks initiated.

Keywords: *Fatigue coupon test; Crack growth rate; Load Spectra; Fatigue prediction.*

1. INTRODUCTION

Like any other air force in the world, the Royal Malaysian Air Force (RMAF) is adopting and implementing the Aircraft Structural Integrity Program (ASIP) (MIL-STD-1530, 1996) comprehensive tasks, that covers Aircraft Structural Integrity (ASI) management. There are two fundamental concepts of ASI management; to develop a certified aircraft structural baseline based on configuration, role and environment, and to continually assess against the baseline throughout aircraft service life until withdrawal. These concepts assure that the certification baseline established during the design stage is maintained throughout the service life of the aircraft and this is where usage monitoring is important in order to identify any baseline variation.

Having ASI management in place would assist the RMAF to assure aircraft safety throughout the aircraft life, to maximise aircraft availability by predicting impending and potential damage thus preventing aircraft from unscheduled repair, and to minimise cost of ownership by accurately planning the details and timing of structural upgrades and life extension options.
The Science & Technology Research of Institute for Defence's (STRIDE) role in the RMAF ASI management is to develop and maintain ASI capabilities that support RMAF operations. This includes structural design analysis, fatigue testing, and defect or failure detection capabilities. Through this R&D Project, Coupon Fatigue Testing is used as a stepping stone to develop the capabilities that is required by STRIDE to deliver the role. As part of the project, this paper will report an early investigation work carried out to study the effect of loading sequences on the fatigue crack growth rate of selected critical components of the RMAF PC-7 mk II aircraft.

1.1 Fatigue Life Management

Fatigue Life Management (FLM) involves the synthesis of usage data, data analysis methods and processes, and fatigue or damage tolerance analysis. Analysis methods for FLM are directly related to the aircraft's certification basis and are therefore influenced by either:

i) Safe Life Aircraft. For aircrafts designed and operated under the safe life philosophy, the analysis determines fatigue life expended (or fatigue index) for each individual aircraft.
ii) Safety by Inspection. For aircrafts designed and operated under the damage tolerance philosophy, the analysis determines aircraft inspection thresholds and intervals for the fleet or for individual aircraft.

FLM delivers outputs such as fatigue life expended index (or fatigue index), inspection intervals, predictions of remaining aircraft fatigue life and planned withdrawal date (PWD) assessments, and recommended fleet management actions (for example, aircraft rotation, changes to mission or mission mix, or changes to aircraft role).

1.2 Damage Hypothesis

The standard damage hypothesis used is Miner's rule (*Stephens*, 2001).This says that, for each load in the fatigue spectrum, the damage D incurred per unit time is given by:

$$D = \frac{n}{N} \tag{1}$$

where n is the estimated number of load cycles experienced at the specified load level. N is the allowable number of cycles at the same specified load level and is defined by the working *S/N* curve for the component.
Using the subscripts ith flight condition in the fatigue spectrum, jth load level in the ith flight condition (for block loads, $j = 1$, for cycle counting, $1 \leq j \leq k$, where k is the number of sub-blocks) then the fatigue damage incurred by the ith flight condition on a particular component is given by Miners Rule as:

$$D_i = \sum_{j=1}^{k} \frac{n_j}{N_j} \tag{2}$$

The total damage is then given by:

$$D_{TOTAL} = \sum_{i=1}^{m} D_i \tag{3}$$

Where m is the total number of flight conditions. For many components, most of the D_i values are zero. In other words, for most components, only a few flight conditions cause fatigue damage.
Miner's rule does not take account of the sequence of loads and hence that information is not incorporated in a design usage spectrum. This is known to be incorrect in that the occurrence of large positive or negative stresses in a component can significantly affect the growth rate of fatigue cracks. Mean load effects may or may not be taken into account. If they are taken into account, Goodman correction is often used.

2. METHODOLOGY

The coupons were intended to closely match the material in the RMAF service and the spectra used to test them are intended to closely match the data used in fleet fatigue monitoring. Thus the:

i) Coupons have the same properties, material characteristics and surface finish representative of the aircraft critical component, mainly wing main spar attachment.

ii) Spectra are representative of RMAF PC-7 mk II fleet processing, and were produced for both benign and severe aircraft usage.

2.1 Test Sequences

The coupon tests will be conducted using five different sequences from the operational g-meter or Nz data from the RMAF PC-7 mk II fleet aircraft. These sequences were selected to represent approximately 200 hours operational flights of the fleet since 2002 to 2005 and the spectrum for this test has only 3289 load line. The five spectra selected to represent a range of aircraft usage severities ranging from benign to severe. Generation of these usage spectra are provided in Ahmad *et.al* **(**2006)
Even though there was no flight recorded strain gauge data for this aircraft, it has been recorded (Anderson, 2000) that the wing main spar attachment loads are directly related to Nz. Nz exceedances from the aircraft can be used to as a representative test loading spectrum at these location.

2.2 Coupon Geometry

The coupons used for testing have been designed to duplicate a detail on the wing critical component using "dog bone" type geometry, conforming to ASTM E468 as shown in Figure 1. This coupon has a test area (A_t) of 200 mm^2 and the geometry produces an analytical stress concentration factor (K_t) of 2.22. The detailed specifications for the specimen manufactured are presented in (ASTM E468: 90, 2004)

2.3 Coupon Material Properties

The coupons used in the tests were made of aluminium alloy Al 7075 in the T6 heat treatment condition.

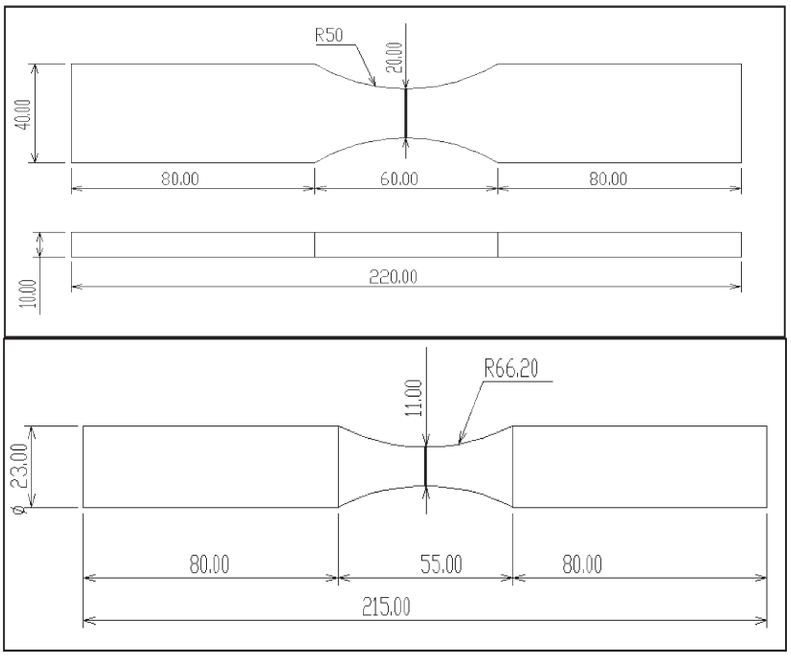

Figure 1: The geometry and dimension of the test coupons.

2.4 Test Loads

The coupon test program was intended to be completed in five phases which each phase using the same usage spectrum of the PC-7 mk II fleet but with different load sequence. Figure 2 shows the five load sequences that are going to be used in the test program. A minimum of five coupons will be used to test most sequences in order to obtain statistical confidence (up to now we only managed to run one specimen and one load sequence).
The testing of the specimens was carried out using a standard servohydraulic Instron 250kN fatigue test machine. The test frequency for these coupon tests was 3 Hz to ensure that potential unrepresentative time dependent effects, caused by applying loads to the specimens at higher frequencies, were not induced. The load was applied as a sine wave function.

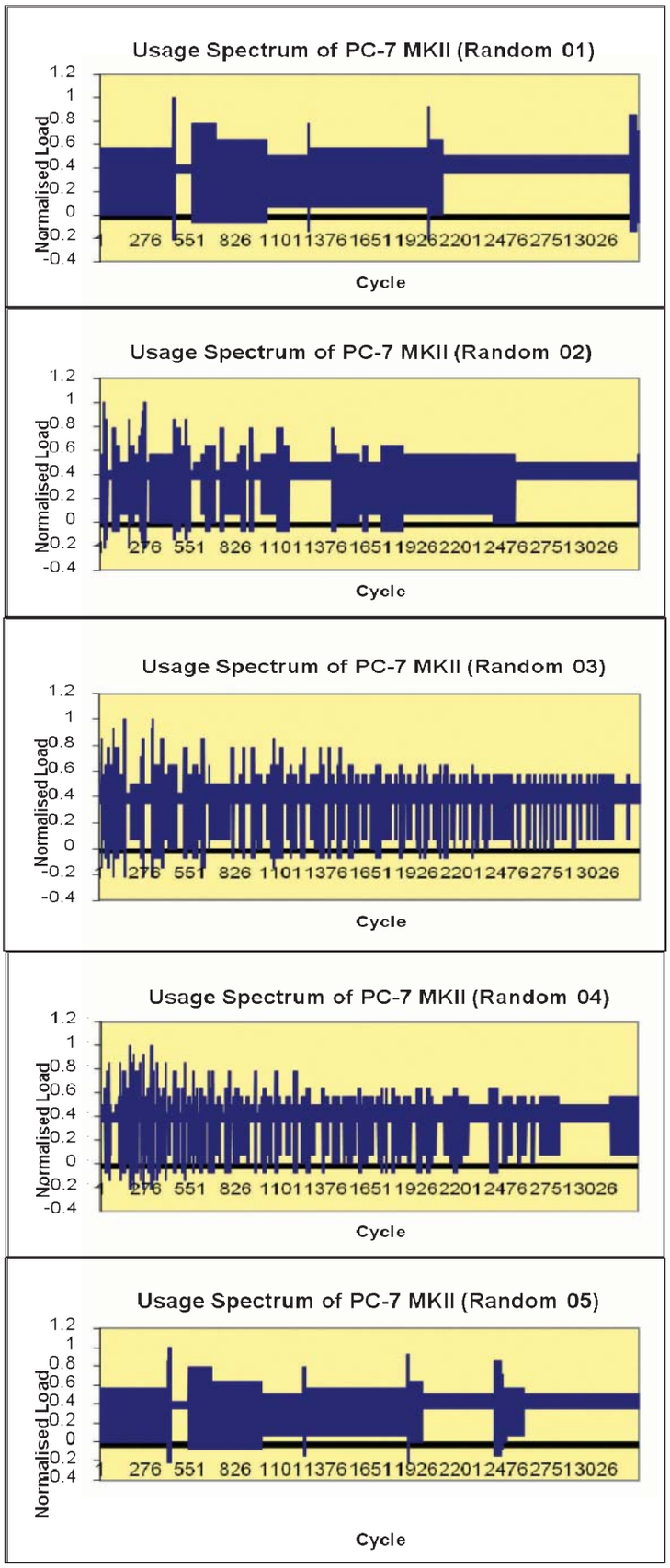

Figure 2: Five load sequences for the test program. Random 01, 02, 03, 04 and 05.

Note that the reference stress of 21.9 MPa and a normalised reference of 1.0 (Raymond, 2001) has been used in the test. This reference stress is a relationship between a stresses per g at the location of wing root bending moment (Matricciani, 1997).

2.5 Crack Growth Measurement

Quantative fractography (QF) will be conducted using both high and low power optical microscopes as well as an SEM in both secondary electron and backscattered modes. QF will be carried out on the main cracks from each of the coupons tested. This allows a complete picture of the crack growth to be assembled assuming that each repeat of the pattern was equivalent to a single load spectrum sequence. The coupon tests will produce repeating markings that would found to be very consistent with the type and spacing expected for fatigue growth per spectrum under these conditions.
One of the features of fatigue crack growth previously noted by many researchers (Barter,,2003a, 2003b).
When examining cracks grown with realistic aircraft fighter spectrum loads, is that they grow at approximately a constant exponential rate for most of their life. The crack growth rate also clearly shows an increase with increasing stress. On the other hand, a retardation (or a decrease in slope) of crack growth rate was clearly shown in the case where the overload precedes each block. While the single spike produced some increase in the total life results, the single spike did not affect the general crack growth rate as shown by the similarity between the single spike and no spike curves (Pell *et al.*, 2003).

Figure 3(a) shows a typical fracture surface of a fractured coupon, showing a distinguish fatigue fracture feature, radial beach marks followed by a ductile failure mode. Figure 3(b) shows a 3D image of the fracture surface taken using an infinite focus microscope that can used to measure the fatigue crack length of the coupon.

Our first test results from the first coupon showed that the total number of cycles to failure was 1.57×10^{10} cycles, which took about three month before the coupon completely fractured.
Since the number of fatigue fractured specimen is only one, currently we have not carried out a quantative fractography to produce crack growth curves for each of the fatigued specimens. Hence, a detailed interpretation of the crack growth has not been made yet, including a measure of the severity of the flaws from which the fatigue cracks initiated.

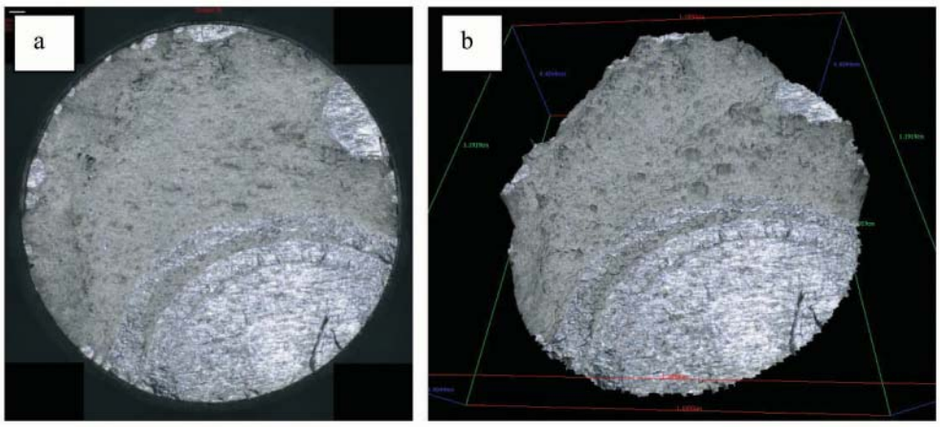

Figure 3: Fracture surface of a coupon after a fatigue test (5x magnification).

3. CONCLUDING REMARKS

This paper has not presented the overall results of the coupon fatigue test program; however this aluminium alloy 7075 T6 coupon fatigue test program primarily aimed at producing experimental results that could be used to examine the effect of loading sequences and the severity of the sequences of the RMAF PC-7 fleet, has been summarised in this paper. Five spectra representative of the RMAF usage were tested on several reference stress levels. The bulk of the coupons were representative of the wing main spar. The test sequences were assembled from fleet or test data in a manner representative of the process used by the

RMAF aircraft service life monitoring program to assess fatigue damage accumulation of individual RMAF aircrafts.
Consistent total life and crack growth results with low levels of scatter will hopefully be obtained for all the spectra and stress levels considered. The results of the mean life value can be used for analyses with a high degree of confidence. An important aspect of the structural integrity management of an aircraft fleet is the validity and accuracy of the "tools" used to assess the life of individual aircraft. The results that will be presented in this project can be later used to assess the validity of the damage algorithms used to assess manoeuvre-induced damage to the critical structure of the RMAF PC-7 mk II, thus meeting an important airworthiness requirement.

ACKNOWLEDGMENTS

The authors wish to acknowledge the contributions of the RMAF PC-7 squadron and PUSPEKA for providing the flight data and all the support staff of STRIDE Structural Mechanics Branch for the successful outcome of this project.

REFERENCES

Ahmad, M.Y., Yusuf, S.R., Khalil, S., Bakar, S.R.S., Idris, A., Kamarudin, N., Tarmizi, M.Y.A., Jin, E. (2006). Development of Fatigue Loading Spectrum for the RMAF, *Proceeding of Defence Research Convention DRC 2006*, STRIDE, Lumut, Perak.

Anderson, R.G. (2000). PC9/A Fatigue Test, Life Assessment Based on the Results of the Fatigue Test, DSTO Report DSTO-TN-0228.

ASTM E468: 90(2004) Standard Practice for Presentation of Constant Amplitude Fatigue Test Results for Metallic Materials, *ASTM international*.

Barter, S.A. (2003a). Fatigue Crack Growth in Several 7050T7451 Aluminium Alloy Thick Section Plates with Aircraft Manufacturers and Laboratory Surface Finishes Representing Some Regions of the F/A-18 Structure, Department of Defence, DSTO Report *DSTO-TR-1539.*

Barter, S.A. (2003b). Fatigue Crack growth in 7050T7451 Aluminium Alloy Thick Section Plate with a Surface Condition Simulating Some Regions ff F/A-18 Structure, Department of Defence, DSTO Report *DSTO-TR-1458*.

Matricciani, E. (1997). PC9/A Fatigue Damage Model, DSTO-DDP-0373.

MIL-STD-1530 (1996). Aircraft Structural Integrity Program (ASIP).

Pell, R.A., Mazeika, P.J. and Molent, L. (2003) The Comparison of Complex Load Sequences Tested at Several Stress Levels by Fractographic Examination*, ICAF 2003 – Fatigue Of Aeronautical Structures As An Engineering Challenge, Proceedings of the 22nd Symposium of the International Committee on Aeronautical Fatigue,* May 2003, Lucern, Switzerland.

Raymond, G. & Parker, A. (2001). Full-Scale Fatigue Test of a Pilatus PC9/A Trainer Aircraft, *DSTO* Report DSTO-TR-1107.

Stephens, R. I. (2001). Metal Fatigue in Engineering. John Wiley & Sons Inc., New York.

KAJIAN *THERMAL SIGNATURE* KE ATAS PESAWAT SASARAN BANSHEE

Muhamad Muslim b. Tasdik

Bahagian Teknologi Instrumentasi & Elektronik, STRIDE
Taman Bukit Mewah Fasa 9, 43000 Kajang, Selangor D.E.
Tel: 03-87324400
Fax: 03-87348695
E-mail: muhamadmuslimstride@yahoo.com

Abstrak

Angkatan Tentera Malaysia mempunyai peluru berpandu (misil) pertahanan udara Anza dan Igla yang menggunakan sistem penjejakan thermal signature. Semasa latihan, terdapat misil yang tidak dapat menjejaki pesawat sasaran Banshee dengan baik. Umumnya, thermal signature Banshee dipengaruhi oleh Pelbagai faktor terutamanya suhu dan emissivity permukaan pesawat serta jarak pesawat yang banyak dipengaruhi oleh serapan, serakan dan sintilasi atmosfera. Oleh itu, satu kajian telah dilaksanakan dengan menggunakan peralatan LWIR thermal camera FLIR SC3000 untuk menentukan keberkesanan tembakan misil tersebut semasa latihan di persekitaran pantai Lapangsasar Tanjung Logok, Kota Tinggi, Johor. Hasil kajian menunjukkan hot nose yang digunakan adalah terdiri dari bahan yang berkilat yang mempunyai emissivity yang rendah yang mengurangkan keupayaan misil menjejaki sasaran setelah pelancaran. Di samping itu, terdapat juga gangguan sintilasi yang besar.

Keywords: *Thermal Signature; Man Portable Air Defence System; Homing System; Emissivity; Scintillation.*

1. PENGENALAN

Peluru berpandu pertahanan udara *surface-to-air missile* (SAM) merupakan asset yang penting dalam sistem pertahanan Angkatan Tentera Malaysia. Pada masa ini, Rejimen Artileri DiRaja Tentera Darat mempunyai peluru berpandu pertahanan udara Anza MK-II buatan Pakistan dan Igla SA-18 buatan Rusia. Kedua-duanya merupakan sistem peluru berpandu jarak dekat *Man Portable Air Defence System* (MANPADS) yang menggunakan sistem pengesanan sasarannya berdasarkan *thermal/infrared* (IR) *signature.* Jarak keberkesanan tembakannya adalah sehingga 5 km dan mencapai ketinggian sehingga 4,000 m.

Secara lazimnya, *thermal signature* sesuatu objek akan bergantung kepada beberapa faktor seperti bentuk dan saiz objek, suhu dan *emissivity* permukaan objek, latarbelakang di mana pengukuran dilaksanakan dan julat lebarjalur penderia atau *thermal camera / imager* yang digunakan. *Thermal signature* juga dipengaruhi oleh jarak di antara objek yang dicerap dengan *thermal camera* di mana ianya akan mengalami gangguan atau pengurangan akibat serapan, serakan dan sintilasi oleh medium perambatan di udara yang terdiri dari molekul-molekul gas dan partikel-partikel air yang berubah-ubah mengikut tempat, cuaca dan masa (Koop, 2005).

Umumnya, sesuatu aset pertahanan perlu melalui proses ujian medan untuk mengesahkan keupayaan dan kesiagaan dari masa ke semasa. Selaras dengan itu, pengujian peluru berpandu tersebut dilaksanakan dengan menembak sasaran di udara seperti *Banshee Target Drone.* Ia merupakan pesawat kawalan jauh yang digunakan sebagai sasaran tanpa pemandu yang bersaiz kecil, iaitu panjang dan lebarnya kurang dari 3 m dan menggunakan enjin *rotary* yang kecil (Vectorsite, 2007). Oleh itu *thermal signature* enjinnya juga adalah kecil dan sukar dikesan oleh peluru berpandu. Walau bagaimanapun dalam latihan pada masa ini, pesawat Banshee telah ditambah dengan *hot nose* supaya peluru berpandu dapat menjejaki *thermal signature* pesawat dari mana-mana arah terutamanya dari arah hadapan di mana peluru berpandu Anza tidak dapat menjejaki (*lock*) pesawat sasaran dari arah hadapan semasa latihan yang terdahulu.

Dari pemerhatian semasa melaksanakan ujian medan, didapati peluru berpandu Anza dan Igla tidak dapat menembak dengan baik sasaran pesawat kawalan jauh *Banshee* yang dilengkapi dengan *hot nose.*

Terdapat peluru berpandu yang mengarah ke laut (bayang matahari), ke atas (langit / matahari) atau berlalu tanpa menuju ke arah sasaran. *Thermal signature* dari pesawat *Banshee* tidak dapat dikesan dengan baik oleh peluru berpandu tersebut. Mengapakah fenomena ini boleh berlaku?

2. SISTEM PENJEJAKAN MANPADS

Sistem peluru berpandu pertahanan udara MANPADS merupakan suatu sistem persenjataan yang sangat berkesan dan berkembang di seluruh dunia. Ianya mula dibangunkan pada akhir tahun 1950an untuk memberikan tentera darat perlindungan dari pesawat musuh yang terbang rendah terutamanya helicopter (Wikipedia, 2008). Kebanyakan MANPADS menggunakan panduarah *homing system* untuk memintas sasaran dengan berkesan. Misil yang menggunakan *homing system* juga dikenali sebagai misil pasif kelas "*launch and leave"* atau "*fire and forget"*. Ia tidak memancarkan sebarang isyarat semasa mengesan sebaliknya hanya mencerap *signature* radiasi dari sasaran yang biasanya terdiri dari *thermal, ultraviolet* (UV) dan cahaya nampak (*visible light*) (Siorius, 2004). Rajah skematik sistem ini diberi di dalam Rajah 1.

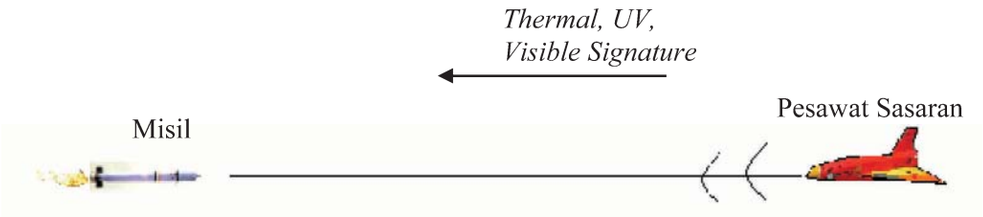

Rajah 1: Pengesanan misil yang menggunakan panduarah *homing system*.
(Sumber: Siouris, 2004)

Di dalam *homing system*, panduarah sasaran adalah di dalam peluru berpandu (misil) yang melibatkan gerakan relatif di antara sasaran dan misil. Kawalan aerodinamik dari konfigurasi sayap misil akan digunakan untuk mengawal arah penerbangan yang menggunakan *self-propelled system*. Seterusnya, pemprosesan data di dalam sistem tersebut akan memberikan maklumat sasaran yang berterusan sehingga ke titik pintasan. Di samping itu, elemen penderianya mempunyai sudut arah yang kecil (*sharply directional*) supaya berkesan untuk sudut yang kecil di antara misil dan sasaran. Oleh itu, MANPADS biasanya perlu ditembak ke arah sasaran yang dikehendaki dan seterusnya pemprosesan data di dalam *homing system* yang akan memberi arahan pergerakan yang lebih tepat (Siouris, 2004).

Terdapat beberapa generasi MANPADS sehingga ke hari ini. Untuk misil generasi pertama, ia mempunyai keupayaan mengejar sasaran dari arah belakang kerana *seeker* hanya boleh menjejaki pesawat setelah pesawat tersebut melepasi kedudukan penembak. Ini adalah kerana dari arah belakang, enjin pesawat akan terdedah sepenuhnya kepada *seeker* misil dan memberikan *thermal signature* yang mencukupi untuk penjejakan. Misil generasi pertama sangat mudah dipengaruhi oleh *thermal signature* dari sumber-sumber persekitaran termasuk matahari, yang meyebabkan para pakar merasakan ianya tidak lagi sesuai digunakan. Contohnya adalah misil Redeye dan SA-7 (Wikipedia, 2008).

Seterusnya, bagi misil generasi kedua, ia menggunakan bahan penyejuk (*coolant*) yang telah dipertingkatkan untuk menyejukkan penderia *seeker* yang membolehkannya untuk menapis kebanyakan gangguan sumber IR dari persekitaran dan juga ianya membolehkan penjejakan profil pesawat dari arah hadapan dan sisi. Misil ini juga menggunakan teknologi untuk mengatasi suaran (*decoy*) yang mempunyai pengesanan UV. Contohnya adalah generasi awal misil Stinger dan SA-14 (Wikipedia, 2008).

Misil generasi ketiga menggunakan pengesan tunggal atau berganda (*multiple*) untuk menghasilkan suatu *quasi-image* sasaran dan mempunyai keupayaan untuk mengenalpasti dan mengenepikan suaran anti misil yang dilancarkan dari pesawat. Contohnya misil Stinger B, SA-18 dan Mistral. Manakala untuk misil generasi ke-empat, ia mempunyai sistem panduarah gabungan *focal plane array* dan sistem penderia termaju

yang lain yang membolehkannya mengesan sasaran pada jarak yang lebih jauh. Beberapa model misil generasi ini sedang dibangunkan oleh negara Russia, Japan, Perancis dan Israel.

Misil yang menggunakan penjejakan *thermal signature* direkabentuk untuk memproses isyarat dari sumber haba pesawat yang datang dari permukaan pesawat yang panas (*aerodynamic heated edges),* enjin, ekszos atau *plume* ekszos. Oleh itu, bagi sasaran di udara *thermal signature* adalah sukar untuk ditutup. Contohnya bagi pesawat pejuang, suhu ekzosnya adalah sekitar 950^{o}C. Kelebihan penderia ini adalah ia boleh beroperasi pada waktu siang dan malam walaupun dalam keadaan *total darkness* untuk mengesan *hot-spot* (Kopp, 2005). Dalam Rajah 2 diberikan amplitud *thermal signature* untuk sebuah pesawat pada sudut 0^{o} hingga 180^{o} untuk jalur gelombang (*band*) 3 – 5.5 mikron (MWIR) dan 8 – 12 mikron (LWIR). Rajah tersebut menunjukkan kedua-dua jalur meliputi keseluruhan pesawat tetapi terdapat perbezaan amplitud *thermal signature* yang ketara di bahagian asap (*plume*) pesawat.

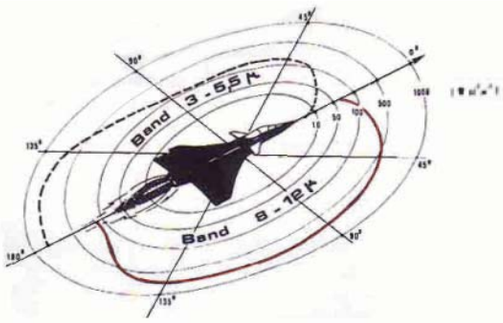

Rajah 2: Amplitud *thermal signature* untuk sebuah pesawat
(Sumber: Cedip *IR System*)

Kajian mendapati, amplitud *thermal signature* pesawat adalah berkadaran dengan salingan kuasadua jarak (*inverse square of the range)* (Akram 1991). Pengurangan amplitud berlaku kerana semasa transmisi *thermal signature* di dalam atmosfera, ia akan dipengaruhi oleh beberapa faktor seperti serapan, serakan dan sintilasi. Sintilasi atau kerlipan adalah perubahan amplitud isyarat cerapan bagi sesuatu objek yang mengeluarkan sumber isyarat seperti haba atau cahaya yang dicerap menerusi atmosfera. Ia berlaku disebabkan oleh perubahan ketumpatan dan suhu udara yang bergelora di sepanjang garis penglihatan pencerap.

Hingar sintilasi (*scintillation noise*) memberi kesan kepada amplitud isyarat pesawat sasaran yang diterima oleh penderia *thermal* pada misil. Ianya boleh menjadi faktor penting semasa proses penjejakan (*engagement*). Contohnya, pengesanan isyarat sasaran akan menjadi kabur (*fade*) yang boleh menyebabkan kelewatan masa penjejakan. Dalam pengesanan yang minimum (*marginal*), pengurangan isyarat sasaran boleh menyebabkan kehilangan penjejakan (Siouris, 2004). Selain itu, faktor serapan dan halangan terutamanya oleh wap air menyebabkan misil tidak boleh menjejaki sasaran ketika hujan.

3. KAEDAH PENGESANAN *THERMAL SIGNATURE*

Peralatan yang digunakan adalah *Long Wave* (LW) *Thermal Camera* model FLIR SC3000 dengan kanta 5^{o} (Rajah 3) manakala perisian pemproses imej *thermal signature* yang digunakan adalah ThermaCam Researcher.

Rajah 3: Peralatan menghadap ke laut di Lapangsasar Tanjung Logok.

4. HASIL DAN PERBINCANGAN

Imej-imej *thermal signature* pasawat Banshee yang diambil untuk kajian adalah semasa pihak Rejimen Artileri DiRaja Tentera Darat melaksanakan Ujian Medan pada 24-26 April 2008 di Tanjung Logok, Kota Tinggi, Johor. Imej-imej visual daripada kamera digital juga disertakan sebagai perbandingan.

Dalam Rajah 4(a) menunjukkan pesawat Banshee sedia berlepas dari pelantar penerbangan. Ianya telah dilengkapkan dengan *hot nose* supaya misil Igla dan Anza dapat mengesannya dengan mudah dari arah hadapan pada jarak penjejakan yang diperlukan. Imej tersebut menunjukkan permukaan *hot nose* adalah berwarna aluminium dan berkilat yang menunjukkan ia mempunyai nilai *emissivity* yang rendah yang menyebabkan suhu yang dicerap oleh *thermal camera* juga menjadi rendah berbanding dengan suhu sebenar. Di sebelahnya, dalam Rajah 4(b) adalah *thermal signature* pesawat Banshee yang menunjukkan dengan jelas *hot nose* dan enjin Banshee tersebut.

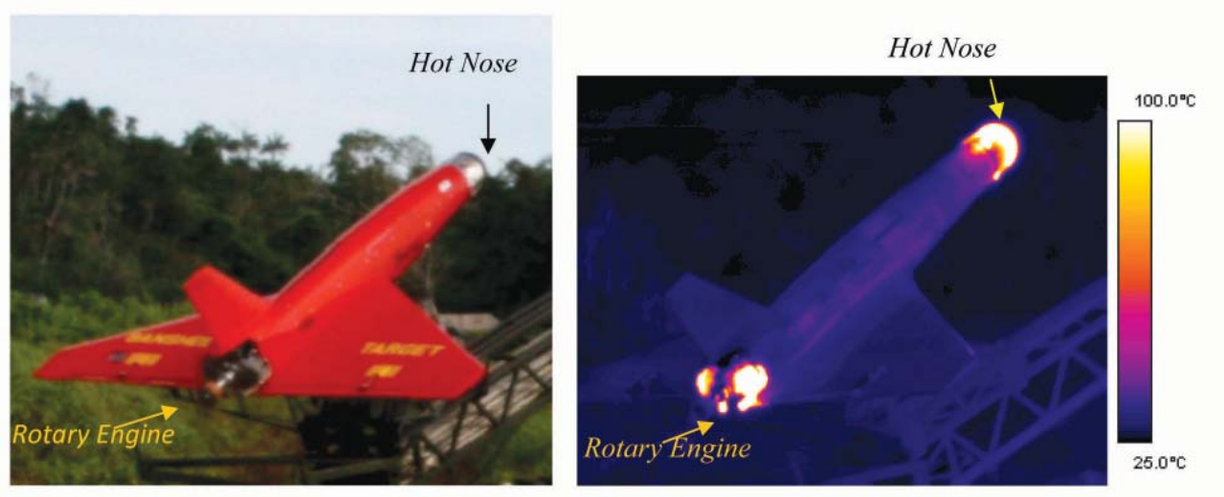

(a) Imej Visual Banshee

(b) Imej *Thermal Signature* Banshee

Rajah 4: Imej visual dan *thermal signature* pesawat Banshee yang sedia berlepas dari pelantar.

Penerbangan pesawat Banshee di udara adalah mengikut laluan autopilot yang telah ditetapkan. Ia mendekati tapak pelancar misil dari arah hadapan pada jarak 10 km. Setelah menghampiri pada jarak 7 km, Banshee akan mengeluarkan asap yang berwarna perang supaya mudah dikesan secara visual sehingga pada jarak 5 km. Seterusnya Banshee akan membuat pusingan "U" pada jarak sekitar 500 m dari penembak atau 860 m dari *thermal camera* penyelidik STRIDE. Kelajuan Banshee di udara adalah sekitar 57 m/s atau 205.2 km/j.

Imej *thermal signature* Banshee yang berlepas dari pelantar diberikan dalam Rajah 5 di mana dua kedudukan Banshee telah ditindan iaitu kedudukan (a) sejurus ia berlepas dan kedudukan (b) setelah 11.5 saat berlepas. Dari imej tersebut didapati suhu udara (*sky*) adalah sekitar 27^{o}C, suhu laut adalah 27^{o}C dan suhu daratan adalah 3^{o}C. Imej telah diambil pada 26 April 2008, pukul 9:34 pagi dalam keadaan cuaca yang cerah dengan kelembapan 77% RH. Seterusnya telah diplotkan graf suhu maksimum Banshee melawan masa yang diberi dalam Rajah 6. Suhu maksimum tersebut diperolehi dari setiap *frame* imej radiomatrik dimana frekuansi *frame* adalah 50 Hz. Ciri-ciri suhu maksimum diambil untuk dianalisa adalah kerana ianya berkadaran dengan pengesanan *thermal signature* Banshee iaitu semakin tinggi suhu maksimum maka semakin jelas *thermal signature* Banshee.

Dari Rajah 6, didapati suhu maksimum untuk *hot nose* Banshee adalah 124 ^{o}C semasa sejurus berlepas dan beransur-ansur berkurangan hingga ke 36^{o}C setelah sekitar 12.3 saat berlalu manakala bagi suhu maksimum enjin pula adalah 76^{o}C dan berkurangan hingga 38^{o}C. Suhu maksimum *hot nose* dan engin sebenarnya adalah tetap semasa pesawat terbang di udara tetapi penurunan suhu yang dicerap oleh *thermal camera* disebabkan oleh pengurangan amplitud *thermal signature* akibat serapan atmosfera dan beberapa faktor lain iaitu semakin jauh jarak objek ke *thermal camera*, maka semakin tinggi serapan atmosfera berlaku. Oleh itu, dalam kajian ini suhu Banshee yang dicerap bukanlah suhu sebenar pesawat. Dari halaju Banshee 57 m/s, maka jarak penerbangan yang sepadan untuk 12.3 saat adalah sekitar 1000 m dari *thermal camera*. Dari graf tersebut juga didapati imej *frame* yang berturutan menunjukkan suhu maksimum yang berubah (*fluctuate*) dengan ketara. Keadaan ini disebabkan oleh faktor sintilasi.

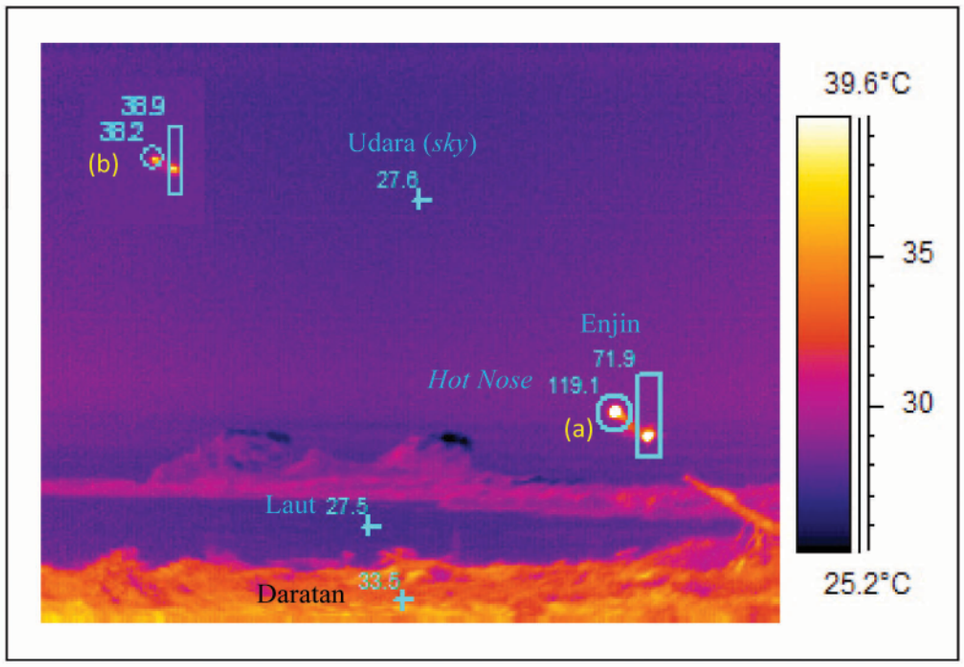

Rajah 5: Imej *thermal signature* Bashee yang berlepas dari pelantar dengan kedudukan (a) sejurus berlepas (jarak: 363 m) dan (b) setelah 11.5 saat berlepas (jarak: 1000 m).

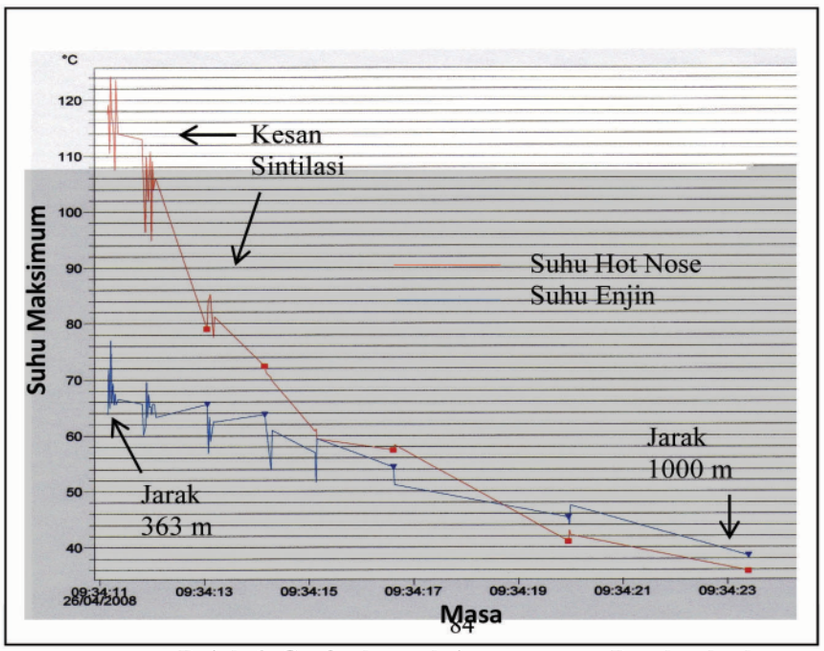

Rajah 6: Graf suhu maksimum semasa Banshee berlepas.

Dalam Rajah 7, diberikan graf profil suhu maksimum Banshee yang menghampiri tapak pelancar misil dari arah hadapan, kemudiannya telah ditembak dengan misil dan seterusnya menjauhi penembak. Beberapa imej *thermal signature* Banshee pada masa yang bersesuaian juga diberikan. Dari rajah tersebut, Banshee telah mula dikesan pada jarak sekitar 5 km dan semasa menghampiri penembak, graf menunjukkan suhu Banshee adalah berkadaran dengan kuasa dua jaraknya. Imej juga menunjukkan tembakan misil telah tersasar dan meletup sendiri (*self destruction*) jauh dari sasaran. Keadaan ini menunjukkan bahawa misil tersebut telah dapat *lock* pada sasaran tetapi tidak dapat menjejakinya dangan baik setelah pelancaran. Keadaan ini berlaku pada suhu Banshee yang kurang dari 49^{o}C pada jarak melebihi 2.3 km dari penembak. Graf tersebut juga menunjukkan suhu maksimum profil adalah 88^{o}C serta berlaku sintilasi yang kecil iaitu sekitar 4^{o}C.

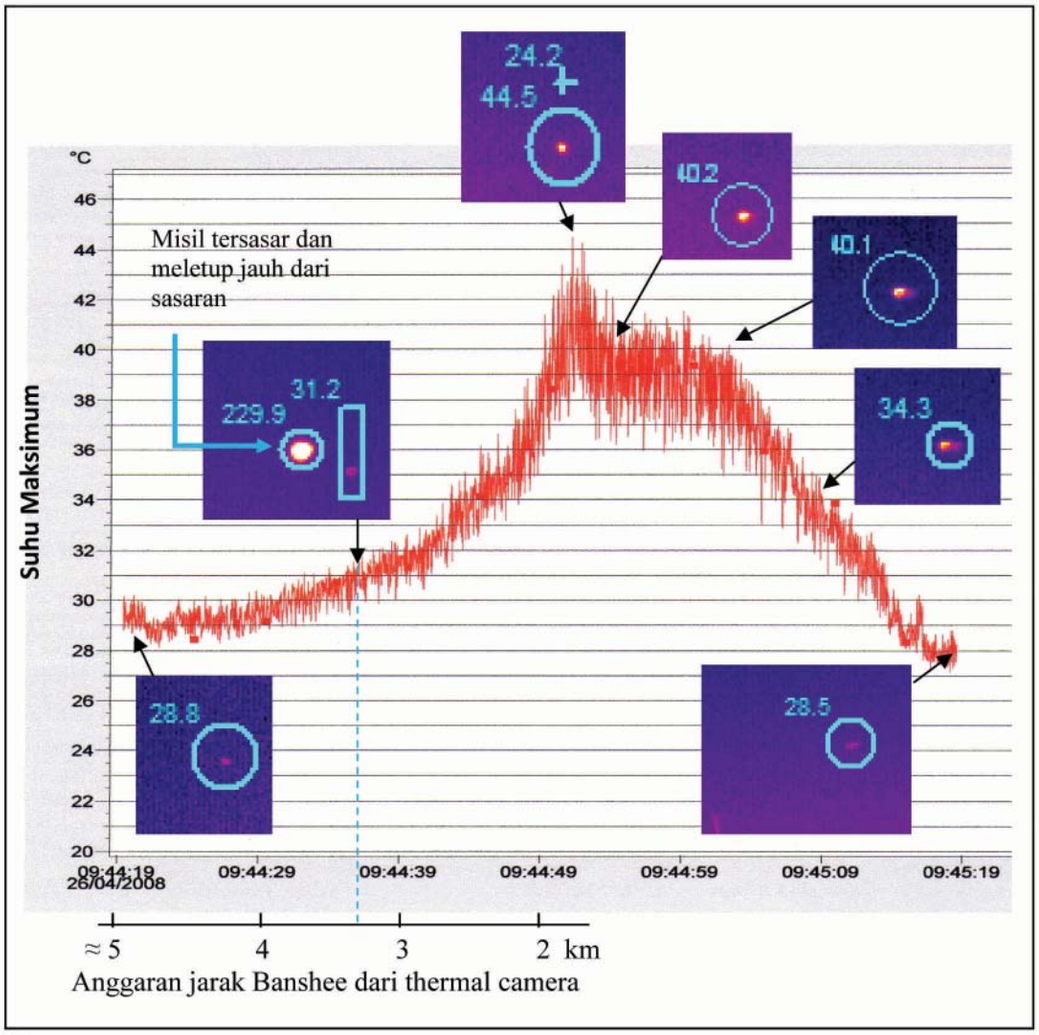

Rajah 7: Graf profil suhu maksimum untuk Banshee yang menghampiri dan menjauhi tapak pelancar misil pada 9.37 pagi.

Keadaan yang sama juga berlaku untuk penerbangan Bansee yang seterusnya seperti yang di tunjuk dalam Rajah 8. Dari rajah tersebut, tembakan misil telah dibuat pada suhu Banshee yang kurang dari 31^{o}C pada jarak lebih dari 3.2 km dari penembak menyebabkan misil tidak dapat menjejaki pesawat setelah pelancaran. Graf tersebut juga menunjukkan suhu maksimum profil adalah 44^{o}C serta berlaku sintilasi yang kecil iaitu sekitar 2^{o}C.

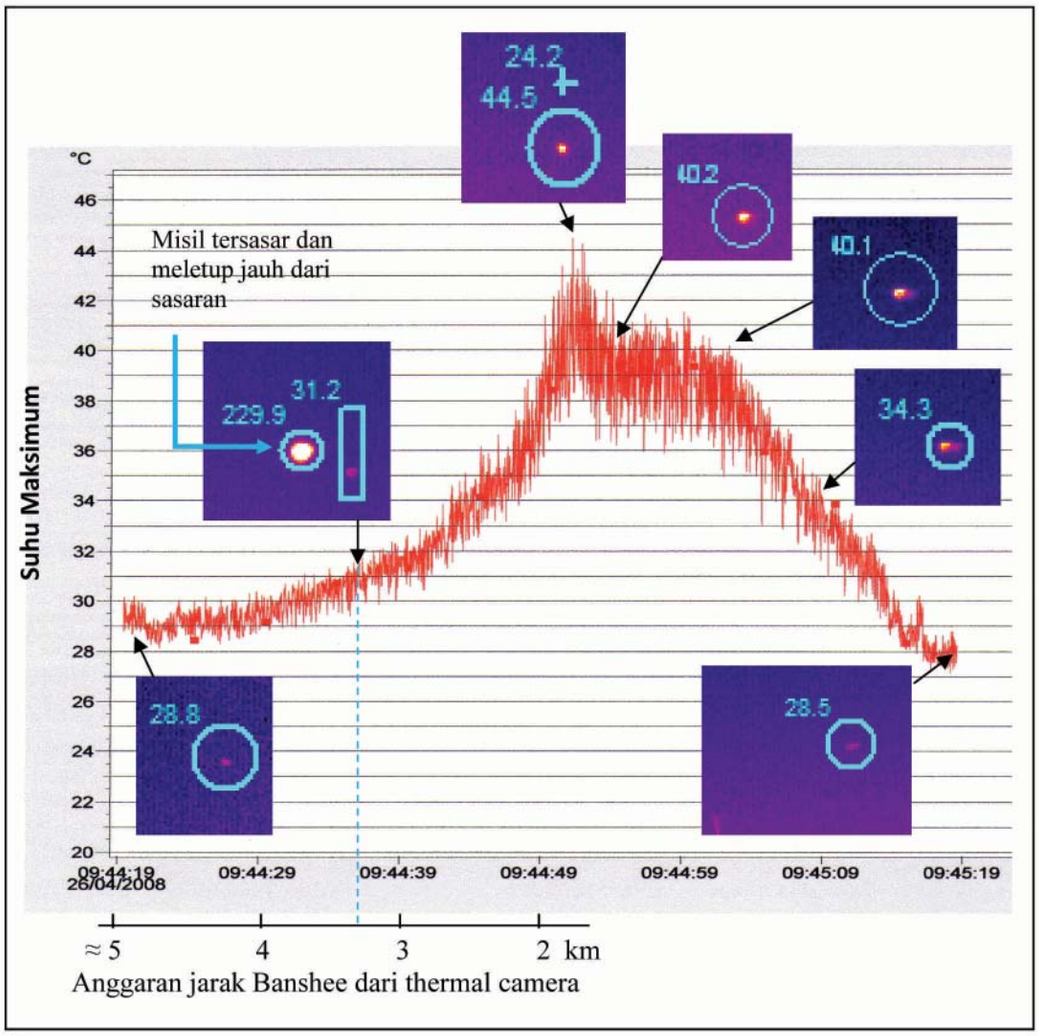

Rajah 8: Graf profil suhu maksimum untuk Banshee yang menghampiri dan menjauhi tapak pelancar misil pada 9.44 pagi.

Seterusnya dalam Rajah 9, didapati *thermal signature* Banshee telah dicerap dengan lebih jelas yang bermula pada jarak melebihi 5 km. Tembakan misil telah dibuat pada suhu Banshee yang lebih tinggi iaitu sekitar 88°C pada jarak lebih dekat iaitu kurang dari 1 km dari penembak. Walaupun misil tidak dapat menembak jatuh pesawat tetapi ianya dapat menjejaki pesawat dengan agak baik. Graf tersebut juga menunjukkan suhu maksimum profil adalah 168°C serta berlaku sintilasi yang besar iaitu sekitar 30°C.

Diberikan juga imej *visual* dan *thermal* untuk tembakan misil ANZA dan Igla seperti dalam Rajah 10 hingga Rajah 13. Kedua-dua misil dapat menjejaki dengan baik sasaran Banshee pada suhu sekitar 60°C. Imej tersebut tidak dapat dibuat analisa graf profil disebabkan *thermal camera* tidak fokus kepada Banshee sebaliknya kepada pergerakan misil.

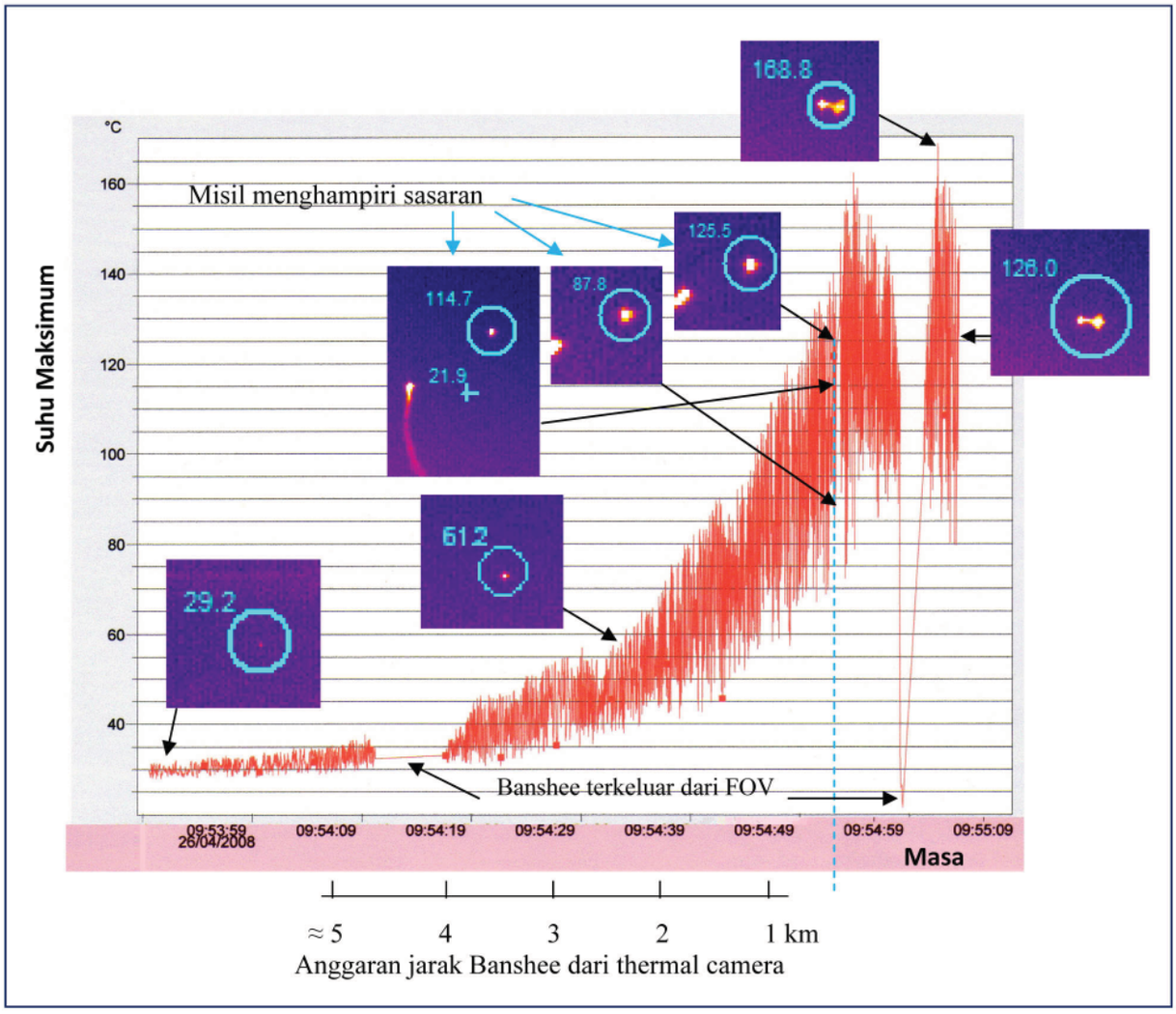

Rajah 9: Graf profil suhu maksimum untuk Banshee yang menghampiri dan membuat pusingan "U" (imej dari sisi) pada 9.54 pagi.

(a) Imej *visual*

(b) Imej *thermal*

Rajah 10: Tembakan misil Anza dilancarkan.

(a) Imej *visual*

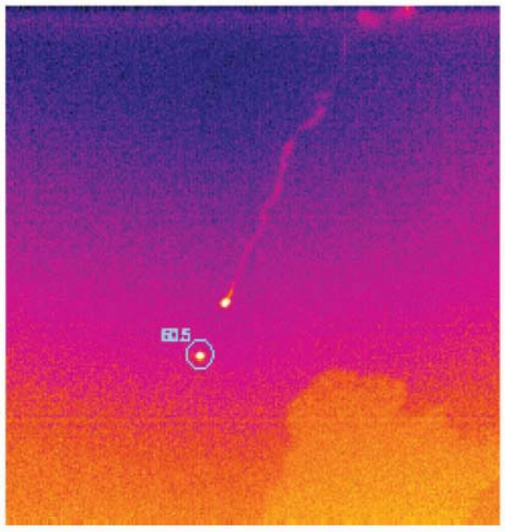

(b) Imej *thermal*

Rajah 11: Misil Anza menghampiri sasaran pada suhu Banshee 60°C.

(a) Imej *Visual*

(b) Imej *Thermal*

Rajah 12: Tembakan misil Igla dilancarkan.

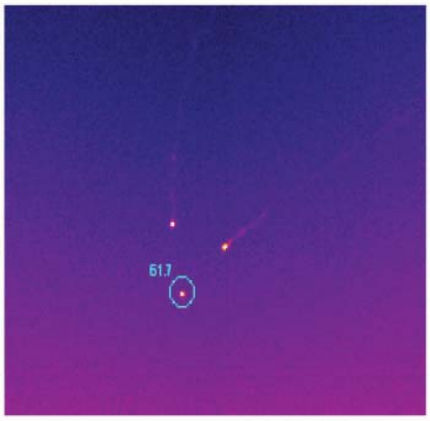

(a) Misil Igla menghampiri sasaran pada suhu Banshee 61°C

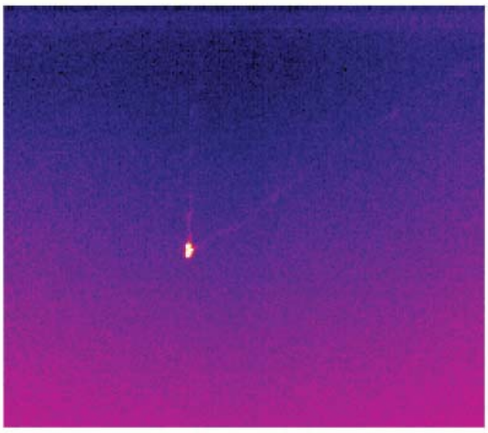

(b) Misil Igla hampir mengenai sasaran

Rajah 13: Imej *thermal* yang menunjukkan kedua-dua misil Igla menghampiri sasaran.

5. KESIMPULAN DAN CADANGAN

Dari pemerhatian hasil kajian, terdapat suatu tahap amplitud *thermal signature* minimum untuk misil menjejaki pesawat Banshee dengan baik setelah pelancaran. Kajian juga menunjukkan terdapat gangguan sintilasi yang besar yang boleh mengganggu penjejakan misil. Oleh itu, untuk mendapat keadaan yang boleh memberikan keberkesanan tembakan misil yang tinggi, penembak perlu menunggu pesawat berada pada jarak yang agak hampir atau dalam keadaan cuaca yang lebih cerah supaya *thermal signature* pesawat mencukupi untuk penjejakan.

Di samping itu, *hot nose* pada Banshee perlulah mempunyai permukaan yang berwana gelap dan tidak berkilat supaya ia dapat memancarkan *thermal signature* dengan lebih baik yang dapat memberikan suhu sebenar. Seterusnya, *hot nose* hendaklah bersesuaian dengan *thermal signature* pesawat pejuang yang

sebenar seperti MIG. Walaupun suhu *hot nose* yang tinggi akan memberikan *thermal signature* yang jelas semasa latihan, tetapi ia tidak menggambarkan keupayaan misil yang sebenar. Adakah misil tersebut boleh menjejaki pesawat sebenar dari arah hadapan? Seterusnya, adakah penjejakan misil berkupayaan mengena sasaran dari arah sisi atau dari arah belakang? Oleh itu, kajian yang berterusan diperlukan untuk menentukan keberkesanan tembakan misil MANPADS di persekitaran Malaysia.

PENGHARGAAN

Penulis amat berterima kasih kepada Pn. Jamilah bt Jaafar dan Pn. Hafizah bt. Yusof kerana membantu dalam menjalankan kajian medan dan memberi cadangan penambahbaikan kertas teknikal ini. Penulis juga berterima kasih kepada En. Kamsani b. Kamal dan tim BTP, Batu Arang kerana membenarkan tim kajian menyertai pengujian medan.

RUJUKAN

Akram, S. H. A. (1991). *Infrared Science and Technology for Military Applications.* Pakistan: Institute of Optronics.

Kopp, C. (2005). *Heat-Seeking Missile Guidance.* Dari laman web: http:www.ausairpower.net/TE-IR-Guidance.html (Tarikh akses terakhir : 23 September 2008).

Pierre Brémond. *Cedip IR System - Cameras and systems for Infrared signature Titanium, Orion ALTAIR & SATIR.* Persembahan pada 21 Julai 2008 di BTIE, STRIDE.

Siouris, G.M. (2004). *Missile Guidance and control System.* Springer, New York.

Wikipedia (2008). *Man-portable air-defense systems.* Dari laman web: http://en.wikipedia.org/wiki/ Man-portable air-defense systems (Tarikh akses terakhir : 8 Ogos 2008).

CATCH OF THE NET

Future Combat Systems (FCS) is one of the most visual physical embodiments of modern military transformation. FCS is composed of equipment including manned and unmanned vehicles, and ground sensors tied together with a network that also includes soldiers as part of the system. The FCS will be a multi-functional, multi-mission re-configurable system of systems aimed at maximizing joint inter-operability, strategic transportability and commonality of mission roles including direct and indirect fire, air defense, reconnaissance, troop transport, counter mobility, and Command & Control operations. The goal of this effort is to develop a network centric advanced force structure, quantify its benefits, and identify materiel solutions and technologies within the context of the force. The following are relatively interesting and useful websites on FCS technologies and issues:

1) **Future Combat Systems (FCS)**
   http://www.globalsecurity.org/military/systems/ground/fcs.htm

   Provides an excellent overview on FCS and its various components.

2) **US Army: Future Combat Systems**
   https://www.fcs.army.mil

   The US Army's FCS program website.

3) **The Army's Future Combat System (FCS): Background and Issues for Congress**
   http://www.fas.org/sgp/crs/weapons/RL32888.pdf

   A report submitted to the US Congress in May 2008 regarding the progress of development of the US Army's FCS program.

4) **Future Combat Systems: Dispelling Widespread Myths of the US Army's Primary Modernization Program**
   http://www.heritage.org/press/commentary/021208e.cfm

5) **Future Combat Systems: A Congressional Guide to Army Modernization**
   http://www.heritage.org/Research/NationalSecurity/bg2091.cfm#_ftn1

   News commentaries on the challenges, importance and advantages of FCS.

6) **Boeing: Future Combat Systems**
   http://www.boeing.com/defense-space/ic/fcs/bia/index.html

7) **Science Applications International Corporation (SAIC): Future Combat Systems**
   http://www.saic.com/natsec/fcs/

   Updates from the US Army's FCS program's two lead systems integrators (LSI).

8) **Defense Tech FCS Watch**
   http://www.defensetech.org/archives/cat_fcs_watch.html

9) **Defence Update: Future Combat Systems**
   http://www.defense-update.com/topics/topics-fcs.htm

10) **Future Combat**
    http://www.washingtonpost.com/wp-srv/technology/interactives/futurecombat/index.html

    Websites that provide updates on the latest FCS technologies and issues.